A STUDY OF THE EFFECT OF LENGTH TO DIAMETER RATIO ON THE RESULTS OF PRESSUREMETER TESTS

By

Mitsuhiro Yao

A THESIS

SUBMITTED FOR THE

DEGREE OF MASTER OF SCIENCE

AT THE UNIVERSITY OF OXFORD

Wolfson College

Hilary Term, 1996

Abstract

A STUDY OF THE EFFECT OF LENGTH TO DIAMETER RATIO ON THE RESULTS OF PRESSUREMETER TESTS

A thesis submitted for the degree of Master of Science

M. Yao

Wolfson College, Oxford

Hilary Term, 1996

The pressuremeter is one of the most commonly used devices in *in-situ* testing, because the interpretation method is relatively easy on the assumption that the pressuremeter is infinitely long. However, the effects of length-to-diameter ratio on the test results have been questioned recently, and so this thesis explores the effects of length-to-diameter ratio on the results of pressuremeter tests in soils.

First, the finite element method is used to analyse numerically the effects of length-to-diameter ratio on self-boring pressuremeter test results, both in sand and in clay since it is impossible to solve the cavity expansion problem theoretically on the assumption that the length of the pressuremeter is finite. In the analysis of clay, the effects of length-to-diameter ratio on the shear modulus and the shear strength are emphasized. In the analysis of sand, the effects of the length-to-diameter ratio on the friction angle are emphasized.

The finite element method is also used to analyse the effects of length-to-diameter ratio on full-displacement pressuremeter tests in clay. The effects of length-to-diameter ratio on the rigidity index, shear strength, shear modulus and initial horizontal stress are emphasized.

Finally, several calibration tests are performed to investigate the effects of length-to-diameter ratio on the limit pressure of a full-displacement pressuremeter in sand. Three values of length-to-diameter ratio (5,10 or 20) are used to investigate the effects.

Acknowledgements

I would like to express my indebtedness to several people who have been of continual assistance to me throughout my stay here in Oxford. My thanks to Professor Guy T. Houlsby who supervised my work and who was always available for consultation. I greatly admire his enthusiasm, dedication, strict attitude and work in the field of soil mechanics. The technical support given to me by Mr Bob Earl in the Soil Mechanics Laboratory was invaluable.

I also wish to express my gratitude to the following members of the laboratory for their useful comments and suggestions during the course of my work: Dr. Harvey Burd and Dr. Brendan Ruck. Many thanks to Miss Nicola Andrews for her secretarial services.

I would also like to thank to my former tutors of Tokyo University for giving me an opportunity to study here in Oxford: Honorary Professor Kenji Ishihara, Professor Ikuo Towhata and Dr. Mitsutoshi Yoshimine.

My thanks also go to my friends and seniors, Mr. Mitsutoshi Setoh, and Mr. Tetsuo Kobayashi, for their continual encouragement during my work here.

May I express my deepest gratitude to my dear parents for their unfailing support and inspiration which they have given to me over the past years. Many thanks also to my brother, my friends and seniors in my college, for their kind encouragement.

Finally, I would like to express my appreciation to my dearest girl-friend, Miss Yoshiko Katsuya in Kyoto University, for inspiring me many times and being a constant source of love and encouragement.

Nomenclature

A, B, B_l	Constants of integration
D	Pressuremter diameter
E	Young's modulus
f	Matsuoka yield function
g	Matsuoka plastic potential function
G	Shear modulus
G^*	Shear modulus of correction layer
G_{cm}	Corrected measured shear modulus
G_{in}	Input shear modulus
G_m	Measured shear modulus
G_m^∞	Measured shear modulus for an infinitely long pressuremeter
H	Height of mesh
I_r	Rigidity index
I_{rin}	Input rigidity index
I_{rcm}	Corrected measured rigidity index
I_{rm}	Measured rigidity index
I_{rm}^∞	Measured rigidity index for an infinitely long pressuremeter
I_s	Stiffness index
I_1	$\sigma_1 + \sigma_2 + \sigma_3$
I_1^*	$\sigma_1^* + \sigma_2^* + \sigma_3^*$
I_2	$\sigma_1\sigma_2 + \sigma_2\sigma_3 + \sigma_3\sigma_1$
I_2^*	$\sigma_1^*\sigma_2^* + \sigma_2^*\sigma_3^* + \sigma_3^*\sigma_1^*$
I_3	$\sigma_1\sigma_2\sigma_3$
I_3^*	$\sigma_1^*\sigma_2^*\sigma_3^*$

k	Parameter in Matsuoka model
k	Factor
K	$\frac{1+\sin\phi_{cv}}{1-\sin\phi_{cv}}$
K_1, K_2, c_l	Constants for hyperbolic function
L	Pressuremeter length
M	$\frac{2(1+\nu)}{1-\nu^2}$
n	Ratio of the outer to inner radii of the correcting layer
n	$\frac{1-\sin\phi}{1+\sin\phi}$
N	$\frac{1+\sin\phi}{1-\sin\phi}$
P	Pressure of cavity expansion
P_l	Limit pressure
r	Radial co-ordinate
$r_{b0}, r_b, r_{bl}, r_c, r_{bc}$	Radii (see Figure 2 to 7)
r_{cp}	cavity pressure ratio
R	Radius of mesh
R	Pressuremter radius
R_i, R_h, R_y, R_l, R_c	Pressuremeter radii (see Figure 2 to 7)
R	Pressuremeter radius
R_d	Relative density
R_{da}	Nominal relative density
R_0	Initial radius of pressuremeter
s	Slope of a line found in Hughes *et al.*'s simplified analysis
s_{cm}	Corrected measured slope
s_{ex}	Yu's exact solution based slope
s_m	Measured slope
s_m^∞	Measured slope for an infinitely long pressuremeter
s_{ta}	Hughes *et al.*'s simplified solution based slope
s_u	Undrained shear strength
s_{ucm}	Corrected measured shear strength
s_{uin}	Input shear strength
s_{um}	Measured shear strength
s_{um}^∞	Measured shear strength for an infinity long pressuremeter

u	Radiual displacement
u_0	*In-situ* pore pressure
v	Volumetric strain
V	Volume of pressuremeter
$\frac{\delta V_c}{V_c}$	Volumetric strain derived from the central hoop strain
$\frac{\delta V_v}{V_v}$	Volumetric strain derived from volumetric hoop strain
Y	$\frac{2c\cos\phi}{1-\sin\phi}$
α	$\frac{1+\sin\phi}{1-\sin\phi}$
γ	shear strain
γ_l	$\frac{\alpha(\beta+1)}{(\alpha-1)\beta}$
δ	$\frac{Y+(\alpha-1)\sigma_{h0}}{2(1+\alpha)G}$
ϵ	Strain
ϵ_c	Central hoop strain
ϵ_i	Principal strain
ϵ_l	Strain when limit pressure is reached
ϵ_{max}	Maximum strain
$\epsilon_r, \epsilon_\theta$	Strains
ϵ_v	Volumetric hoop strain
ζ	$\tan^2\varphi_{tc}$
ζ^*	$\tan^2\varphi_{tc}$
η	$\exp\{\frac{[(\beta+1)(1-2\nu)Y+(\alpha-1)\sigma_{h0}](1+\nu)}{2(1+\nu)(\alpha-1)\beta}\}$
λ	Lame modulus
λ	undetermined multiplier
ν	Poisson's ratio
ν^*	Poisson's ratio of added mesh
ξ	$\frac{2(1-\nu^2)\delta}{(1+\nu)(\alpha-1)\beta}[\alpha\beta+1-\frac{\nu(\alpha+\beta)}{1-\nu}]$
σ_h	Horizontal Stress
σ'_h	Effective horizontal stress
σ_r, σ_θ	Stresses
σ_{h0}	*In-situ* horizontal stress
σ_{h0}	Initial horizontal stress
σ_{h0c}	Corrected initial horizontal stress

σ_{h0cm}	Corrected measured initial horizontal stress
σ_{h0in}	Input initial horizontal stress
σ_{h0m}	Measured initial horizontal stress
σ_{h0m}^{∞}	Measured initial horizontal stress for an infinitely long pressuremeter
σ_i	Principal stress
σ_{ij}^{*}	$\sigma_{ij} + k\delta_{ij}$
σ_{R_y}	Radial stress at the elastic-plastic boundary
ϕ	Friction angle
ϕ_{cm}	Corrected measured friction angle
ϕ_{cr}	Critical friction angle
ϕ_{ex}	Yu's exact solution based friction angle
ϕ_m	Measured friction angle
ϕ_m^{∞}	Measured friction angle for an infinitely long pressuremeter
ϕ_{ps}	Friction angle for plane strain
ϕ_{psin}	Input friction angle for plane strain
ϕ_{ta}	Hughes et al.s simplified solution based friction angle
ϕ_{tc}	Friction angle for triaxial compression
ϕ_{tcin}	Input friction angle for triaxial compression
ψ	Dilation angle
p	Pressure of the cavity
p_l	Limit pressure
p_{lcm}	Corrected measured limit pressure
p_{lin}	Limit pressure calculated from input values
p_{lm}	Measured limit pressure
p_{lm}^{∞}	Measured limit pressure for an infinitely long pressuremeter
ψ_{ps}	Dilation angle for plane strain
ψ_{psin}	Input dilation angle for plane strain
ψ_{tc}	Triaxial dilation angle
ψ_{tcin}	Input dilation angle for triaxial compression
$p^{10\%}$	Pressure at 10% strain

Contents

Abstract ii

Acknowledgements iii

Nomenclature iv

1 Introduction **1-1**

1.1 Introduction 1-1

1.2 Review 1-3

1.2.1 Introduction 1-3

1.3 Cavity expansion theory 1-6

1.3.1 Elastic stage 1-8

1.3.2 Plastic stage 1-9

1.4 Objectives of the study 1-19

2 Study of self-boring pressuremeter **2-1**

2.1 Analysis in clay 2-2

2.1.1 Introduction 2-2

2.1.2 Procedure of interpretation 2-3

2.1.3 Numerical results 2-8

2.2 Analysis in sand 2-33

2.2.1 Introduction 2-33

2.2.2 Procedure of interpretation 2-36

2.2.3 Numerical results 2-38

2.3 Recommended interpretation procedure 2-62

2.3.1 Self-boring pressuremeter tests in clay 2-62
2.3.2 Self-boring pressuremeter in sand 2-63
2.4 Final remark 2-65

3 Study of the full-displacement pressuremeter 3-1
3.1 Introduction 3-1
3.2 Procedure of Interpretation 3-3
3.3 Numerical results 3-5
3.4 Effects of length-to-diameter ratio 3-13
3.4.1 Rigidity index 3-13
3.4.2 Shear strength 3-13
3.4.3 Shear modulus 3-15
3.4.4 Initial horizontal stress 3-16
3.4.5 Limit pressure 3-16
3.5 Effects of rigidity index 3-16
3.5.1 Rigidity index 3-16
3.5.2 Shear strength 3-18
3.5.3 Shear modulus 3-19
3.5.4 Initial horizontal stress 3-19
3.5.5 Limit pressure 3-21
3.6 Application 3-22
3.7 Final remark 3-28

4 Experimental apparatus and sample preparation 4-1
4.1 Introduction 4-1
4.2 Experimental apparatus 4-2
4.2.1 The cone-pressuremeter 4-2
4.2.2 The Oxford sand calibration chamber 4-3
4.2.3 The driving rig 4-3
4.2.4 The hopper and sieve 4-6
4.3 The pressurization system for the pressure-meter 4-10
4.4 Procedure of the test 4-10
4.5 Data acquisition and calibration 4-13

5 Experimental results **5-1**

5.1 Introduction 5-1

5.2 Calibration results 5-1

5.3 Interpretation method 5-2

5.3.1 Data reduction and correction 5-2

5.4 Experimental results 5-3

5.5 Final remark 5-9

6 Conclusion **6-1**

6.1 Introduction 6-1

6.2 Self-boring pressuremeter 6-1

6.3 Full-displacement pressuremeter 6-2

6.4 Experimental Work 6-3

6.5 Recommendations for future work 6-3

References **Ref-1**

List of Tables

1 Mesh size 2-4

2 Results of measured values from finite element analysis of self-boring pressuremter with the small mesh (see text for definitions of variables) 2-20

3 Results of measured values from finite element analysis of self-boring pressuremter with the medium mesh (see text for definitions of variables) 2-21

4 Results of measured values from finite element analysis of self-boring pressuremter with the large mesh (see text for definitions of variables) 2-22

5 Results of corrected measured values divided by input values from finite element analysis of self-boring pressuremeter with the small mesh (see text for definitions of variables) 2-23

6 Results of corrected measured values divided by input values from finite element analysis of self-boring pressuremeter with the medium mesh (see text for definitions of variables) 2-24

7 Results of corrected measured values divided by input values from finite element analysis of self-boring pressuremeter with the large mesh (see text for definitions of variables) 2-25

8 Input values for analysis of self-boring pressuremeter in sand 2-36

9 Results of measured values of the slope from finite element analysis of self-boring pressuremeter in sand for $\phi_{psin} = 33^{o}$ (see text for definitions of variables) 2-43

10 Results of measured values of the slope from finite element analysis of self-boring pressuremeter in sand for $\phi_{psin} = 38^{o}$ (see text for definitions of variables) 2-44

11 Results of measured values of the slope from finite element analysis of self-boring pressuremeter in sand for $o_{psin} = 43^o$ (see text for definitions of variables) 2-45
12 Results of measured values of the slope from finite element analysis of self-boring pressuremeter in sand for $o_{psin} = 48^o$ (see text for definitions of variables) 2-46
13 A comparison of corrected measured values from finite element analysis of self-boring pressuremeter in sand for $o_{psin} = 33^o$ (see text for definitions of variables) 2-47
14 A comparison of corrected measured values from finite element analysis of self-boring pressuremeter in sand for $o_{psin} = 38^o$ (see text for definitions of variables) 2-48
15 A comparison of corrected measured values from finite element analysis of self-boring pressuremeter in sand for $o_{psin} = 43^o$ (see text for definitions of variables) 2-49
16 A comparison of corrected measured values from finite element analysis of self-boring pressuremeter in sand for $o_{psin} = 48^o$ (see text for definitions of variables) 2-50
17 Results of measured values from finite element analysis of full displacement pressuremter 3-11
18 A comparison between corrected measured and input values from finite element analysis of full displacement pressuremter 3-12
19 Test results at Madingley by Powell and Shields 3-23
20 Test results at Madingley by Houlsby and Withers 3-23
21 Test results at Bothkennar by Powell and Shields 3-24
22 Corrected values of test results at Madingley 3-25
23 Corrected values of test results at Bothkennar 3-26
24 Results of calibration 4-14
25 Results of the experimental work 5-1
26 Results of the experimental work by Schnaid(1990) 5-7

List of Figures

1 The segment of the soil in cylindrical polar co-ordinates 1-6
2 A ground condition before pressuremeter installation 1-10
3 A ground condition just after pressuremeter installation 1-10
4 A ground condition when the cavity pressure has reached initial horizontal stress 1-10
5 A ground condition in the plastic stage 1-12
6 A ground condition when the cavity pressure has reached the limit pressure 1-13
7 A ground condition in the contraction (reverse-plastic) stage 1-13
8 Structure of the finite element mesh 2-4
9 Small finite element mesh 2-4
10 Medium finite element mesh 2-5
11 Large finite element mesh 2-5
12 Procedure of pressuremeter interpretation 2-7
13 A comparison between theoretical and numerical self-boring pressuremeter curves ($I_r = 100$) 2-8
14 A comparison between measured values of shear modulus ($I_r = 500, D/L = \infty$) 2-9
15 A comparison between measured values of shear strength ($I_r = 500, D/L = \infty$) 2-9
16 A comparison between corrected measured values of shear modulus 2-10
17 A comparison between corrected measured values of shear strength 2-10
18 Plastic area for $I_r = 50, L/D = 4$.(dark shaded area is the plastically deforming zone) 2-13

19 Plastic area for $I_r = 500, L/D = 4$.(dark shaded area is the plastically deforming zone) 2-14
20 Plastic area for $I_r = 500, L/D = 10$.(dark shaded area is the plastically deforming zone) 2-15
21 Distribution of σ_r for $I_r = 500, L/D = 4$, (contours at intervals of s_u)2-16
22 Distribution of σ_r, $I_r = 500, L/D = \infty$, (contours at intervals of $0.5s_u$) 2-17
23 Distribution of τ for $I_r = 500, L/D = 4$, (contours at intervals of $0.125s_u$) 2-18
24 Distribution of $\tau_{r\theta}$ showing small numerical scatter only for $I_r = 500, L/D = \infty$, (contours at intervals of $0.0004s_u$) 2-19
25 The effects of the length-to-diameter ratio on shear modulus 2-26
26 The effects of the rigidity index on shear modulus 2-27
27 The effects of length to diameter ratio on shear modulus 2-30
28 Effects of rigidity index on shear modulus 2-31
29 The relationship between ϕ_{ps} and ϕ_{tc} 2-36
30 Procedure of interpretation for self-boring pressuremeter in sand . . 2-39
31 A comparison between theoretical and numerical pressuremeter curves ($I_s = 100$) 2-40
32 Distribution of σ_r for $\phi_{psin} = 33^o, I_s = 500, L/D = 10$, (contours at intervals of $0.8\sigma_{h0}$) 2-41
33 Distribution of $\tau_{r\theta}$ for $\phi_{psin} = 33^o, I_s = 500, L/D = 10$, (contours at intervals of $0.2\sigma_{h0}$) 2-42
34 A comparison between s_{ta} and s_{ex} 2-52
35 A comparison between ϕ_{ta} and ϕ_{ex} 2-52
36 A comparison between s_m and s_{ex} using central hoop strain 2-53
37 A comparison between ϕ_m and ϕ_{ex} using central hoop strain 2-54
38 A comparison between s_{cm} and s_{ex} using volumetric hoop strain . . 2-55
39 A comparison between ϕ_{cm} and ϕ_{ex} using volumetric hoop strain . . 2-56
40 A comparison between s_{cm} and s_{ex} using central strain ($L/D = 5, 6, 8, 10$) 2-58

41 A comparison between s_{cm} and s_{ex} using central strain (L/D = 12, 16, 20) 2-59
42 A comparison between o_{cm} and o_{ex} using central strain (L/D = 5, 6, 8, 10) 2-60
43 A comparison between o_{cm} and o_{ex} using central strain (L/D = 12, 16, 20) 2-61
44 The combined effects on slope due to finite length and elastic deformation(centre) 2-65
45 The combined effects on friction angle due to finite length and elastic deformation(centre) 2-66
46 Mesh used in the full-displacement pressuremeter analysis 3-2
47 Houlsby and Withers(1988) analysis 3-3
48 Procedure of interpretation 3-6
49 Distribution of σ_r for $I_r = 200$, $L/D = 6$, (contours at intervals of s_u) 3-8
50 Distribution of $\tau_{r\theta}$ for $I_r = 200$, $L/D = 6$, (contours at intervals of $0.2s_u$) 3-9
51 Plastic area for $I_r = 200$, $L/D = 6$, (dark shaded area is the plastically deforming zone) 3-10
52 Typical pressuremeter curves from finite element analysis of full-displacement pressuremeter ($I_r = 200$) 3-11
53 The effects of the length-to-diameter ratio on the calculated rigidity index 3-14
54 The effects of the length-to-diameter ratio on the calculated shear strength 3-14
55 The effects of the length-to-diameter ratio on the calculated shear modulus 3-15
56 The effects of the length-to-diameter ratio on the calculated initial horizontal stress 3-17
57 The effects of the length-to-diameter ratio on the calculated limit pressure 3-17
58 The effects of the input rigidity index on the calculated rigidity index3-18
59 The effects of the input rigidity index on the calculated shear strength3-19

60 The effects of the input rigidity index on the calculated shear modulus3-20
61 The effects of the input rigidity index on the calculated initial horizontal stress 3-20
62 The effects of the input rigidity index on the calculated limit pressure3-21
63 A typical pressuremeter curve from a field test b1, see Table 65 . . 3-22
64 Results of the correction of Madingley results (best estimate as made by Powell and Shields) 3-26
65 Results of the correction of Bothkennar results (best estimate as made by Powell and Shields) 3-27
66 The mechanism for the pressuremeter pressurization 4-1
67 The Oxford calibration chamber 4-5
68 The mechanism of the driving rig 4-7
69 The hopper 4-8
70 The sieve 4-9
71 The mechanism for the pressuremeter pressurization 4-11
72 Calibration result of displacement transducer 4-14
73 Calibration result of pressuremeter transducer 4-15
74 Three-parameter hyperbola 5-2
75 A typical result of membrane calibration 5-3
76 Experimental results for $K_0 = 0.5$ 5-5
77 Experimental results for $K_0 = 1.0$ 5-5
78 Experimental results for $K_0 = 2.0$ 5-6
79 Density effects on the limit pressure 5-8
80 Density effects on the limit pressure(10%) 5-8
81 Length-to-diameter effects on the limit pressure 5-9
82 Length-to-diameter effects on the limit pressure(10%) 5-10
83 Length-to-diameter effects on the limit pressure 5-10
84 Length-to-diameter effects on the limit pressure(10%) 5-11

Chapter 1

Introduction

1.1 Introduction

The design of any structure or foundation requires a good understanding of the underlying ground condition. There are two basic methods to determine ground conditions. First, there is a laboratory test, in which a small sample is taken from the ground to be investigated. Second, there is the *in-situ* test, where the ground conditions are investigated directly. *In-situ* testing has the distinct advantage of being fast and relatively inexpensive. The pressuremeter (e.g. the self-boring pressuremeter, the cone-pressuremeter), which is a well-known *in-situ* device, is the focus here. The pressuremeter was first introduced by Louis Menard forty years ago in France. Since then it has been used all over the world, partly because the interpretation of the result is relatively easy, working on the assumption that the pressuremeter is infinitely long.

As long as ground disturbance during installation is minimized, the self-boring pressuremeter is a device which can measure the soil strength, stiffness and *in-situ* horizontal stress with tolerable accuracy. However, it is difficult to operate this test because it is slow and requires skilled operators.

The cone-pressuremeter is a relatively new *in-situ* device which was developed to combine the profiling efficiency of the cone penetrometer and the merit of self-boring pressuremeter. The device consists of 60^{o} penetrometer and pressuremeter. This test is relatively fast and easy to do. However, since the installation causes

ground disturbance, the interpretation of the results is more difficult than for the self-boring device.

The pressuremeter tests, as described above, give a lot of *in-situ* information, including the stiffness and strength of the soil, and *in-situ* horizontal stress. The accuracy of these values continues to be discussed. However, the consensus view is introduced below.

In measuring the *in-situ* stiffness of the soil, the value obtained from the unload-reload stage is thought to be more reliable than the initial or tangent value, since the unload-reload value has a good agreement with the laboratory based value (Fahey and Randolph (1984), Mair and Wood (1987)).

As for soil strength, it has been shown by experience that undrained strength values of clay derived from the self-boring pressuremeter are higher than the expected values obtained from laboratory tests. One of the possible reasons for this is that the laboratory based value is too low due to disturbance during sampling. Other possible reasons are finite length of the probe (Borsetto *et al.* (1983), Yeung and Carter (1986), Houlsby and Carter (1993), Shuttle and Jefferies (1995)) and the method of data reduction applied (Wroth (1984)). It is also difficult to understand the strength of the sand using the pressuremeter, although a friction angle can be obtained from the pressuremeter test using Hughes *et al.*'s (1977) method. The friction angle obtained from this approach is found to be larger than the value obtained from empirical approach using the cone penetrometer. The possible reasons for this are finite length of the probe (Schnaid, 1990) and the simplicity of Hughes *et al.* 's method (Yu, 1990).

Finally, determination of the *in-situ* horizontal stress in the ground is one of the most difficult tasks because of the disturbance caused by pressuremeter installation. Measuring the horizontal stress in the ground by means of the self-boring pressuremeter has been more successful in clay than in other soils. The lift-off pressure which is found at the beginning of the test is often used. Jamiolkowski *et al.* (1985) has highlighted the many difficulties involved in measuring the initial horizontal stress in sands. Recently, the method of understanding soil properties of clay using cone-pressuremeter is devel

1.2 Review

1.2.1 Introduction

In this section, I would like to focus on some existing studies of the effect of length to diameter ratio. Some attempts have so far been made to analyse the effect of length to diameter ratio on the results of the pressuremeter tests. These works can be divided into three categories:

- Theoretical work
- Numerical analysis by the Finite Element Method (F.E.M)
- Experimental work

Each of the categories is reviewed below.

In this thesis, the effects of length to diameter ratio are discussed sometimes in terms of the factor L/D. On other occasions, it is more convenient to use the inverse of this factor, i.e. D/L, which has the advantage that it becomes zero for an infinitely long pressuremeter.

Review of theoretical work

There are many theoretical analyses of the infinite pressuremeter which shall be considered later. However, only few studies have been made of finite length pressuremeters and all of these have restricted themselves to the elastic stage alone. These studies originated in the paper by Tranter (1946). Tranter found that the displacement at the centre of a finite pressuremeter is less than that of an infinite pressuremeter. The conclusions suggested that the shear modulus measured by a finite length pressuremeter is an overestimate. Moreover, a method for correcting this overestimation was implied in his work. The validity of the plane strain condition has been studied by Livneh *et al.* (1971) using an elastic model. Both of the authors showed that the plane strain approximation can be justified for high values of a length-to-diameter ratio equal to or more than 7.0.

Since the analyses are based highly on the Airy's stress function method, it is not possible to extend this theory to the case of a non-homogeneous or anisotropic

material and the theory is restricted just to the geometry of an infinite cavity, where the ground is infinitely long horizontally and vertically and the pressuremeter is also infinitely long.

Dormieux (1992) investigated the error on the shear modulus due to the assumption of plane strain conditions, by using the method based on the principle of total potential energy and complementary potential energy. This method can be applied to more complex geometry and also to non-homogeneous or anisotropic elastic materials. The analyses have also shown that the overestimation is due to the finite length of the pressuremeter. In this paper, it is found that the overestimation of the shear modulus, calculated under the boundary condition that the surface of the ground is free, rapidly increases when the length-to-diameter ratio is less than 5.

Review of numerical analyses by F.E.M.

The analysis used to investigate the effects of the length-to-diameter ratio using finite element analysis originated in the paper by Borsetto *et al.* (1983).

Borsetto et al. presented some finite element analyses to investigate the effects of the length-to-diameter ratio on the results of the self-boring pressuremeter tests in clay , using an elastic plastic work-hardening model. The pressuremeter was idealized as a cylindrical cavity of finite dimensions. The conclusion was that the soil stiffness is not overestimated as much as the soil strength. The strength of the soil is highly overestimated when the length-to-diameter ratio is less than 10, which agrees with some of the in-situ results. The same effects were found by Baguelin *et al.* (1986), using the Tresca model and the Cam Clay model.

Yeung and Carter (1990) presented a new method to correct the overestimation of the strength of the soil due to the finite length of the pressuremeter and shallow testing depth. The method is based on finite element analysis and the correction is a function of the ratio of the shear modulus to the initial horizontal stress. This new correction gives improved estimates of the undrained shear strength, but the value is higher than other tests (i.e. the vane test). The elastic modulus was found to be determined accurately, not being affected by shallow depth or the length-to-diameter ratio.

Yu (1990) analysed the self-boring pressuremeter in sand and cone-pressuremeter in clay. It was found that the friction angle is overestimated due to the length-to-diameter ratio when the method by Hughes et al. is taken into account. In cone pressuremeter analysis, in clay, it was found that the initial horizontal stress is overestimated if the method by Houlsby and Withers (1988) is applied.

Houlsby and Carter (1993) did finite element analyses for the self-boring pressuremeter in a Tresca material, to investigate the effects of the length-to-diameter ratio and the depth. It was found that the depth effects are remarkably small in comparison with the effects of length-to-diameter ratio, both in soil stiffness and strength, and that the length-to-diameter ratio has more effect on the strength than the stiffness. The shear modulus seems to be measured accurately using the central strain.

Shuttle and Jefferies (1995) commented critically on the paper by Houlsby and Carter (1993). In the paper by Shuttle and Jefferies (1995), it was concluded that the pressure expansion curve for an infinitely long pressuremeter cannot be reproduced by using a correction factor suggested by Houlsby and Carter and that the correction factor should be varied with strain range. However, the criticism was based on a misunderstanding, because the aim of the analysis by Houlsby and Carter was not to reproduce the expansion curve for an infinitely long pressuremeter, and the shear strength was not measured from the limit pressure.

Review of experimental work

Laier *et al.* (1975) carried out calibration chamber tests to investigate the effect of finite pressuremeter length in dry sand. The results suggested that there was no significant effect due to the length-to-diameter ratio, measured when the ratio is over 4.0, which support Tranter's (1946) theoretical prediction. In contrast, it was found that the length-to-diameter ratio had a marked effect on measured limit pressure. However, this effect was found to be independent of sand density and over-consolidation ratio. Limit pressure is overestimated due to the finite length of pressuremeter. The maximum overestimation (60%) was found when the length-to-diameter ratio was about 12.

Schnaid (1990) presented some experimental results using a large chamber with

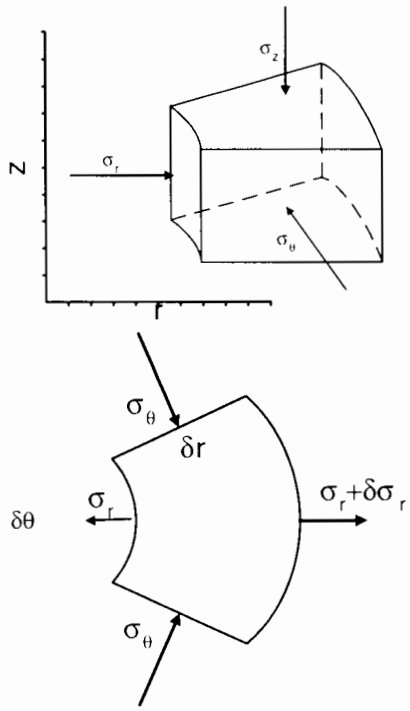


Figure 1: The segment of the soil in cylindrical polar co-ordinates

sand. The limit pressure measured by different lengths of pressuremeter is presented. Limit pressure is found to increase with decreasing length of the pressuremeter .

1.3 Cavity expansion theory

In studying the stress distributions which are related to in-situ testing using pressuremeters, it is recognized that cavity expansion theory is one of the most useful methods for theoretical analysis. The behaviour of the cylindrical cavity is described in terms of cylindrical polar co-ordinates (r, θ, z).

Considering the segment shown in Fig. 1, the force on the inner surface is $-r\sigma_r\delta\theta$ and that on the outer surface is $(r+\delta r)(\sigma_r+\delta\sigma_r)\delta\theta$. There are also forces on both sides of the segment. The resultant force in tangential direction is equal

to zero. Hence, the force in the radial direction on the sides of the element is:

$$-2\sigma_\theta \delta r \sin\frac{\delta\theta}{2}. \tag{1}$$

$\delta\theta$ is sufficiently small that this almost equal to $-\sigma_\theta \delta r \delta\theta$. Considering equilibrium and letting $\delta\theta$ tend to zero, it follows that:

$$\frac{\partial\sigma_r}{\partial r} + \frac{\sigma_r - \sigma_\theta}{r} = 0. \tag{2}$$

or, since σ_r is a function of r only:

$$\frac{d\sigma_r}{dr} + \frac{\sigma_r - \sigma_\theta}{r} = 0 \tag{3}$$

Initially, at time ($t = 0$), the cavity has a radius R_i and an internal pressure σ_{h0}. Later, at a different time (t) the cavity has changed and the radius becomes R. A typical material point of the material has a radial co-ordinate r, which has moved to this position from its original position r_0.

The boundary condition is:

$$\begin{aligned} \sigma_r &= P \quad at \quad r = R \\ \sigma_r &= \sigma_{h0} \quad at \quad r = \infty \end{aligned} \tag{4}$$

The expansion of the cylindrical cavity occurs under conditions of axial symmetry and of plane strain for an infinitely long pressuremeter.

The constitutive equation for the continuum material may be written as a relationship between the rate of change of stress and of strain. The strains are defined as below:

$$\begin{aligned} \dot{\epsilon}_r &= -\frac{\partial\dot{u}}{\partial r} = -\frac{d\dot{u}}{dr} \\ \dot{\epsilon}_\theta &= -\frac{\dot{u}}{r} \\ u &= R - R_i \end{aligned} \tag{5}$$

Even though the displacement may be large, these equations may still be applied since the kinematic constraints do not permit a rotation of principal stress and strain directions.

1.3.1 Elastic stage

The elasticity relations can be expressed as below:

$$E\begin{bmatrix}\delta\epsilon_r\\ \delta\epsilon_\theta\\ \delta\epsilon_z\end{bmatrix}=\begin{bmatrix}1 & -\nu & -\nu\\ -\nu & 1 & -\nu\\ -\nu & -\nu & 1\end{bmatrix}\begin{bmatrix}\delta\sigma_r\\ \delta\sigma_\theta\\ \delta\sigma_z\end{bmatrix} \tag{6}$$

where E and ν are Young's modulus and Poisson's ratio respectively.

Because of elasticity and plane strain, it can be said that

$$\delta\sigma_z=\nu(\delta\sigma_r+\delta\sigma_\theta). \tag{7}$$

where δ means the secant increase.

Substituting the condition of plane strain (equation 7) into the equations of elasticity relations, it is found that:

$$E\begin{bmatrix}\delta\epsilon_r\\ \delta\epsilon_\theta\end{bmatrix}=\begin{bmatrix}1-\nu^2 & -\nu(1+\nu)\\ -\nu(1+\nu) & 1-\nu^2\end{bmatrix}\begin{bmatrix}\delta\sigma_r\\ \delta\sigma_\theta\end{bmatrix} \tag{8}$$

Then, it is obtained from this equation

$$\begin{bmatrix}\delta\sigma_r\\ \delta\sigma_\theta\end{bmatrix}=\frac{E}{(1-2\nu)(1+\nu)}\begin{bmatrix}1-\nu & -\nu\\ -\nu & 1-\nu\end{bmatrix}\begin{bmatrix}\delta\epsilon_r\\ \delta\epsilon_\theta\end{bmatrix}=\begin{bmatrix}\lambda+2G & \lambda\\ \lambda & \lambda+2G\end{bmatrix}\begin{bmatrix}\delta\epsilon_r\\ \delta\epsilon_\theta\end{bmatrix} \tag{9}$$

where G and λ are the shear modulus and Lame modulus respectively as follows:

$$\begin{aligned}G&=\frac{E}{2(1+\nu)}\\ \lambda&=\frac{E\nu}{(1-2\nu)(1+\nu)}=\frac{2G\nu}{(1-2\nu)}\end{aligned} \tag{10}$$

Since

$$\begin{aligned}\sigma_r&=\sigma_{h0}+\delta\sigma_r\\ \sigma_\theta&=\sigma_{h0}+\delta\sigma_\theta,\end{aligned} \tag{11}$$

it follows from the equations 9 that

$$\begin{aligned}\sigma_r&=\sigma_{h0}-(\lambda+2G)\frac{\partial u}{\partial r}-\lambda\frac{u}{r}\\ \sigma_\theta&=\sigma_{h0}-\lambda\frac{\partial u}{\partial r}-(\lambda+2G)\frac{u}{r}\end{aligned} \tag{12}$$

Substituting these equations into the equilibrium equation (3), the elastic displacement satisfies the second-order ordinary differential equation:

$$\frac{d^2u}{dr^2} + \frac{1}{r}\frac{du}{dr} - \frac{u}{r^2} = 0 \tag{13}$$

It is well known that the general solution for this kind of differential equation can be written as following:

$$u = \frac{A}{r} + Br \tag{14}$$

From the fact that $u \to 0 \quad (r \to \infty)$, it is necessary that $B = 0$. And from the boundary condition (4):

$$A = (\frac{P - \sigma_{h0}}{2G}) R_i{}^2 a \tag{15}$$

In this case, the secant increase of σ_r, that of σ_θ, and the displacement u are

$$\begin{aligned} \delta\sigma_r &= (P - \sigma_{h0})(\frac{R_i}{r})^2 \\ \delta\sigma_\theta &= -\delta\sigma_r = -(P - \sigma_{h0})(\frac{R_i}{r})^2 \\ u &= (\frac{P - \sigma_{h0}}{2G})(\frac{R_i{}^2}{r}) \end{aligned} \tag{16}$$

In addition to this,

$$\begin{aligned} \epsilon_r &= (\frac{P - \sigma_{h0}}{2G})(\frac{R_i}{r})^2 \\ \epsilon_\theta &= -\epsilon_r = -(\frac{P - \sigma_{h0}}{2G})(\frac{R_i}{r})^2 \end{aligned} \tag{17}$$

Normally, c is used instead of σ_r as the pressuremeter expansion pressure. Therefore, the stress-strain relationship in this stage is:

$$c = \sigma_{h0} + 2G\epsilon \tag{18}$$

where ϵ is the negative hoop strain at the surface of the pressuremeter.

1.3.2 Plastic stage

The initial stress state in the ground is $\sigma_r = \sigma_\theta = \sigma_{h0}$, because it is assumed in the cavity expansion theory that the pressuremeter is installed deep in sand or clay without any disturbance. As the pressure of the the cavity increases, σ_r increases

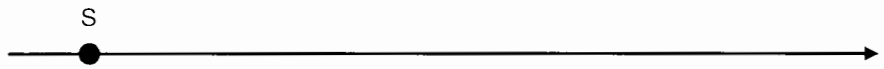


Figure 2: A ground condition before pressuremeter installation

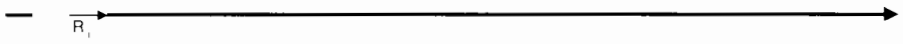


Figure 3: A ground condition just after pressuremeter installation

and σ_θ decreases until they reach the failure condition (plastic stage). The failure condition is different according to whether it is clay or sand. In practice, the Tresca yield condition is applied in the case of clay and the Mohr-Coulomb yield condition is applied in the case of sand.

Clay

Self-boring pressuremeter

The analysis for elastic-perfectly plastic analysis for a self-boring pressuremeter in clay was presented by Gibson and Anderson (1961). The ground conditions before installation are seen in Figure 2, where point S indicates a point on the centre-line of the pressuremeter. Figure 3 shows the ground condition just after installation. R_i is the radius of the pressuremeter. Figure 4 shows the condition when the cavity pressure has reached initial horizontal stress, σ_{h0} and the radius of the pressuremeter is R_h. In these stages, the soil is assumed to be elastic.

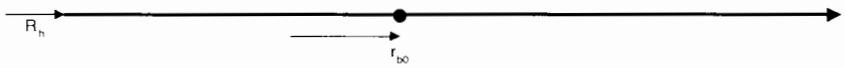


Figure 4: A ground condition when the cavity pressure has reached initial horizontal stress

The yield condition for clay, termed Tresca condition, is expressed when the principal stress components satisfy the inequalities $\sigma_i \leq \sigma_j \leq \sigma_k$:

$$| \sigma_i - \sigma_k | = 2s_u \tag{19}$$

It is assumed that the axial stress σ_z is intermediate between σ_r and σ_θ at yield, which is a reasonable assumption in in-situ tests. So this condition is precisely expressed:

$$\sigma_r - \sigma_\theta = 2s_u \tag{20}$$

Considering the condition 16 and 20, yield will occur when

$$\begin{aligned} \sigma_r &= \sigma_{h0} + s_u \\ \sigma_\theta &= \sigma_{h0} - s_u \end{aligned} \tag{21}$$

The yield condition (20) is applied throughout the plastic zone, equation 13 is written as:

$$\frac{d\sigma_r}{dr} + \frac{2s_u}{r} = 0 \tag{22}$$

which has the solution

$$\sigma_r + 2s_u \ln r = B_l \tag{23}$$

where B_l is a constant of integration.

Figure 5 shows the plastic stage when the radius of the pressuremeter is R_y. Point B shows the elastic-plastic boundary. A plastic region occurs between the radii of R_y and r_b. In Figure 4, r_{b0} indicates the point where point B is at that stage. Plastic deformation is at constant value, which results in the fact that the clay of the plastic region (Figure 5) exists at the stage of the test when the ground pressure is restored.

$$r_{b0}^2 - R_h^2 = r_b^2 - R_y^2 \tag{24}$$

The pressure of point B is $\sigma_{h0} + s_u$, because it just reaches the plastic stage, and equation 23 can be applied both at point S and B with the result that

$$\sigma_{h0} + s_u = P - 2s_u \ln \frac{r_b}{R_y} \tag{25}$$

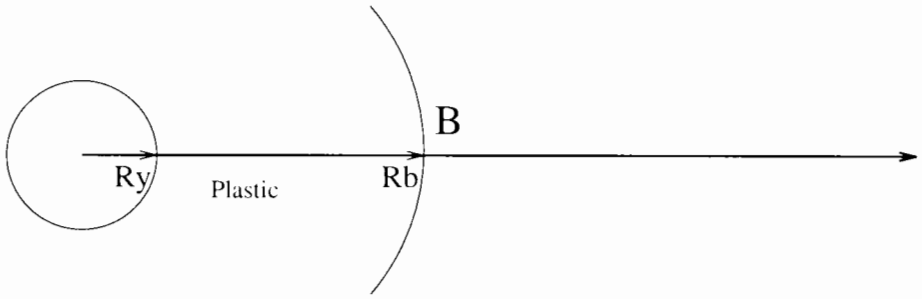


Figure 5: A ground condition in the plastic stage

Then the radius R_h and r_{b0} is expressed as follows:

$$\begin{aligned} R_h &= R_i(1 + \frac{\sigma_{h0}}{2G}) \\ r_{b0} &= r_b(1 - \frac{P - 2s_u \ln \frac{r_b}{R_y} - \sigma_{ho}}{2G}) \end{aligned} \tag{26}$$

Substituting equation 26 into equation 24 and eliminating the term $\frac{r_b}{R_y}$ in equation 25.

$$P = \sigma_{h0} + s_u + s_u \ln[\frac{2G}{s_u}\{1 - (\frac{R_i}{R_y})^2\} - (\frac{R_i}{R_y})^2 \frac{\sigma_{h0}}{s_u}] \tag{27}$$

This can be expressed as

$$P = \sigma_{h0} + s_u + s_u \ln\{I_r \frac{\delta V}{V} - (1 - \frac{\delta V}{V})\frac{\sigma_{h0}}{s_u}\} \tag{28}$$

where $I_r = \frac{G}{s_u}$ is rigidity index and V is volume of pressuremeter. The stiffness of the pressuremeter response diminishes steadily as the elastic-plastic boundary is pushed further out until, eventually, a limiting condition is reached for $\frac{\delta V}{V} = 1$, at which stage all the soil deforms plastically. This limiting pressure v_l is:

$$v_l = \sigma_{h0} + s_u(1 + \ln I_r) \tag{29}$$

so that the response of the pressuremeter in the plastic phase, $\sigma_{h0} + s_u \leq v \leq v_L$, can most conveniently be written as:

$$v = v_l + s_u \ln \frac{\delta V}{V} \tag{30}$$

Then, in theory, if the pressure v is plotted against $\ln \frac{\delta V}{V}$, the plastic phase of the test should lie on a straight line, the gradient of which is the same value as s_u.

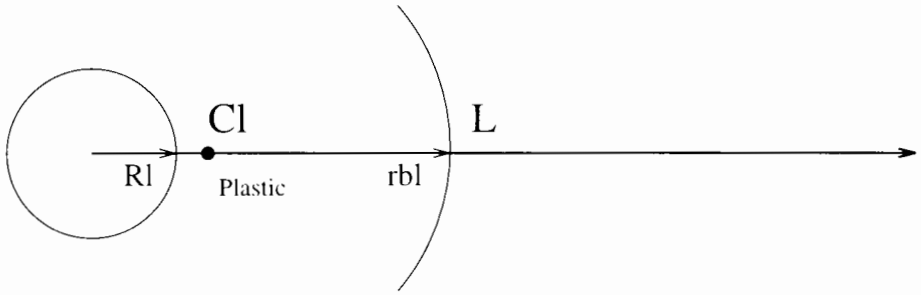


Figure 6: A ground condition when the cavity pressure has reached the limit pressure

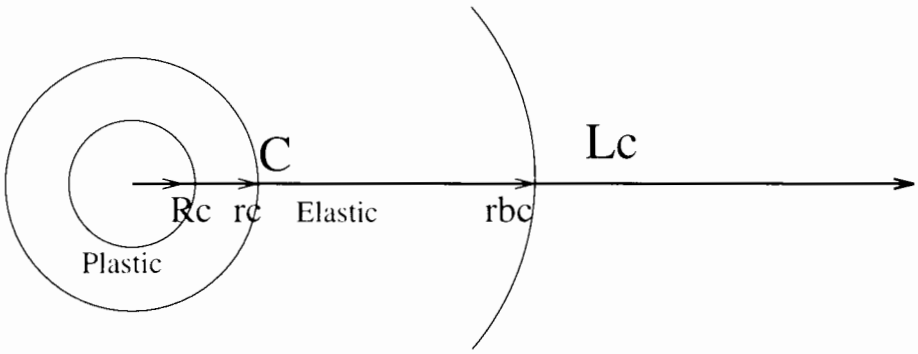


Figure 7: A ground condition in the contraction (reverse-plastic) stage

Cone-pressuremeter

An analysis for full displacement pressuremeter tests in undrained clay soil has been presented by Houlsby and Withers (1988) using a large strain cavity expansion and contraction theory. In the initial plastic phrase, the analysis is similar and the limit pressure obtained is the same as the one in the self-boring pressuremeter. The difference between them is that in cone-pressuremeter analysis there is some disturbance due to installation.

In this particular problem, logarithmic strain is used because large strains are involved with the result that the definition of the strain may have some small effects on the numerical analysis.

To begin with the condition seen in Figure 6, which shows the condition where the limit pressure is reached and point L is at the elastic-plastic boundary. r_{bl} is

the radius of the plastic zone and R_l is the radius of the pressuremeter. At the beginning of the contraction, all the soil behaves elastically, following the equations in the elastic stage. Therefore, the slope of the elastic section of the pressuremeter stress-strain curve is 2G. This elastic stage ends when the condition for reverse plasticity is satisfied:

$$\sigma_r - \sigma_\theta = -2s_u \tag{31}$$

Substituting this reverse plastic condition 31 into the equilibrium equation 3, it follows that

$$\frac{d\sigma_r}{dr} - \frac{2s_u}{r} = 0 \tag{32}$$

which has the solution

$$\sigma_r + 2s_u \ln r = B_u \tag{33}$$

where B_u is a constant of integration.

This condition is firstly satisfied at the surface of the pressuremeter when the pressure is $o_l - 2s_u$. Figure 7 shows the condition when the contraction is performed. Point C is the elastic-plastic boundary (r_c) and the radius of the pressuremeter is R_c. Point L_c is the place where point L in Figure 6 is at this stage and point C_l is the place where point C is in the limit pressure condition. The pressure at point C_l in Figure 6 is obtained as $o_l - 2s_u \ln \frac{r_{cl}}{R_l}$ by using equation 33, so that the pressure at point C in Figure 7 is $o_l - 2s_u \ln \frac{r_{cl}}{R_l} - 2s_u$.

Using equation 33 with the boundary condition,

$$\sigma_r = P \quad at \quad R_c \tag{34}$$

and

$$\sigma_r = o_l - 2s_u - 2s_u \ln \frac{r_{cl}}{R_l} - 2s_u \quad at \quad r_c. \tag{35}$$

$$P = o_l - 2s_u - 2s_u \ln \frac{r_{cl}}{R_l} - 2s_u \ln \frac{r_c}{R_c} \tag{36}$$

is obtained.

The compatibility condition of no volume change requires

$$r_{cl}^2 - R_l^2 = r_c^2 - R_c^2 \tag{37}$$

Focusing on the point C and considering that it behaves elastically until it reaches the reverse plastic condition.

$$\frac{1}{I_r} = \ln \frac{r_{cl}}{r_c} \tag{38}$$

and

$$\epsilon_l - \epsilon_c = \ln \frac{R_l}{R_c} \tag{39}$$

where ϵ_l is a strain in the limit pressure condition and ϵ_c is a strain in the contraction stage.

Substituting equations 38 and 39 gives:

$$\exp(\frac{2}{I_r}) - 1 = (\frac{R_c}{r_c})^2[\exp\{2(\epsilon_l - \epsilon_c)\} - 1] \tag{40}$$

Substituting equations 38 to 40 into equation 36 leads to:

$$P = P_l - 2s_u\{1 + \ln[\sinh(\epsilon_l - \epsilon_c)] - \ln[\sinh(\frac{1}{I_r})]\} \tag{41}$$

Rewriting ϵ_l as ϵ_{max}, because ϵ_l is normally a maximum value of strain, and ϵ_c as a general form, ϵ.

$$v = v_l - 2s_u\{1 + \ln[\sinh(\epsilon_{max} - \epsilon)] - \ln[\sinh(\frac{1}{I_r})]\} \tag{42}$$

When $(\epsilon_l - \epsilon_c)$ is small, in theory, if the pressure v is plotted against $\ln(\epsilon_l - \epsilon_c)$ should give a straight line, the gradient of which is the same value as $2s_u$. In addition, this line passes the point $(0, 2\sigma_{h0} - P_l)$, which can be used to predict the initial horizontal stress.

Sand

In engineering practice, the method developed by Hughes *et al.* (1977) is commonly used to interpret the pressuremeter test in sand, and their method is summarized here. Earlier analyses have been presented by Gibson and Anderson (1961), Ladanyi (1963) and Vesić (1972). The first of these ignores volume changes, the other two incorporate volume changes in different ways. Recently, an exact solution was developed by Yu (1990), and only the method to obtain the pressuremeter expansion curve is introduced here.

Hughes et al.'s method

As the pressure of the cavity increases, σ_r increases and σ_θ decreases until they reach the failure condition, termed the Mohr-Coulomb condition. This is expressed by the yield function when the principal stress components satisfy the inequalities $\sigma_i \leq \sigma_j \leq \sigma_k$:

$$\alpha\sigma_k - \sigma_i = Y \tag{43}$$

where

$$\begin{aligned} \alpha &= \frac{1+\sin\phi}{1-\sin\phi} \\ Y &= \frac{2c\cos\phi}{1-\sin\phi} \end{aligned} \tag{44}$$

and ϕ and c denote the friction angle and the cohesion of soils respectively.

It is assumed that the axial stress σ_z is intermediate between σ_r and σ_θ at yield, which is a reasonable assumption in in-situ tests. So this condition is precisely expressed:

$$\frac{\sigma_r}{\sigma_\theta} = N = \frac{1+\sin\phi}{1-\sin\phi} (0 < N < 1) \tag{45}$$

Therefore, from equation 16 it is found that first yielding occurs at the surface of the pressuremeter when

$$P - u_0 = \sigma_{h0}(1+\sin\phi) \tag{46}$$

where u_0 is the in-situ pore pressure. However, in this thesis, u_0 is always equal to zero, so that u_0 is set to zero from here.

Using the same figure in clay analysis (Figure 5) which shows the plastic condition, in which the radius of the plastic area is r_b and the radius of the pressuremeter is R_y at the moment.

Substituting 45 into 3 and considering the boundary condition

$$\sigma_r = \sigma_{R_y} = \sigma_{h0}(1+\sin\phi) \quad at \quad r = R_y. \tag{47}$$

it follows that:

$$\ln\frac{\sigma_r}{\sigma_{R_y}} = (1-N)\ln\frac{r}{R_y} \tag{48}$$

This equation governs the stress distribution in the plastic area occurring near the pressuremeter.

The mobilized angle of dilation, υ, is defined by

$$\sin\upsilon = -\frac{dv}{d\gamma} \tag{49}$$

where v is the volumetric strain, taken positive for compression, which depends on the difference between υ and ϕ_{cr}, and γ is shear strain. This dependence may be expressed by a stress-dilatancy relationship such as (Rowe,1962):

$$\frac{1+\sin\phi}{1-\sin\phi} = \frac{1+\sin\phi_{cr}}{1-\sin\phi_{cr}}\frac{1+\sin\upsilon}{1-\sin\upsilon} \tag{50}$$

Ignoring elastic strain in the plastic region, it follows from equation 49 that

$$v = -\gamma\sin\upsilon \tag{51}$$

The sand is assumed to be failing when volumetric and shear strains follows the straight line defined by equation 51.

Since there is no rotation of principal strains, v and γ are expressed as:

$$\begin{aligned} v &= \epsilon_r + \epsilon_\theta \\ \gamma &= \epsilon_r - \epsilon_\theta \end{aligned} \tag{52}$$

Therefore, equation 52 can be written as:

$$-\epsilon_r = n\epsilon_\theta \tag{53}$$

where

$$n = \frac{1-\sin\upsilon}{1+\sin\upsilon}(0 < n < 1) \tag{54}$$

Since ϵ_r and ϵ_θ is expressed by u (equations 5), equation 53 leads to the differential equation:

$$\frac{du}{dr} = -n\frac{u}{r} \tag{55}$$

Multiplying r^n, integrating and using the boundary condition $\frac{u}{r} = \epsilon_{R_y} = constant$ at $r = R$, it is found that:

$$\frac{u}{r} = (\frac{R}{r})^{(n+1)}\epsilon_{R_y} \tag{56}$$

Eliminating $\frac{R}{r}$ from equation 48 and 56 and substituting r=R gives

$$\epsilon = \epsilon_{R_y}(\frac{\upsilon}{\sigma_{R_y}})^{\frac{n+1}{1-N}} \tag{57}$$

where ϵ is the strain of the pressuremeter.

Taking logarithms.

$$\ln \epsilon = \frac{n+1}{1-N} \ln \upsilon + constant \tag{58}$$

Therefore, a plot of υ against ϵ on double logarithmic axes should give a straight line with slope s, given by:

$$s = \frac{1-N}{n+1} \tag{59}$$

Using equation 50, equation 59 can be expressed as:

$$\begin{aligned} \sin \phi &= \frac{(K+1)s}{(K-1)s+2} \\ \sin \upsilon &= \frac{2Ks-(K-1)}{K+1} \end{aligned} \tag{60}$$

where

$$K = \frac{1+\sin \phi_{cr}}{1-\sin \phi_{cr}} \tag{61}$$

Then, the angle of friction and the angle of dilation are obtained.

Yu's method

Since it is difficult to summarize the whole theory, only the method to calculate the expansion curve for the cylindrical case is introduced here.

First of all, it is necessary to define the variables written below:

$$\begin{aligned} M &= \frac{2(1+\nu)G}{1-\nu^2} \\ Y &= \frac{2c\cos\phi}{1-\sin\phi} \\ \alpha &= \frac{1+\sin\phi}{1-\sin\phi} \\ \beta &= \frac{1+\sin\upsilon}{1-\sin\upsilon} \\ \gamma &= \frac{\alpha(\beta+1)}{(\alpha-1)\beta} \\ \delta &= \frac{Y+(\alpha-1)\sigma_{h0}}{2(1+\alpha)G} \\ \eta &= \exp\{\frac{[(\beta+1)(1-2\nu)\{Y+(\alpha-1)\sigma_{h0}\}](1+\nu)}{2(1+\nu)(\alpha-1)\beta}\} \\ \xi &= \frac{2(1-\nu^2)\delta}{(1+\nu)(\alpha-1)\beta}[\alpha\beta+1-\frac{\nu(\alpha+\beta)}{1-\nu}] \end{aligned} \tag{62}$$

When $G, \nu, c, \phi, \upsilon, \sigma_{h0}$ are given, all of the variables above stay constant. r_{cp} called cavity pressure ratio is expressed as:

$$r_{cp} = \frac{(1+\alpha)[Y + (\alpha - 1)P]}{2\alpha[Y + (\alpha - 1)\sigma_{h0}]} \tag{63}$$

This parameter can be obtained when the pressure is given.

The ratio of the current radius of the pressuremeter to the initial radius of that is written as:

$$\frac{R}{R_i} = \frac{r_{cp}^{-\gamma}}{(1-\delta)^{(1+\frac{1}{\beta})} - \frac{\gamma}{\eta}\Lambda_1(r_{cp}, \xi)} \tag{64}$$

where

$$\Lambda_1(x, y) = \sum_{i=0}^{\infty} A_n^1 \tag{65}$$

in which

$$A_n^1 = \begin{cases} \frac{y^n}{n!}\ln x & \text{if } n = \gamma \\ \frac{y^n}{n!(n-\gamma)}[x^{(n-\gamma)} - 1] & \text{otherwise} \end{cases} \tag{66}$$

Then, the pressuremeter-expansion curve (ϵ, υ) can be obtained.

1.4 Objectives of the study

As is discussed in the introduction, the effect of the length-to-diameter ratio on the measured value (i.e. stiffness, strength, initial horizontal stress) is large. Therefore, this thesis concentrates on studying the effect of length-to-diameter ratio on in-situ pressuremeter test results. The work falls into two categories.

One of them involves finite element analysis for self-boring pressuremeter in clay and sand and for cone-pressuremeter in clay. The other is experimental work with cone-pressuremeter using sand.

First, in the finite element analysis for self-boring pressuremeter in clay, the analyses following Houlsby and Carter (1993) are expanded to analyse the effects of the length-to-diameter ratio on the stiffness and strength of the soil and the effects of rigidity index. As for self-boring pressuremeter in sand,a correction method is developed and the effects of the length-to-diameter ratio and stiffness index on the friction angle is examined.

Second, in the finite element analysis for the cone-pressuremeter in clay, the interpretation method by Houlsby and Withers (1988) is applied to interpret the tests.

The effects of the length-to-diameter ratio on the initial horizontal stress and the stiffness and strength of the soil are examined. A correction method and interpretation method is developed. The results from the analyses are applied to the pressuremeter in situ test results performed by Powell and Shields (1995).

Finally, in the experimental work, some calibration chamber tests using Leighton Buzzard sand were performed to investigate the effects of the length-to-diameter on the limit pressure.

Chapter 2

Study of self-boring pressuremeter

This chapter investigates the effects of length-to-diameter ratio on the behaviour of a self-boring pressuremeter by using the finite element program developed at Oxford University, known as OXFEM1.45. It is assumed that the self-boring pressuremeter is installed deep into the ground without any disturbance and that the initial soil stress state is unchanged by the installation of the pressuremeter.

The analysis of a finite length self-boring pressuremeter is modelled as a two-dimensional axisymmetric problem, and a large strain elastic perfectly-plastic analysis is used.

As there are several definitions of the word, 'strain', it is necessary to define the definition of the strain strictly. The calculated results depends on the precise definition of the strain, although the differences is small.

In this chapter, 'central hoop strain' (ϵ_c) means:

$$\epsilon_c = \frac{r_c - r_0}{r_0} \tag{67}$$

r_c is the central radius at any stage in the pressuremeter test and r_0 is the initial radius of the pressuremeter.In the analysis, r_0 is set to 1.0.

In order to determine the 'volumetric hoop strain' (ϵ_v), the actual change of volume of the pressuremeter is first calculated. The apparent radius, as determined from this change of volume on the assumption that the pressuremeter deforms as

a right cylinder, is then determined. Defining the radius of this cylinder as r_v, the 'volumetric hoop strain' (ϵ_v) is defined as:

$$\epsilon_v = \frac{r_v - r_0}{r_0} \tag{68}$$

In addition, the 'volumetric strain derived from the central hoop strain' ($\frac{\delta V_c}{V_c}$) means:

$$\frac{\delta V_c}{V_c} = \frac{r_c^2 - r_0^2}{r_c^2} \tag{69}$$

and also the 'averaged volumetric strain derived from volumetric hoop strain' ($\frac{\delta V_v}{V_v}$) is defined as:

$$\frac{\delta V_v}{V_v} = \frac{r_v^2 - r_0^2}{r_v^2} \tag{70}$$

2.1 Analysis in clay

2.1.1 Introduction

As far as the material is concerned, a von Mises material with various shear moduli is used. The shear strength of the soil (s_u) is set to 1.0 in each study, since all stresses can be normalized with respect to s_u. Various rigidity index values ($I_r = G/s_u = 50, 100, 200, 500 or 1000$) are used in these analyses, since the size of the zone around the pressuremeter, where the soil deforms and behaves plastically, depends on the rigidity index. The rigidity index is defined as ratio of the shear modulus to the undrained shear strength (G/s_u). Because exact incompressibility cannot be enforced in a finite element program without introducing numerical problems, the Poisson's ratio for the soil (ν) is set at 0.49 throughout all of the analyses. The size of the loading step in the study is $0.05 s_u$ which is thought to be sufficiently small. In non-linear analysis the choice of step size is important. A compromise is made between large steps which are quick but inaccurate, and small steps which give more accurate solutions but can take an unacceptably long time. The pressure increment of $0.05 s_u$ was found by trial and error. The initial horizontal stress (σ_{h0}) is set to 0.0, since the horizontal stress appears simply as an additive term on all stresses.

In the study, three kinds of meshes are used to check the scale effects of the size of the mesh. The fundamental structures of the three meshes are all the same. The symmetry of the pressuremeter was exploited to reduce the size of the the mesh for the analysis. In order to model a horizontally infinite ground using a mesh of finite dimensions, a correcting layer is added at the outer boundary. In adding this outer mesh, the method which was developed by Burd (1986) is used. Burd showed that it is possible to simulate correctly the material behaviour of the infinite medium by adding the outer mesh. The shear modulus (G^*) and Poisson's ratio (ν^*) of the outer region must satisfy the following equation:

$$\frac{G^*}{G} = \frac{(n^2-1)(1-2\nu^*)}{1+n^2(1-2\nu^*)} \tag{71}$$

where G and ν are shear modulus and Poisson's ratio of the inner layer and n is the ratio of the outer to inner radii of the outer layer. In this study, $n = 2.0$, $\nu^* = 0.0$ and $\frac{G^*}{G} = 0.6$ were adopted. The structure of the mesh, including the boundary conditions and the number of the Gauss points, is shown in Figure 8 and the size of each mesh, which is the only difference between them, is given in Table 1. The meshes are shown in Figure 9, 10 and 11.

Each mesh consists of triangular grid of elements. The triangular grid is enclosed by 6 nodes. The large mesh consists of 588 elements and 1265 nodes in total. The medium mesh consists of 357 elements and 788 nodes. The small mesh consists of 334 elements and 731 nodes.

The body of the pressuremeter above and below the expanding membrane is modelled as rigid. The radius of the pressuremeter ($D/2$) is 1 and the height of the pressuremeter (L) is derived from the length-to-diameter ratio (L/D) in each test. As a result of the symmetry, the height of the pressuremeter seen in the mesh is equal to $L/2$, which is numerically equal to the length-to-diameter ratio (L/D).

In order to model an infinitely long pressuremeter, the pressuremeter is assumed to extend along the whole of the side of the mesh.

2.1.2 Procedure of interpretation

In interpreting the data derived from finite element analyses, the correction method used by Houlsby and Carter (1993) was followed. The details are as follows.

Mesh size	Radius(R)	Height(H)
large mesh	80	80
medium mesh	80	50
small mesh	80	40

Table 1: Mesh size

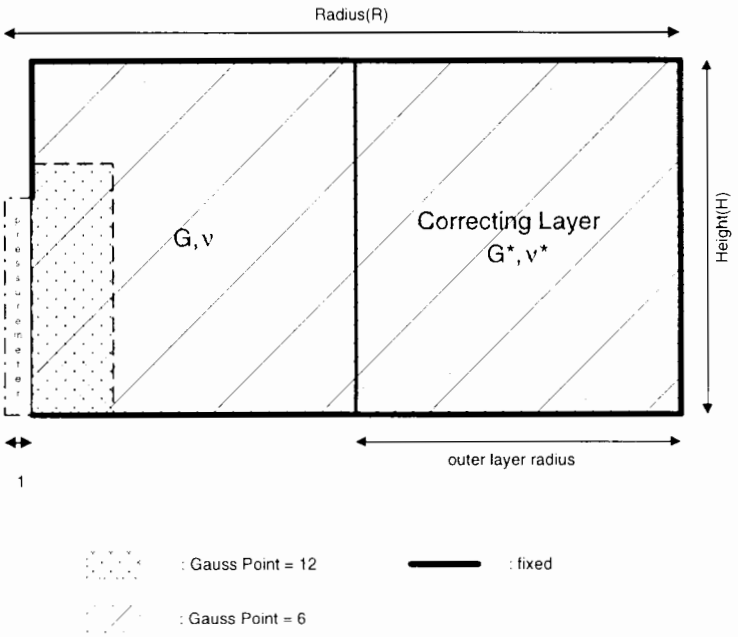


Figure 8: Structure of the finite element mesh

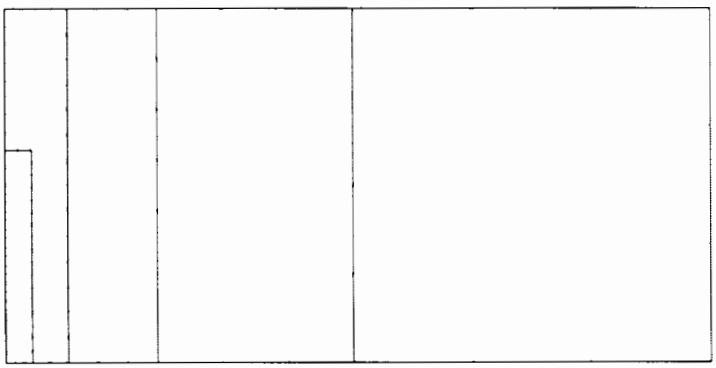


Figure 9: Small finite element mesh

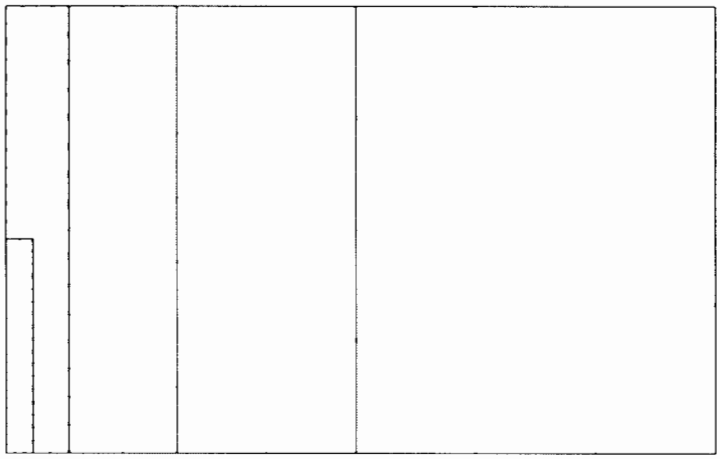


Figure 10: Medium finite element mesh

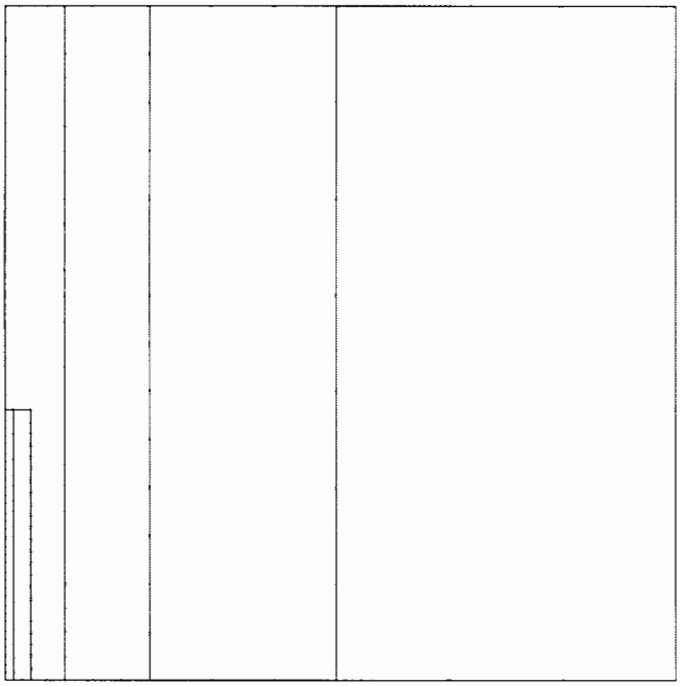


Figure 11: Large finite element mesh

The apparent measured value of shear modulus (G_m) and undrained shear strength (s_{um}) , which are to be compared with the actual input values such as G_{in} and s_{uin}, are derived from the pressuremeter expansion curves. The measured shear modulus is obtained at an early stage of the pressuremeter curve. Measured undrained shear strength was calculated from the following strain range often used in-situ test interpretation. 2% to 5%; 6% to 10% and 6% to 15%. In measuring the shear modulus, ϵ is used. On the other hand, in measuring shear strength, $\frac{\delta V}{V}$ is used and the cavity pressure is plotted against ln $\frac{\delta V}{V}$.

In order to isolate the effects due to the finite length of the pressuremeter from possible numerical errors due to the non-linear solution algorithm, a correction calculation with an infinitely long pressuremeter is carried out with each input shear modulus and undrained shear strength, from these a the measured shear modulus (G_m^∞) and undrained shear strength (s_{um}^∞) with an infinitely long pressuremeter are obtained. These values should be compared very closely with the input values.

Assuming that the numerical errors will be of the same proportion in each analysis with the same input shear modulus and undrained shear strength, the measured shear modulus (G_m) is corrected by being divided by the ratio of the measured shear modulus (G_m^∞) to the input shear modulus (G_{in}). The same correction procedure is used to correct the measured undrained shear strength (s_{um}). Defining these corrected values as G_{cm} and s_{ucm}, the correction procedure is expressed as the following equations:

$$\begin{aligned} G_{cm} &= G_m \frac{G_{in}}{G_m^\infty} \\ s_{ucm} &= s_{um} \frac{s_{in}}{s_{um}^\infty} \end{aligned} \tag{72}$$

The whole interpretation procedure is shown in Figure 12.

In this study, s_u means a triaxial compression undrained shear strength, which corresponds to a plane strain undrained shear strength of $\frac{2}{\sqrt{3}} s_u$. Therefore, all the undrained shear strength values derived from the analysis are multiplied by $\frac{\sqrt{3}}{2}$ and all values given in terms of triaxial compression shear strength.

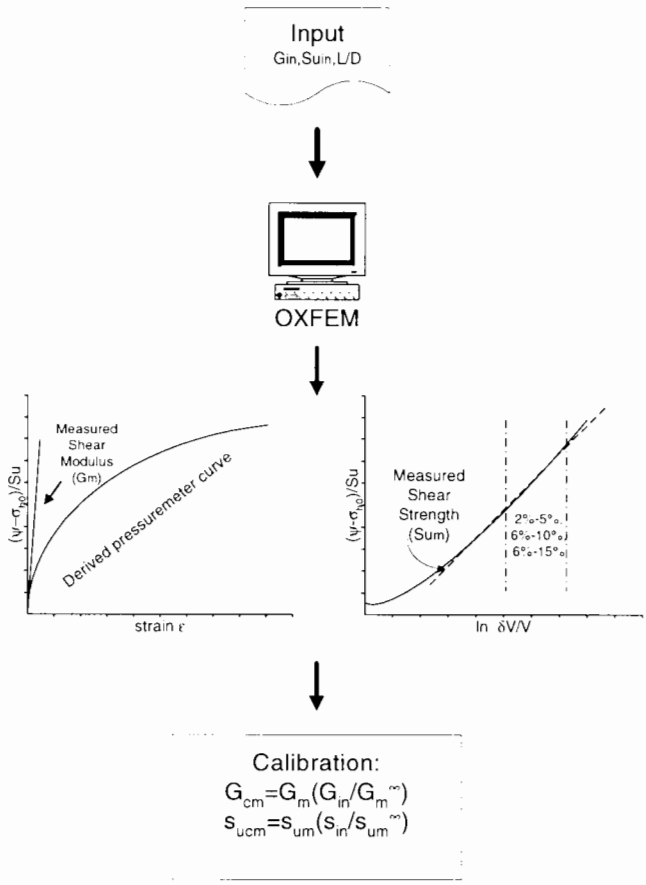


Figure 12: Procedure of pressuremeter interpretation

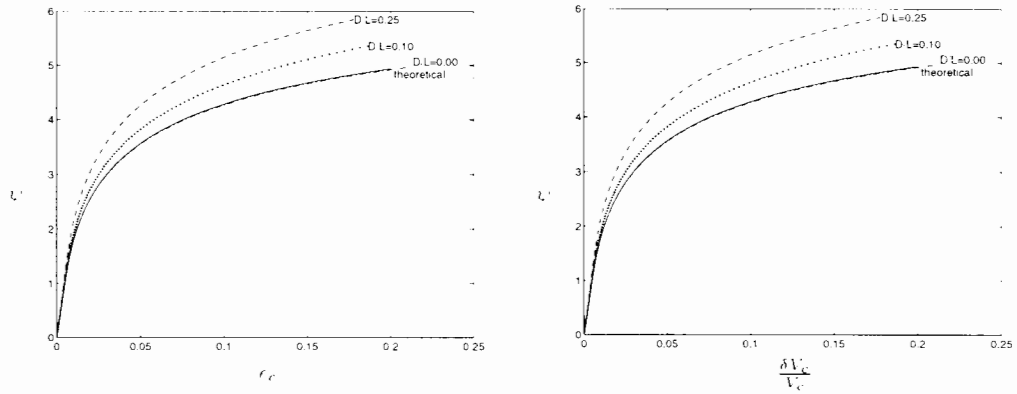


Figure 13: A comparison between theoretical and numerical self-boring pressuremeter curves ($I_r = 100$)

2.1.3 Numerical results

A total of 140 finite element analyses were completed, all possible combinations of 9 values of L/D and 5 values of I_r were analysed using each of the three meshes. One additional L/D ratio was examined with the large mesh only.

The results of all analyses are summarized in Table 2-7. Table 2-4 and Table 5-7 which show measured values and corrected measured values divided by input values respectively.

Figure 13 shows a comparison between theoretical and resulting pressuremeter expansion curves for $I_r = 100$ using the large mesh. A good agreement is found between the theoretical curves and resulting pressuremeter curve for an infinitely long case. Agreement between measured values and input values can also be found in the analysis of infinitely long cases, which indicates that the performance of these numerical analyses are satisfactory. The maximum error found in the measured shear modulus and strength are both less than 1 %.

Comparing the data according to which mesh was used, it is found that all of the results are very similar, although the difference between the results using a small mesh and a large mesh is discernible when the length-to-diameter ratio is small (e.g. $L/D = 4, 5$). This can be seen from Figures 14 and 15, which show the comparison between the input and measured values from the case of $I_r = 500$. Note that although the discussion of figures is in terms of the ratio L/D, the axis

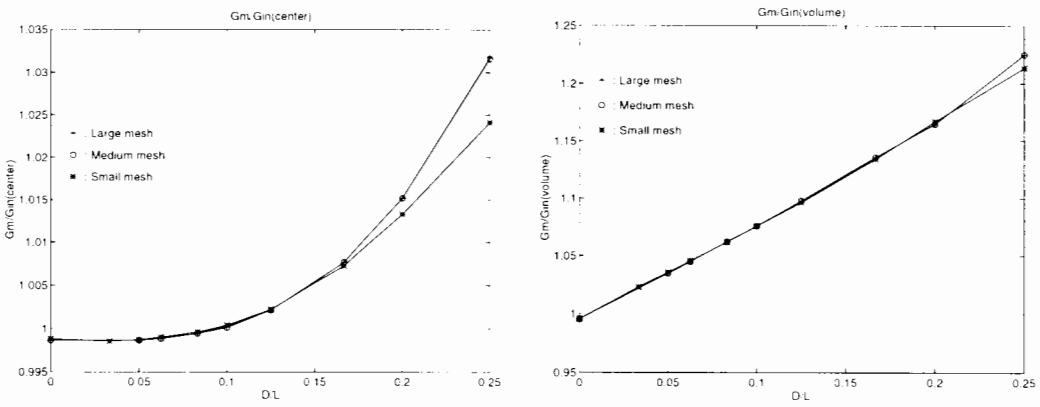


Figure 14: A comparison between measured values of shear modulus ($I_r = 500, D/L = \infty$)

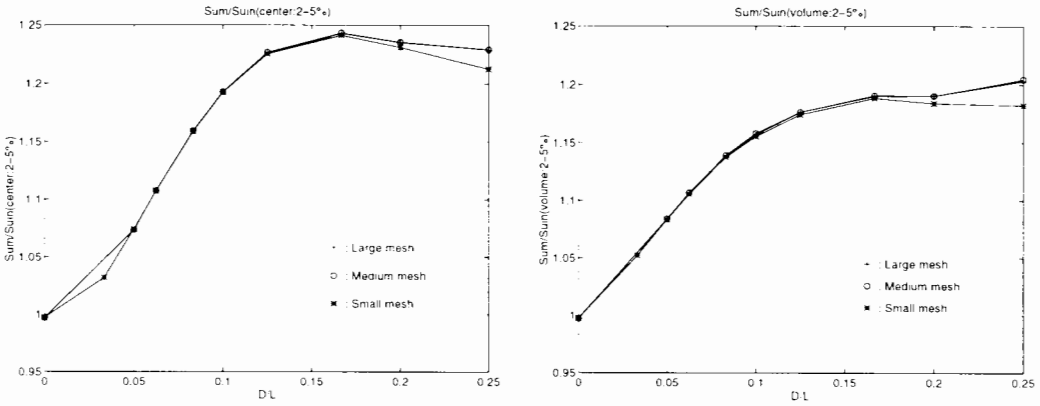


Figure 15: A comparison between measured values of shear strength ($I_r = 500, D/L = \infty$)

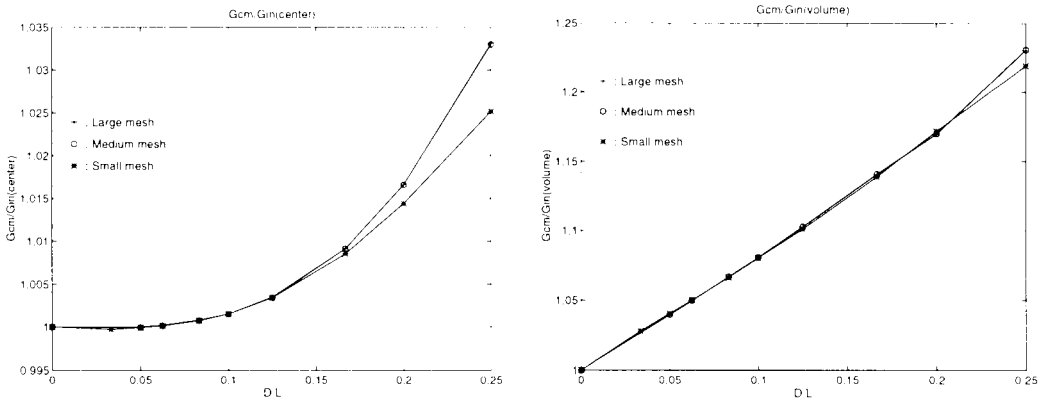


Figure 16: A comparison between corrected measured values of shear modulus

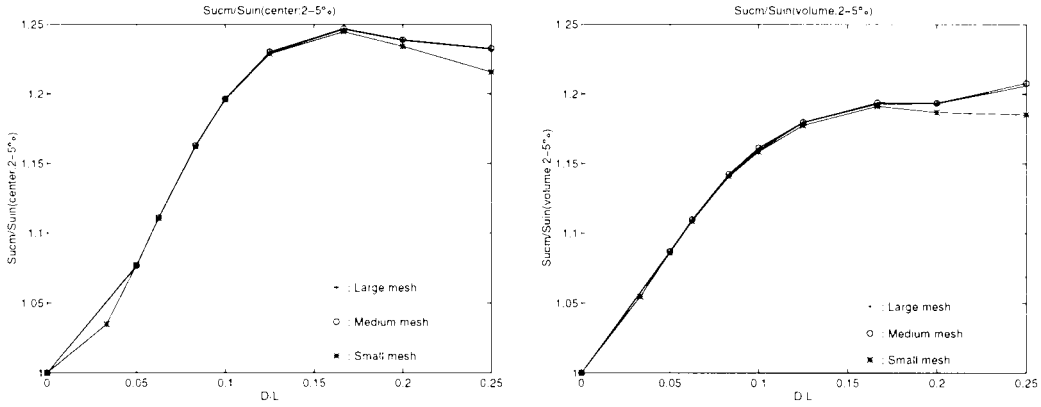


Figure 17: A comparison between corrected measured values of shear strength

used on the figure is the inverse ratio D/L. However, the difference is less than 1.5 % in measured values, which implies that the sizes of the three meshes are sufficiently big.

In addition, as can be seen in Figures 16 and 17, which show the comparison between input and corrected measured values from the case of $I_r = 500$, it is noticed that the difference due to the size of the mesh found in the measured values are still valid in terms of the corrected measured values. This implies that the correction procedure does not eliminate the error caused by the size of the mesh. However, this error is very small and is probably due to boundary effects.

The plastic (yielded) area around pressuremeter depends highly on the length of the pressuremeter and I_r value as is seen in Figures 18 to 20, which shows the zone of plastic potential area occurred at the same pressure of the test. Plots of the plastic areas (Figure 18 to 20) show a detail from the bottom left-hand corner of the large mesh (Figure 11).

Comparing Figure 18 which shows the zone of plastically deforming soil area for $I_r = 50, L/D = 4$ and Figure 19 which shows the zone of plastically deforming soil for $I_r = 500, L/D = 4$, it is found that I_r value affects on the area of the plasticity, especially horizontally. This is due to the shear modulus value. On the other hand, comparing Figures 19 and 20 which shows the zone of plasticity area for $I_r = 500, L/D = 4$ and $I_r = 500, L/D = 10$, it can be seen that the length-to-diameter ratio (L/D) affects the vertical dimension of the plastic zone.

Results of σ_r and shear stress $\tau_{r\theta}$ for the case of $I_r = 500$ with the value of $L/D = 4$ at the same pressure from the large mesh results are shown in Figure 21 and 23. Both the σ_r and the $\tau_{r\theta}$ plots show the behaviour of the finite element analysis in the bottom left-hand corner of the large mesh (Figure 11) . Comparing Figure 21 and 22 which shows the difference between the distribution of σ_r for a finite length case ($L/D = 4$) and for an infinitely long case, an area near the upper end of the pressuremeter has stresses reduced and the area along the pressuremeter is compressed in the finite length case, but the whole area is compressed equally in the infinitely long case.

Comparing Figure 23 and 24 which shows the difference of the distribution of $\tau_{r\theta}$ for a finite length case ($L/D = 4$) and for an infinitely long case, an area near the upper end of the pressuremeter is sheared in the finite length case, in contrast, in the infinitely long case, shear stresses $\tau_{r\theta}$ are calculated to be small (and are in theory zero). (In Figure 24, $\tau_{r\theta}$ seems to vary a lot, however, the value is very small in comparison with the value found in Figure 23.) In summary, from the distribution of σ_r and $\tau_{r\theta}$ that the area near the end of the pressuremeter is partly compressed or sheared, which cannot be seen in an infinitely long case. This results in so-called end-effects and these effects obviously have much influence on pressuremeter tests.

The effects of the length to diameter ratio (L/D) should be closely examined

. but because the pressure-expansion curve depends much on the rigidity index (I_r) attention should be paid also to the latter case . Therefore, these two effects are examined together below. In the following section, the values of the corrected measured shear modulus and strength are discussed.

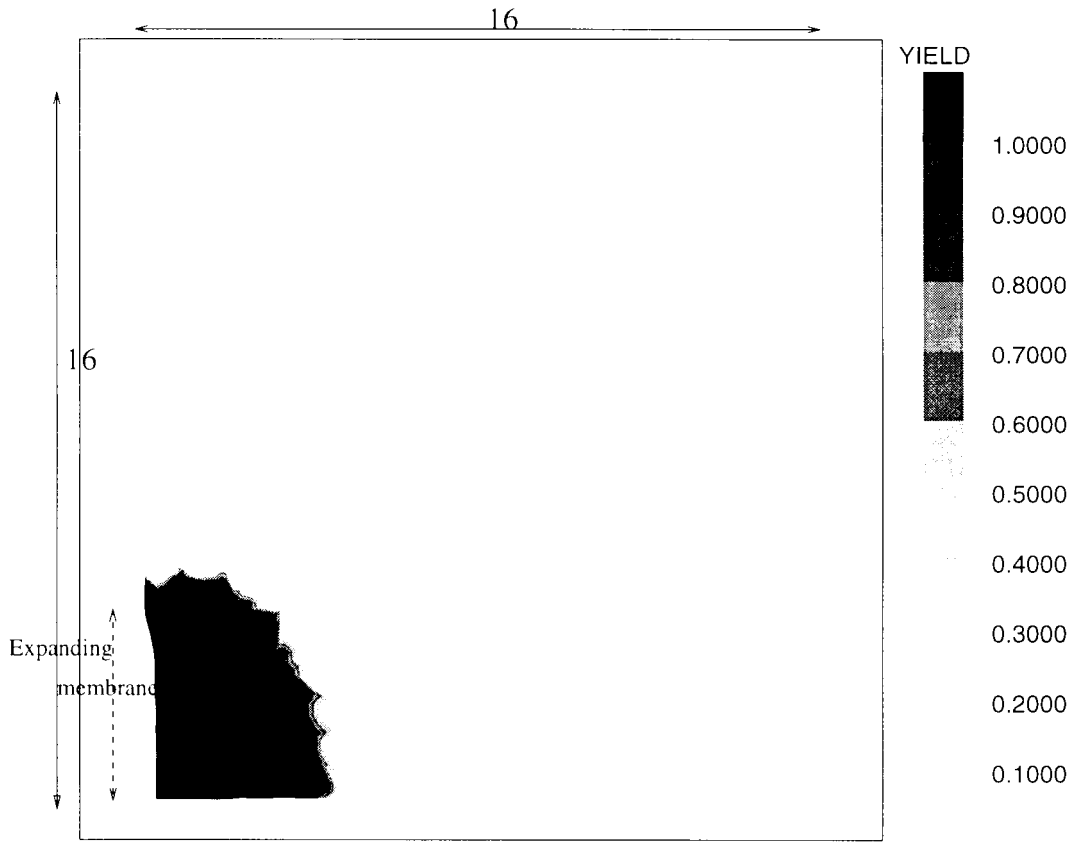


Figure 18: Plastic area for $I_r = 50.\ L/D = 4.$(dark shaded area is the plastically deforming zone)

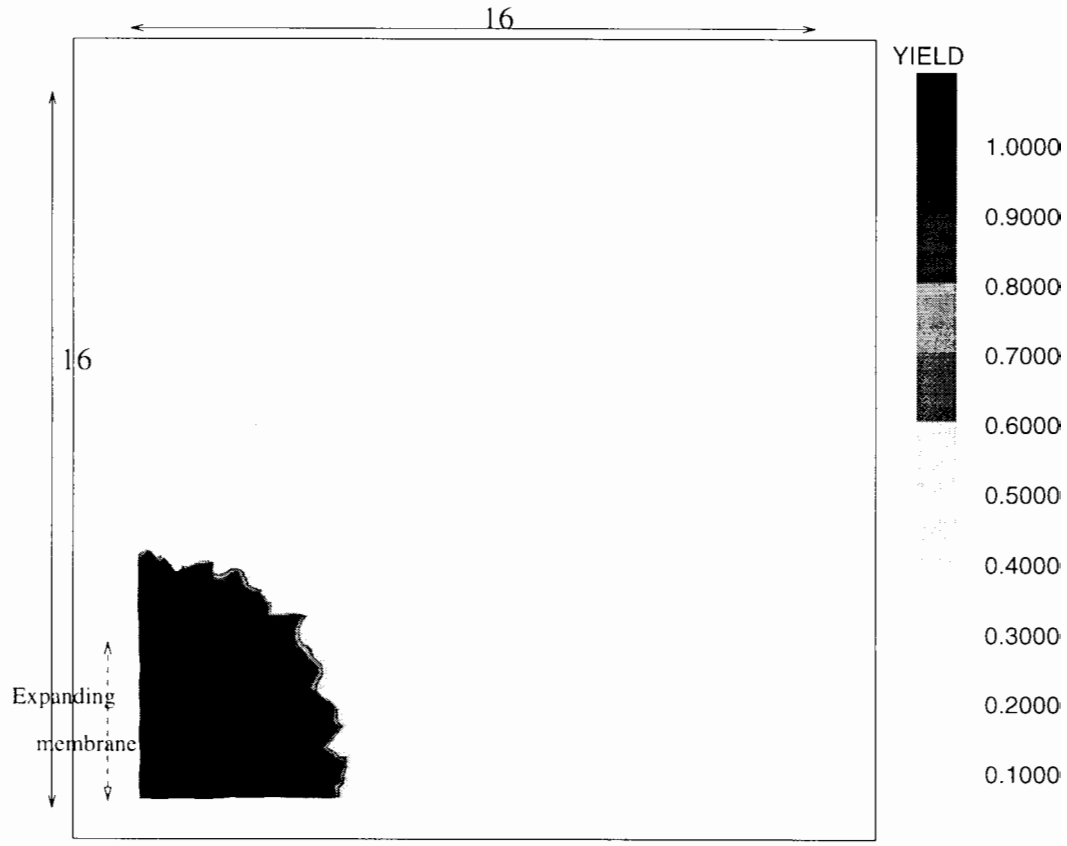


Figure 19: Plastic area for $I_r = 500$. $L/D = 4$.(dark shaded area is the plastically deforming zone)

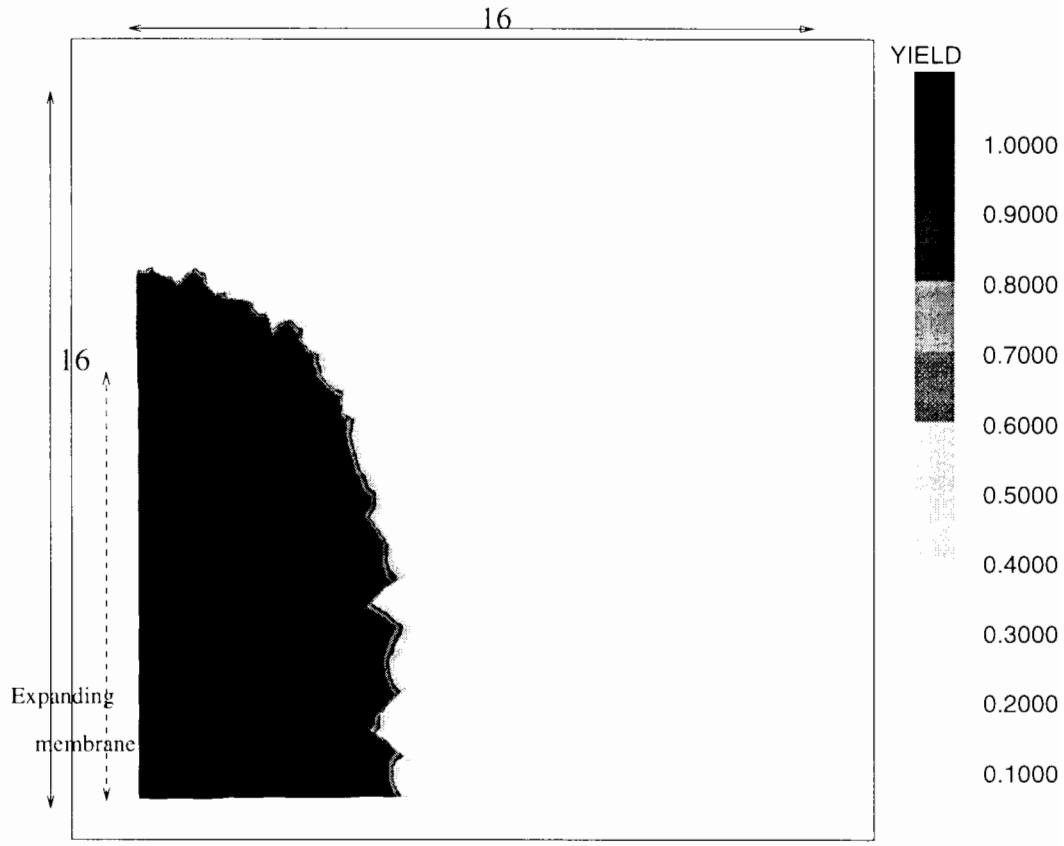


Figure 20: Plastic area for $I_r = 500$. $L/D = 10$.(dark shaded area is the plastically deforming zone)

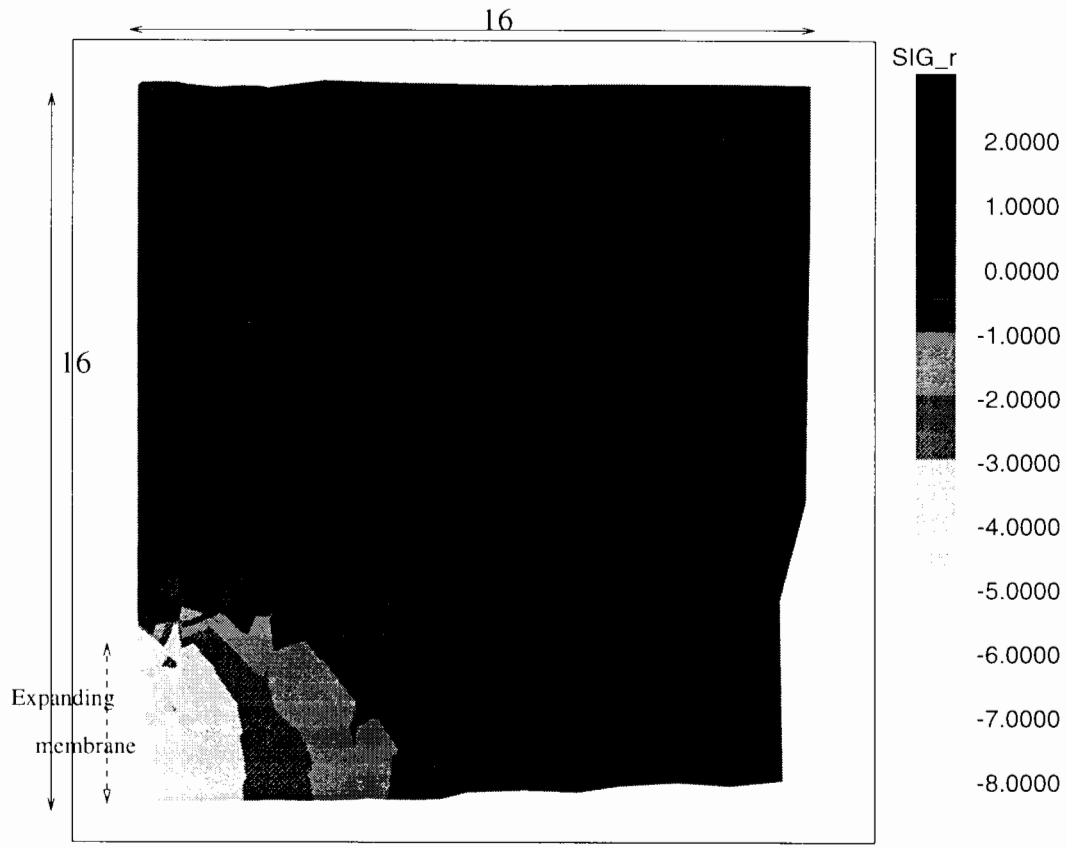


Figure 21: Distribution of σ_r for $I_r = 500, L/D = 4$. (contours at intervals of s_u)

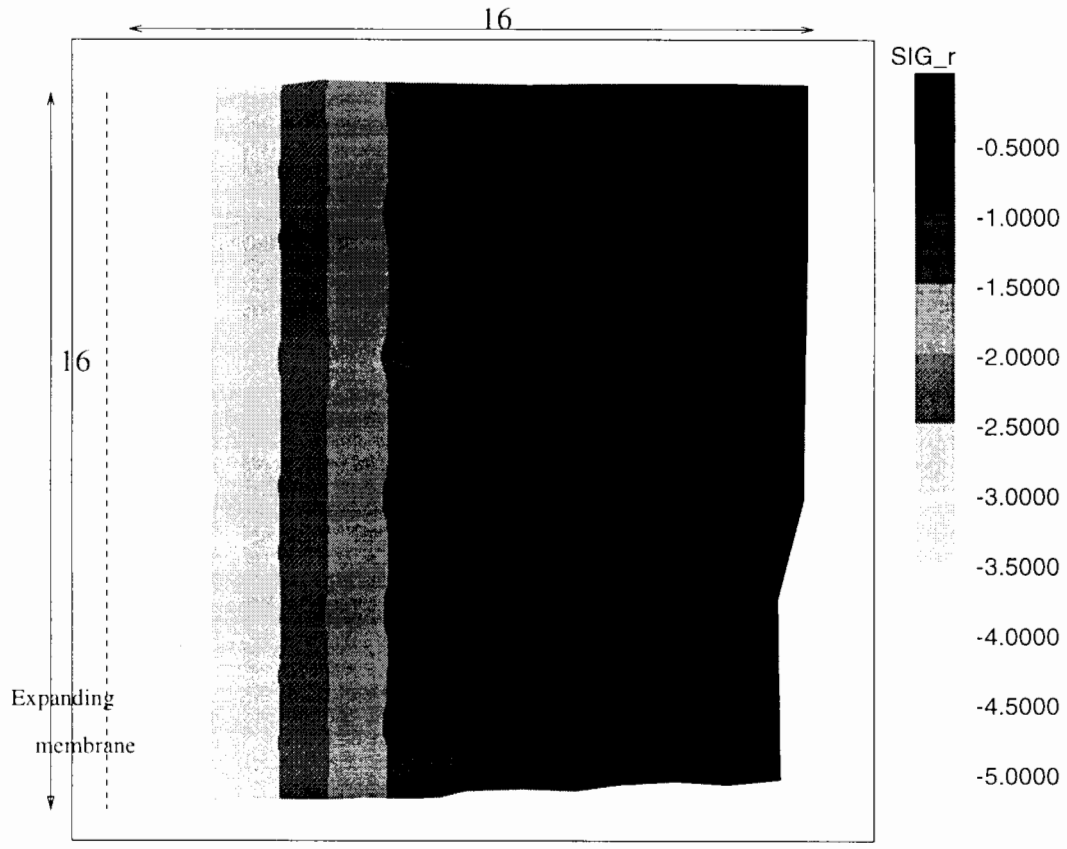


Figure 22: Distribution of σ_r, $I_r = 500$, $L/D = \infty$, (contours at intervals of $0.5s_u$)

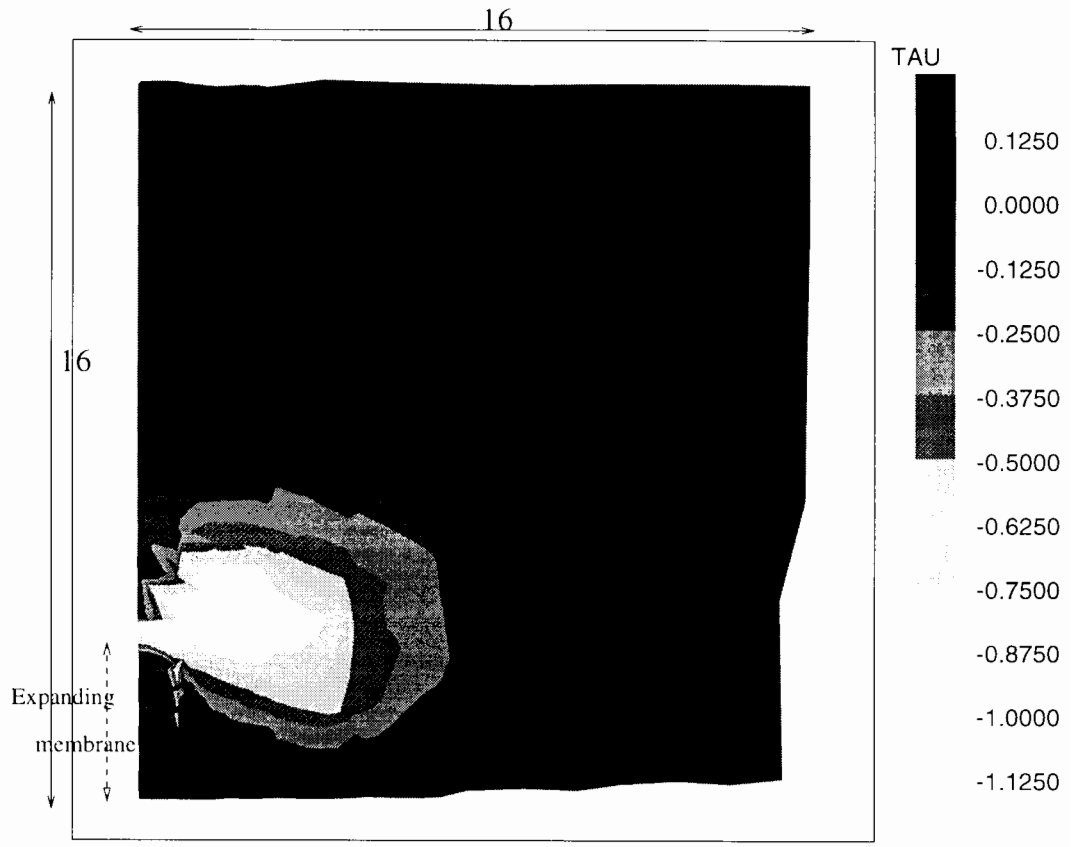


Figure 23: Distribution of τ for $I_r = 500, L/D = 4$. (contours at intervals of $0.125 s_u$)

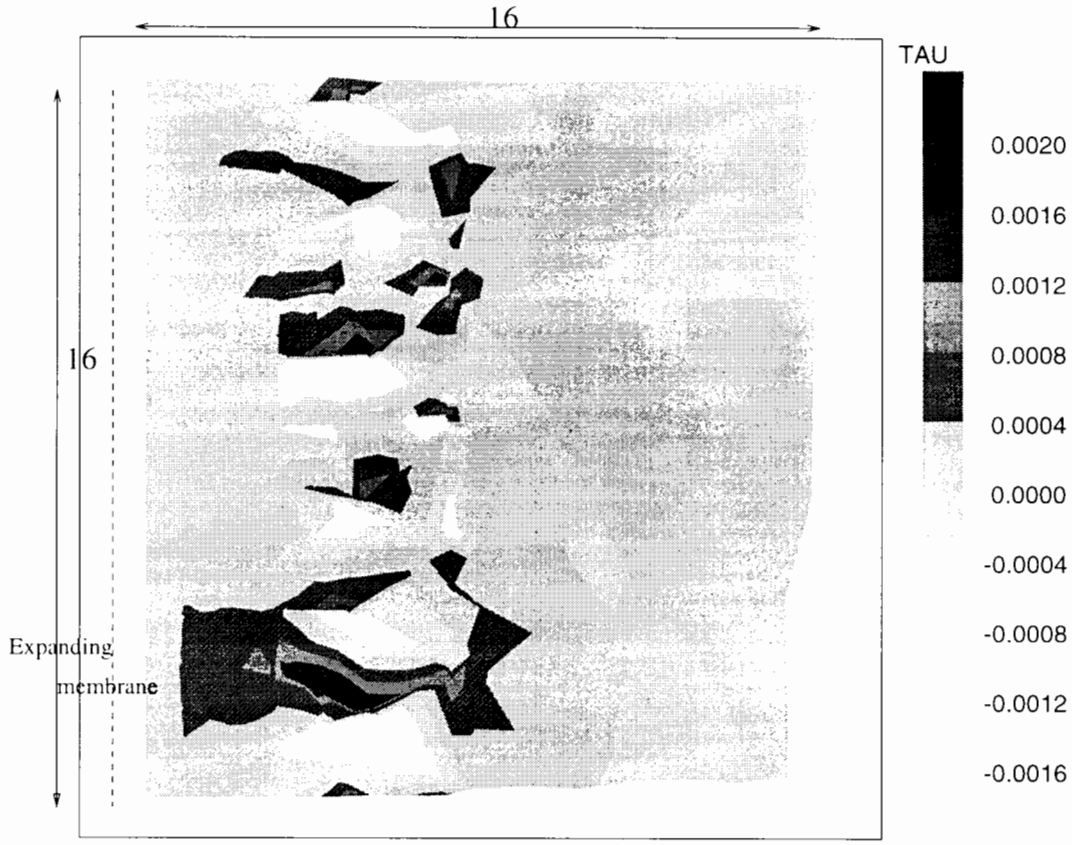


Figure 24: Distribution of $\tau_{r\theta}$ showing small numerical scatter only for $I_r = 500$. $L/D = \infty$. (contours at intervals of $0.0004 s_u$)

input values		central strain				volumetric strain			
I_r	L/D	G_m	Su_m	Su_m	Su_m	G_m	Su_m	Su_m	Su_m
			2%-5%	6%-10%	6%-15%		2%-5%	6%-10%	6%-15%
50	4	51.390	1.180	1.313	1.338	61.040	1.201	1.244	1.276
50	5	50.553	1.121	1.240	1.275	58.005	1.156	1.200	1.225
50	6	50.176	1.087	1.200	1.237	56.572	1.131	1.185	1.200
50	8	49.889	1.047	1.129	1.165	54.667	1.093	1.142	1.158
50	10	49.791	1.027	1.090	1.120	53.568	1.069	1.109	1.125
50	12	49.752	1.015	1.065	1.089	52.879	1.055	1.087	1.101
50	16	49.722	1.006	1.038	1.056	52.027	1.039	1.062	1.072
50	20	49.711	1.001	1.025	1.038	51.517	1.029	1.046	1.054
50	∞	49.709	0.991	0.991	0.993	49.566	0.995	0.993	0.993
100	4	102.997	1.258	1.322	1.330	122.312	1.214	1.260	1.281
100	5	101.338	1.191	1.290	1.302	116.255	1.165	1.218	1.238
100	6	100.587	1.151	1.266	1.289	113.388	1.152	1.203	1.225
100	8	100.018	1.095	1.208	1.237	109.578	1.113	1.167	1.191
100	10	99.824	1.062	1.160	1.190	107.382	1.088	1.141	1.162
100	12	99.747	1.042	1.124	1.150	106.004	1.070	1.116	1.138
100	16	99.688	1.022	1.080	1.100	104.300	1.049	1.085	1.101
100	20	99.668	1.012	1.056	1.071	103.280	1.036	1.064	1.077
100	∞	99.666	0.994	0.998	0.996	99.377	0.993	0.997	0.996
200	4	206.213	1.274	1.280	1.293	244.856	1.214	1.258	1.280
200	5	202.909	1.248	1.272	1.280	232.757	1.190	1.230	1.247
200	6	201.409	1.216	1.278	1.288	227.020	1.174	1.220	1.236
200	8	200.276	1.157	1.257	1.277	219.401	1.143	1.201	1.219
200	10	199.891	1.114	1.221	1.247	215.009	1.116	1.180	1.200
200	12	199.737	1.083	1.184	1.213	212.253	1.096	1.156	1.176
200	16	199.621	1.049	1.128	1.158	208.845	1.069	1.120	1.137
200	20	199.582	1.030	1.090	1.114	206.807	1.053	1.093	1.109
200	∞	199.581	0.996	0.995	0.996	198.999	0.996	0.996	0.997
500	4	515.861	1.229	1.254	1.282	612.489	1.203	1.266	1.288
500	5	507.621	1.235	1.237	1.248	582.263	1.190	1.225	1.245
500	6	503.875	1.243	1.239	1.252	567.916	1.190	1.220	1.238
500	8	501.051	1.226	1.254	1.264	548.871	1.176	1.210	1.229
500	10	500.092	1.193	1.254	1.268	537.890	1.157	1.206	1.222
500	12	499.709	1.159	1.243	1.261	531.003	1.139	1.193	1.207
500	16	499.420	1.108	1.205	1.229	522.483	1.106	1.162	1.180
500	20	499.324	1.073	1.160	1.187	517.388	1.084	1.133	1.152
500	∞	499.324	0.997	0.996	0.998	497.864	0.998	0.997	0.998
1000	4	1031.940	1.202	1.264	1.293	1225.211	1.203	1.274	1.304
1000	5	1015.476	1.200	1.233	1.249	1164.772	1.182	1.236	1.251
1000	6	1007.985	1.215	1.227	1.247	1136.075	1.186	1.218	1.245
1000	8	1002.342	1.229	1.228	1.242	1097.988	1.185	1.213	1.229
1000	10	1000.427	1.225	1.241	1.249	1076.025	1.177	1.209	1.225
1000	12	999.663	1.206	1.245	1.252	1062.252	1.164	1.202	1.217
1000	16	999.084	1.164	1.235	1.246	1045.212	1.136	1.184	1.197
1000	20	998.894	1.123	1.208	1.224	1035.024	1.110	1.164	1.174
1000	∞	998.897	0.998	0.998	0.999	995.972	0.998	0.998	0.999

Table 2: Results of measured values from finite element analysis of self-boring pressuremter with the small mesh (see text for definitions of variables)

input values		central strain				volumetric strain			
I_r	L/D	G_m	Su_m	Su_m	Su_m	G_m	Su_m	Su_m	Su_m
			2%-5%	6%-10%	6%-15%		2%-5%	6%-10%	6%-15%
50	4	51.385	1.180	1.313	1.338	61.038	1.201	1.244	1.275
50	5	50.549	1.121	1.240	1.275	58.001	1.156	1.200	1.225
50	6	50.174	1.087	1.200	1.237	56.572	1.131	1.184	1.201
50	8	49.888	1.047	1.129	1.165	54.668	1.093	1.142	1.158
50	10	49.789	1.027	1.090	1.121	53.567	1.069	1.109	1.125
50	12	49.749	1.015	1.065	1.089	52.877	1.055	1.087	1.101
50	16	49.718	1.006	1.038	1.056	52.023	1.039	1.062	1.072
50	20	49.707	1.001	1.025	1.038	51.514	1.029	1.046	1.054
50	∞	49.709	0.990	0.991	0.993	49.553	0.995	0.992	0.993
100	4	102.988	1.258	1.322	1.330	122.309	1.214	1.259	1.279
100	5	101.331	1.191	1.290	1.302	116.248	1.165	1.217	1.237
100	6	100.583	1.151	1.266	1.289	113.388	1.152	1.203	1.226
100	8	100.016	1.095	1.208	1.237	109.581	1.113	1.167	1.191
100	10	99.820	1.062	1.160	1.190	107.378	1.088	1.142	1.162
100	12	99.741	1.042	1.124	1.150	105.999	1.070	1.118	1.138
100	16	99.681	1.022	1.080	1.101	104.293	1.049	1.085	1.102
100	20	99.660	1.012	1.056	1.071	103.275	1.036	1.064	1.077
100	∞	99.666	0.994	0.998	0.996	99.350	0.993	0.995	0.995
200	4	206.194	1.274	1.278	1.294	244.851	1.214	1.257	1.281
200	5	202.895	1.248	1.273	1.280	232.742	1.190	1.231	1.247
200	6	201.402	1.216	1.279	1.288	227.020	1.174	1.219	1.236
200	8	200.272	1.157	1.256	1.277	219.408	1.143	1.201	1.219
200	10	199.883	1.114	1.221	1.248	215.002	1.117	1.179	1.200
200	12	199.727	1.083	1.184	1.214	212.245	1.097	1.156	1.176
200	16	199.608	1.049	1.128	1.158	208.831	1.070	1.121	1.138
200	20	199.567	1.030	1.090	1.115	206.796	1.053	1.094	1.109
200	∞	199.580	0.995	0.995	0.996	198.945	0.995	0.996	0.996
500	4	515.813	1.229	1.252	1.280	612.476	1.205	1.263	1.289
500	5	507.588	1.235	1.236	1.248	582.226	1.190	1.230	1.245
500	6	503.857	1.243	1.241	1.252	567.917	1.191	1.219	1.237
500	8	501.041	1.227	1.255	1.263	548.888	1.176	1.216	1.229
500	10	500.071	1.193	1.258	1.269	537.873	1.158	1.211	1.222
500	12	499.682	1.160	1.248	1.263	530.982	1.139	1.193	1.209
500	16	499.388	1.108	1.207	1.231	522.448	1.107	1.160	1.182
500	20	499.286	1.074	1.163	1.189	517.361	1.084	1.135	1.154
500	∞	499.323	0.997	0.996	0.998	497.728	0.997	0.996	0.998
1000	4	1031.844	1.201	1.259	1.290	1225.184	1.200	1.278	1.305
1000	5	1015.408	1.200	1.234	1.247	1164.698	1.182	1.232	1.249
1000	6	1007.950	1.215	1.223	1.245	1136.078	1.186	1.218	1.244
1000	8	1002.322	1.230	1.232	1.242	1098.021	1.186	1.211	1.229
1000	10	1000.385	1.225	1.244	1.251	1075.992	1.178	1.210	1.224
1000	12	999.609	1.208	1.246	1.253	1062.210	1.165	1.201	1.216
1000	16	999.020	1.166	1.236	1.247	1045.141	1.137	1.185	1.199
1000	20	998.819	1.124	1.211	1.228	1034.968	1.113	1.168	1.179
1000	∞	998.895	0.998	0.997	0.997	995.701	0.999	0.996	0.998

Table 3: Results of measured values from finite element analysis of self-boring pressuremter with the medium mesh (see text for definitions of variables)

input values		central strain				volumetric strain			
I_r	L/D	G_m	Su_m	Su_m	Su_m	G_m	Su_m	Su_m	Su_m
			2%-5%	6%-10%	6%-15%		2%-5%	6%-10%	6%-15%
50	4	51.004	1.177	1.292	1.315	60.466	1.199	1.229	1.242
50	5	50.456	1.119	1.248	1.280	58.121	1.161	1.206	1.221
50	6	50.154	1.083	1.200	1.234	56.479	1.128	1.172	1.195
50	8	49.895	1.044	1.131	1.163	54.587	1.091	1.133	1.151
50	10	49.801	1.023	1.093	1.118	53.558	1.068	1.105	1.119
50	12	49.760	1.013	1.067	1.088	52.857	1.054	1.085	1.099
50	16	49.727	1.003	1.042	1.056	52.056	1.037	1.064	1.070
50	20	49.715	0.999	1.028	1.039	51.572	1.027	1.052	1.055
50	30	49.705	0.994	1.012	1.019	50.932	1.015	1.031	1.033
50	∞	49.719	0.987	0.993	0.993	49.564	0.990	0.997	0.994
100	4	102.229	1.245	1.300	1.302	121.172	1.201	1.228	1.244
100	5	101.142	1.198	1.292	1.305	116.485	1.182	1.222	1.235
100	6	100.543	1.151	1.267	1.289	113.202	1.146	1.207	1.226
100	8	100.030	1.094	1.206	1.235	109.419	1.111	1.169	1.189
100	10	99.844	1.062	1.157	1.189	107.362	1.085	1.142	1.162
100	12	99.764	1.041	1.121	1.148	105.961	1.069	1.113	1.134
100	16	99.699	1.021	1.077	1.099	104.359	1.049	1.083	1.100
100	20	99.675	1.012	1.054	1.071	103.391	1.038	1.064	1.077
100	30	99.657	1.003	1.027	1.037	102.111	1.022	1.038	1.047
100	∞	99.686	0.995	0.995	0.995	99.373	0.994	0.994	0.995
200	4	204.680	1.263	1.249	1.259	242.585	1.196	1.220	1.237
200	5	202.514	1.247	1.266	1.273	233.213	1.187	1.213	1.231
200	6	201.321	1.216	1.277	1.285	226.648	1.173	1.221	1.236
200	8	200.302	1.156	1.254	1.274	219.083	1.140	1.199	1.217
200	10	199.932	1.113	1.219	1.246	214.971	1.113	1.177	1.196
200	12	199.773	1.083	1.182	1.212	212.169	1.094	1.155	1.173
200	16	199.644	1.049	1.128	1.157	208.966	1.066	1.119	1.136
200	20	199.596	1.029	1.092	1.115	207.029	1.051	1.092	1.107
200	30	199.561	1.011	1.046	1.061	204.469	1.030	1.058	1.069
200	∞	199.621	0.996	0.994	0.996	198.991	0.995	0.996	0.997
500	4	512.033	1.212	1.220	1.244	606.823	1.182	1.223	1.249
500	5	506.631	1.231	1.230	1.238	583.398	1.184	1.207	1.227
500	6	503.657	1.241	1.235	1.249	566.988	1.188	1.218	1.234
500	8	501.116	1.225	1.251	1.259	548.078	1.174	1.208	1.225
500	10	500.195	1.192	1.253	1.265	537.797	1.156	1.202	1.220
500	12	499.799	1.159	1.239	1.259	530.794	1.138	1.188	1.206
500	16	499.478	1.108	1.200	1.228	522.786	1.106	1.162	1.179
500	20	499.358	1.074	1.158	1.188	517.944	1.083	1.133	1.149
500	30	499.272	1.032	1.089	1.114	511.543	1.052	1.089	1.102
500	∞	499.425	0.997	0.995	0.997	497.845	0.998	0.997	0.998
1000	4	1024.289	1.184	1.229	1.256	1213.886	1.178	1.234	1.265
1000	5	1013.493	1.200	1.212	1.229	1167.040	1.180	1.212	1.224
1000	6	1007.550	1.211	1.222	1.236	1134.221	1.184	1.212	1.235
1000	8	1002.473	1.227	1.222	1.235	1096.402	1.182	1.208	1.223
1000	10	1000.634	1.224	1.233	1.240	1075.840	1.175	1.208	1.219
1000	12	999.842	1.207	1.241	1.246	1061.835	1.162	1.204	1.212
1000	16	999.202	1.163	1.237	1.242	1045.820	1.136	1.181	1.192
1000	20	998.963	1.123	1.210	1.223	1036.135	1.112	1.160	1.170
1000	30	998.791	1.060	1.139	1.157	1023.334	1.073	1.114	1.124
1000	∞	999.098	0.998	0.999	0.999	995.936	0.998	0.999	0.999

Table 4: Results of measured values from finite element analysis of self-boring pressuremter with the large mesh (see text for definitions of variables)

input values		central strain				volumetric strain			
I_r	L/D	$\frac{G_{cm}}{G_{in}}$	$\frac{Su_{cm}}{Su_{in}}$	$\frac{Su_{cm}}{Su_{in}}$	$\frac{Su_{cm}}{Su_{in}}$	$\frac{G_{cm}}{G_{in}}$	$\frac{Su_{cm}}{Su_{in}}$	$\frac{Su_{cm}}{Su_{in}}$	$\frac{Su_{cm}}{Su_{in}}$
			2%-5%	6%-10%	6%-15%		2%-5%	6%-10%	6%-15%
50	4	1.034	1.191	1.324	1.348	1.231	1.207	1.253	1.284
50	5	1.017	1.132	1.251	1.284	1.170	1.162	1.209	1.233
50	6	1.009	1.098	1.210	1.246	1.141	1.136	1.193	1.208
50	8	1.004	1.057	1.139	1.174	1.103	1.098	1.150	1.166
50	10	1.002	1.036	1.100	1.129	1.081	1.074	1.117	1.133
50	12	1.001	1.025	1.074	1.097	1.067	1.061	1.095	1.108
50	16	1.000	1.015	1.047	1.063	1.050	1.044	1.070	1.079
50	20	1.000	1.011	1.034	1.045	1.039	1.034	1.054	1.061
50	∞	1.000	1.000	1.000	1.000	1.000	1.000	1.000	1.000
100	4	1.033	1.265	1.324	1.336	1.231	1.222	1.264	1.286
100	5	1.017	1.198	1.292	1.307	1.170	1.173	1.222	1.244
100	6	1.009	1.158	1.269	1.294	1.141	1.160	1.208	1.230
100	8	1.004	1.101	1.210	1.243	1.103	1.121	1.171	1.196
100	10	1.002	1.068	1.162	1.195	1.081	1.096	1.145	1.167
100	12	1.001	1.048	1.126	1.155	1.067	1.078	1.120	1.143
100	16	1.000	1.028	1.082	1.105	1.050	1.056	1.089	1.106
100	20	1.000	1.018	1.058	1.075	1.039	1.043	1.067	1.081
100	∞	1.000	1.000	1.000	1.000	1.000	1.000	1.000	1.000
200	4	1.033	1.280	1.287	1.299	1.230	1.219	1.263	1.284
200	5	1.017	1.253	1.279	1.285	1.170	1.196	1.235	1.251
200	6	1.009	1.221	1.285	1.293	1.141	1.179	1.225	1.240
200	8	1.003	1.162	1.263	1.282	1.103	1.148	1.206	1.223
200	10	1.002	1.119	1.227	1.252	1.080	1.121	1.185	1.204
200	12	1.001	1.088	1.190	1.218	1.067	1.101	1.161	1.180
200	16	1.000	1.054	1.134	1.162	1.049	1.074	1.125	1.141
200	20	1.000	1.034	1.096	1.119	1.039	1.057	1.098	1.112
200	∞	1.000	1.000	1.000	1.000	1.000	1.000	1.000	1.000
500	4	1.033	1.232	1.259	1.285	1.230	1.206	1.270	1.291
500	5	1.017	1.238	1.242	1.252	1.170	1.193	1.228	1.248
500	6	1.009	1.246	1.244	1.255	1.141	1.193	1.223	1.241
500	8	1.003	1.230	1.259	1.267	1.102	1.179	1.214	1.232
500	10	1.002	1.196	1.259	1.271	1.080	1.160	1.210	1.225
500	12	1.001	1.162	1.247	1.265	1.067	1.141	1.196	1.210
500	16	1.000	1.111	1.209	1.232	1.049	1.109	1.165	1.183
500	20	1.000	1.076	1.164	1.190	1.039	1.086	1.137	1.154
500	∞	1.000	1.000	1.000	1.000	1.000	1.000	1.000	1.000
1000	4	1.033	1.205	1.267	1.295	1.230	1.206	1.276	1.306
1000	5	1.017	1.203	1.235	1.250	1.169	1.184	1.238	1.252
1000	6	1.009	1.217	1.230	1.248	1.141	1.189	1.220	1.246
1000	8	1.003	1.232	1.231	1.244	1.102	1.187	1.215	1.230
1000	10	1.002	1.228	1.244	1.251	1.080	1.179	1.211	1.226
1000	12	1.001	1.209	1.248	1.254	1.067	1.166	1.204	1.218
1000	16	1.000	1.167	1.237	1.247	1.049	1.139	1.186	1.199
1000	20	1.000	1.125	1.211	1.226	1.039	1.112	1.166	1.175
1000	∞	1.000	1.000	1.000	1.000	1.000	1.000	1.000	1.000

Table 5: Results of corrected measured values divided by input values from finite element analysis of self-boring pressuremeter with the small mesh (see text for definitions of variables)

input values		central strain				volumetric strain			
I_r	L/D	$\frac{G_{cm}}{G_{in}}$	$\frac{Su_{cm}}{Su_{in}}$ 2%-5%	$\frac{Su_{cm}}{Su_{in}}$ 6%-10%	$\frac{Su_{cm}}{Su_{in}}$ 6%-15%	$\frac{G_{cm}}{G_{in}}$	$\frac{Su_{cm}}{Su_{in}}$ 2%-5%	$\frac{Su_{cm}}{Su_{in}}$ 6%-10%	$\frac{Su_{cm}}{Su_{in}}$ 6%-15%
50	4	1.034	1.191	1.325	1.348	1.232	1.208	1.253	1.284
50	5	1.017	1.132	1.251	1.284	1.170	1.162	1.209	1.233
50	6	1.009	1.098	1.210	1.246	1.142	1.137	1.194	1.209
50	8	1.004	1.057	1.139	1.174	1.103	1.099	1.151	1.167
50	10	1.002	1.037	1.100	1.129	1.081	1.075	1.117	1.133
50	12	1.001	1.025	1.075	1.097	1.067	1.061	1.095	1.109
50	16	1.000	1.016	1.048	1.064	1.050	1.044	1.070	1.079
50	20	1.000	1.011	1.034	1.046	1.040	1.035	1.055	1.061
50	∞	1.000	1.000	1.000	1.000	1.000	1.000	1.000	1.000
100	4	1.033	1.265	1.325	1.336	1.231	1.222	1.265	1.285
100	5	1.017	1.197	1.293	1.307	1.170	1.173	1.223	1.243
100	6	1.009	1.158	1.269	1.295	1.141	1.160	1.209	1.231
100	8	1.004	1.101	1.211	1.243	1.103	1.121	1.172	1.196
100	10	1.002	1.068	1.163	1.196	1.081	1.095	1.147	1.168
100	12	1.001	1.048	1.127	1.155	1.067	1.077	1.123	1.143
100	16	1.000	1.027	1.083	1.106	1.050	1.056	1.090	1.107
100	20	1.000	1.018	1.059	1.076	1.040	1.043	1.069	1.082
100	∞	1.000	1.000	1.000	1.000	1.000	1.000	1.000	1.000
200	4	1.033	1.280	1.285	1.300	1.231	1.219	1.263	1.286
200	5	1.017	1.254	1.280	1.286	1.170	1.196	1.236	1.251
200	6	1.009	1.222	1.286	1.293	1.141	1.179	1.224	1.241
200	8	1.003	1.162	1.263	1.283	1.103	1.148	1.206	1.223
200	10	1.002	1.119	1.228	1.253	1.081	1.122	1.184	1.204
200	12	1.001	1.088	1.191	1.219	1.067	1.102	1.161	1.180
200	16	1.000	1.054	1.134	1.163	1.050	1.075	1.125	1.142
200	20	1.000	1.035	1.096	1.119	1.039	1.058	1.098	1.113
200	∞	1.000	1.000	1.000	1.000	1.000	1.000	1.000	1.000
500	4	1.033	1.233	1.258	1.283	1.231	1.208	1.268	1.292
500	5	1.017	1.239	1.241	1.251	1.170	1.194	1.234	1.248
500	6	1.009	1.247	1.246	1.255	1.141	1.194	1.223	1.239
500	8	1.003	1.230	1.260	1.266	1.103	1.180	1.221	1.232
500	10	1.001	1.196	1.263	1.272	1.081	1.161	1.216	1.225
500	12	1.001	1.163	1.253	1.265	1.067	1.142	1.197	1.211
500	16	1.000	1.111	1.212	1.233	1.050	1.110	1.164	1.184
500	20	1.000	1.077	1.167	1.192	1.039	1.087	1.139	1.156
500	∞	1.000	1.000	1.000	1.000	1.000	1.000	1.000	1.000
1000	4	1.033	1.203	1.264	1.293	1.230	1.202	1.282	1.308
1000	5	1.017	1.202	1.238	1.250	1.170	1.183	1.236	1.252
1000	6	1.009	1.217	1.227	1.248	1.141	1.187	1.223	1.247
1000	8	1.003	1.231	1.236	1.245	1.103	1.187	1.216	1.232
1000	10	1.001	1.227	1.248	1.254	1.081	1.180	1.214	1.227
1000	12	1.001	1.210	1.250	1.257	1.067	1.167	1.205	1.219
1000	16	1.000	1.167	1.240	1.251	1.050	1.138	1.190	1.202
1000	20	1.000	1.126	1.215	1.231	1.039	1.114	1.172	1.182
1000	∞	1.000	1.000	1.000	1.000	1.000	1.000	1.000	1.000

Table 6: Results of corrected measured values divided by input values from finite element analysis of self-boring pressuremeter with the medium mesh (see text for definitions of variables)

input values		central strain				volumetric strain			
I_r	L/D	$\frac{G_{cm}}{G_{in}}$	$\frac{Su_{cm}}{Su_{in}}$ 2%-5%	$\frac{Su_{cm}}{Su_{in}}$ 6%-10%	$\frac{Su_{cm}}{Su_{in}}$ 6%-15%	$\frac{G_{cm}}{G_{in}}$	$\frac{Su_{cm}}{Su_{in}}$ 2%-5%	$\frac{Su_{cm}}{Su_{in}}$ 6%-10%	$\frac{Su_{cm}}{Su_{in}}$ 6%-15%
50	4	1.026	1.192	1.301	1.325	1.220	1.210	1.233	1.250
50	5	1.015	1.134	1.257	1.290	1.173	1.173	1.210	1.229
50	6	1.009	1.098	1.209	1.243	1.140	1.139	1.176	1.203
50	8	1.004	1.058	1.139	1.172	1.101	1.102	1.137	1.158
50	10	1.002	1.036	1.100	1.127	1.081	1.079	1.109	1.127
50	12	1.001	1.026	1.075	1.096	1.066	1.065	1.089	1.106
50	16	1.000	1.016	1.050	1.064	1.050	1.047	1.067	1.077
50	20	1.000	1.012	1.035	1.047	1.041	1.037	1.055	1.062
50	30	1.000	1.007	1.019	1.026	1.028	1.025	1.035	1.039
50	∞	1.000	1.000	1.000	1.000	1.000	1.000	1.000	1.000
100	4	1.026	1.251	1.306	1.309	1.219	1.208	1.235	1.250
100	5	1.015	1.204	1.298	1.312	1.172	1.189	1.229	1.241
100	6	1.009	1.157	1.273	1.295	1.139	1.153	1.213	1.233
100	8	1.003	1.100	1.212	1.242	1.101	1.118	1.175	1.196
100	10	1.002	1.068	1.163	1.195	1.080	1.092	1.148	1.168
100	12	1.001	1.047	1.126	1.155	1.066	1.075	1.120	1.140
100	16	1.000	1.027	1.082	1.105	1.050	1.055	1.089	1.106
100	20	1.000	1.018	1.059	1.077	1.040	1.044	1.070	1.082
100	30	1.000	1.008	1.032	1.042	1.028	1.028	1.044	1.053
100	∞	1.000	1.000	1.000	1.000	1.000	1.000	1.000	1.000
200	4	1.025	1.269	1.256	1.264	1.219	1.202	1.225	1.241
200	5	1.014	1.253	1.273	1.278	1.172	1.193	1.218	1.235
200	6	1.009	1.222	1.284	1.290	1.139	1.179	1.226	1.240
200	8	1.003	1.161	1.261	1.279	1.101	1.146	1.204	1.221
200	10	1.002	1.117	1.226	1.251	1.080	1.119	1.182	1.200
200	12	1.001	1.087	1.189	1.217	1.066	1.099	1.160	1.177
200	16	1.000	1.053	1.135	1.162	1.050	1.071	1.124	1.140
200	20	1.000	1.034	1.098	1.120	1.040	1.057	1.096	1.111
200	30	1.000	1.016	1.052	1.065	1.028	1.036	1.063	1.072
200	∞	1.000	1.000	1.000	1.000	1.000	1.000	1.000	1.000
500	4	1.025	1.216	1.227	1.247	1.219	1.185	1.227	1.252
500	5	1.014	1.234	1.237	1.241	1.172	1.187	1.211	1.229
500	6	1.008	1.244	1.241	1.252	1.139	1.191	1.222	1.237
500	8	1.003	1.229	1.257	1.263	1.101	1.177	1.212	1.228
500	10	1.002	1.196	1.260	1.268	1.080	1.158	1.206	1.223
500	12	1.001	1.162	1.246	1.262	1.066	1.141	1.192	1.208
500	16	1.000	1.111	1.206	1.231	1.050	1.108	1.165	1.181
500	20	1.000	1.077	1.165	1.191	1.040	1.086	1.136	1.152
500	30	1.000	1.035	1.095	1.117	1.028	1.055	1.093	1.104
500	∞	1.000	1.000	1.000	1.000	1.000	1.000	1.000	1.000
1000	4	1.025	1.187	1.230	1.258	1.219	1.181	1.235	1.266
1000	5	1.014	1.203	1.213	1.230	1.172	1.182	1.212	1.226
1000	6	1.008	1.214	1.223	1.238	1.139	1.186	1.213	1.236
1000	8	1.003	1.230	1.223	1.237	1.101	1.184	1.209	1.224
1000	10	1.002	1.227	1.234	1.242	1.080	1.177	1.209	1.220
1000	12	1.001	1.209	1.243	1.248	1.066	1.164	1.204	1.213
1000	16	1.000	1.166	1.238	1.244	1.050	1.138	1.182	1.193
1000	20	1.000	1.126	1.211	1.225	1.040	1.114	1.161	1.171
1000	30	1.000	1.063	1.140	1.159	1.028	1.075	1.114	1.125
1000	∞	1.000	1.000	1.000	1.000	1.000	1.000	1.000	1.000

Table 7: Results of corrected measured values divided by input values from finite element analysis of self-boring pressuremeter with the large mesh (see text for definitions of variables)

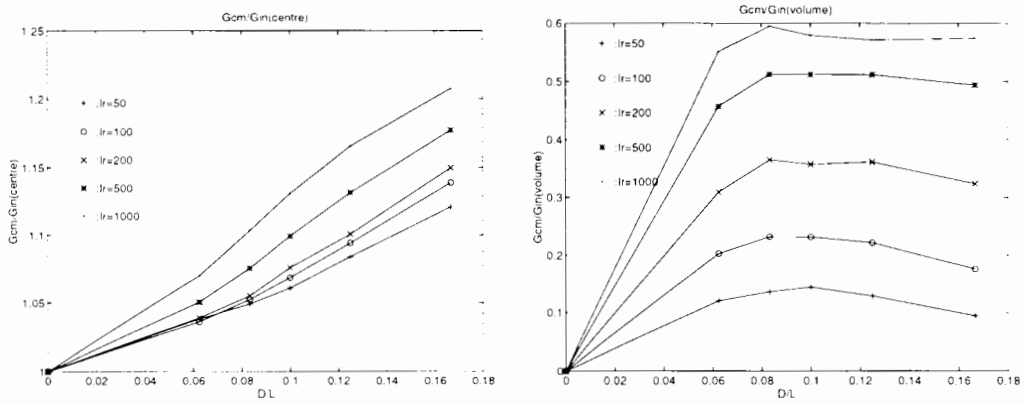


Figure 25: The effects of the length-to-diameter ratio on shear modulus

Shear stiffness

The effects of the length-to-diameter ratio on shear modulus are seen in Figure 25. It can be said that corrected measured shear modulus is overestimated more as the pressuremeter length reduces both when central hoop strain and when volumetric hoop strain is taken into account. All of the results fall on the same line in both cases, which indicates that the effect of the rigidity index is very small if the L/D ratio is the same. This confirms the expected result. It appears that the overestimation found in shear moduli derived from the central hoop strain has a maximum value of less than 2.5 %, which is not as large as the overestimation found when using volumetric hoop strain. This is not a surprising fact if the shape of the pressuremeter is taken into account. The overestimation in the values derived from the central strain get larger rapidly after the D/L ratio is over 0.1, which indicates that a pressuremeter with L/D equal to more than 10 is adequate in measuring shear modulus, using central hoop strain. As for the overestimation found in volumetric hoop strain, it is almost linear with the D/L ratio and the effects of the rigidity index on the shear modulus are negligible as is found in central hoop strain. However, the overestimation is large even for a small D/L value, which means that much attention should be paid in measuring shear modulus using volumetric hoop strain.

From Figures 25 and 26, it is found that the value of G_{cm}/G_{in} is almost the

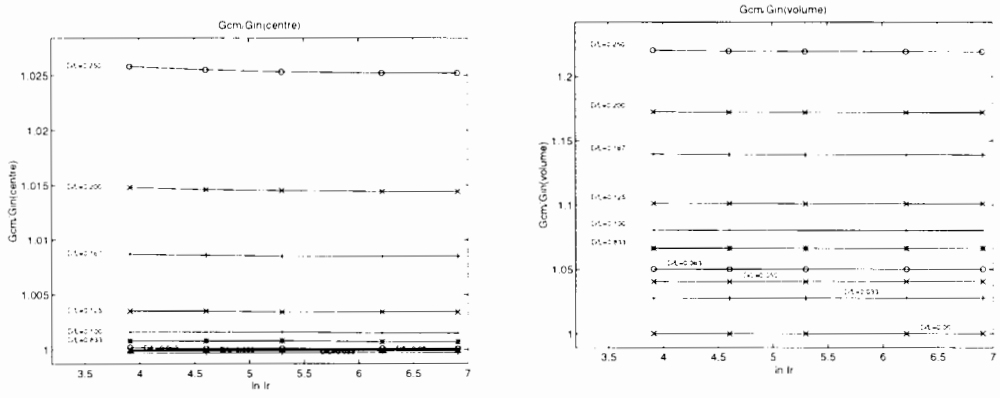


Figure 26: The effects of the rigidity index on shear modulus

same for the same L/D ratio, but different for I_r both in central hoop strain case and volumetric hoop strain case. The difference due to the rigidity index is less than 1 %. This confirms that the effects of the rigidity index on measuring shear modulus by the pressuremeter has no significance. It is found that the the overestimation decrease very slightly as the rigidity index increase both in central case and volumetric case.

It is concluded that the effect of the length-to-diameter is satisfactorily small (less than 2.6%) when central hoop strain is taken into account, however, the effect of the length-to-diameter is significant when volumetric hoop strain is taken into account. The effect of the rigidity index has no significance in comparison with the effects of the length-to-diameter ratio in both cases.

Shear Strength

Shear strength is overestimated due to the effects of the length-to-diameter ratio, particularly when the ratio is small. The value derived from the volumetric strain derived from the central hoop strain is higher than the averaged volumetric strain derived from volumetric hoop strain. It can be also seen that the overestimation depends both on the rigidity index and on the strain range over which shear strain was measured. Therefore, the overestimation due to the length-to-diameter ratio is examined in two ways below.

The overestimation due to the length-to-diameter ratio seems to become constant in the analyses with high rigidity index (e.g. I_r = 250.500 or 1000) when the length-to-diameter ratio is more than 10, although there is a small drop when the length-to-diameter ratio is small (Figure 27). On the other hand, when the rigidity index is relatively small, the overestimation is almost linear with the D/L ratio. Focusing on the results of shear strength measured over the range 6% to 10% and 6% to 15%, it can be said that the measured values seem to become more constant at high D/L values, compared to the values measured over the range 2% to 5%. The constant value is between 1.2 and 1.35. (Fig 27). This trend is slightly present even in the case of a small rigidity index(e.g. I_r = 50 or 100) (Figure 28).

The details of the derived shear strength are examined below. First of all, the effects of the length-to-diameter ratio on the corrected measured shear strength are examined. Firstly, the results of the derived values over the strain 2% to 5% are given attention (Figure 27). In the volumetric strain derived from central hoop strain case, the overestimation is between 22% and 27% when the rigidity index is 1000 or 500 and the length-to-diameter ratio is less than 10. This means that when the rigidity index is sufficiently high, the overestimation is not influenced much by the rigidity index. In contrast, when the rigidity index is less than or equal to 200, the overestimation is almost linear to the D/L ratio and the overestimation is found to be larger as the length-to-diameter ratio is less. In the averaged volumetric strain derived from volumetric hoop strain case, the overestimation seems to become constant when the length-to-diameter ratio is more than 0.16, although the overestimation increases slightly when the rigidity index is less than or equal to 200. The value is between 17% and 20%. This means that the overestimation found when the L/D is less than or equal to 6 is affected by neither the length-to-diameter ratio nor the rigidity index. This means that when the pressuremeter, the length-to-diameter of which is equal to 6, is used, the overestimation may be about constant and the deviation due to the length-to-diameter ratio and the rigidity index is less than 3%.

The results of the derived values over the strain 6% to 10% are examined next (Figure 27). In the volumetric strain derived from central hoop strain case, it is more obvious in comparison with the previous case that the overestimation become

constant even when the rigidity index is 50. When the rigidity index is more than or equal to 100 and the length-to-diameter ratio is less than 10, the overestimation takes a value between 20% and 30%. The deviation due to the length-to-diameter for $I_r = 500$ or 1000 is less than 5%. In the averaged volumetric strain derived from volumetric hoop strain case, the overestimation seems much more constant when the rigidity index is more than or equal to 200. The value is between 20% and 24%. Even for small rigidity index case (i.e. I_r =100 or 50), the overestimation value seems become constant when the D/L value is more than 0.2.

The results of the derived values over the strain 6% to 15% are examined lastly (Figure 27). As found in the previous case, the overestimation in the volumetric strain derived from central hoop strain case become constant when the rigidity index is relatively high (I_r =200.500 or 1000). The value is between 23% and 29%. The overestimation found in the averaged volumetric strain derived from volumetric hoop strain seems to be on the same line when the rigidity index value is more than or equal to 200, especially when the rigidity index is 500 and 1000. For I_r =500 or 1000, the deviation is less than 3%.

In addition, the derived values are examined according to the strain range where the undrained shear strength is measured. In the volumetric hoop strain derived from central hoop strain case, when the strain range becomes higher, it seems that the all lines approach to the left and the shape of the line get similar to the shape of the line for $I_r = 1000$. This kind of phenomenon can also be seen in the volumetric case. This implies that when the strain takes higher range, the overestimation tends to become constant. In fact, this is not surprising if imaging from Figure 13 (right).

Then, the effects of the rigidity index on the derived shear strength are investigated. The derived values from the strain range over 2% to 5% are first examined (Figure 28). In the central strain case, for D/L ratio less than or equal to 0.125, the overestimation almost linearly increases with the logarithm of the rigidity index. However, on the other hand, when the D/L ratio is more than 0.125, the overestimation decreases when the rigidity index is high. This means that when using a short pressuremeter, the length-to-diameter of which is less than 8 and I_r is more than 500, the overestimation may be small in comparison with the other lower I_r

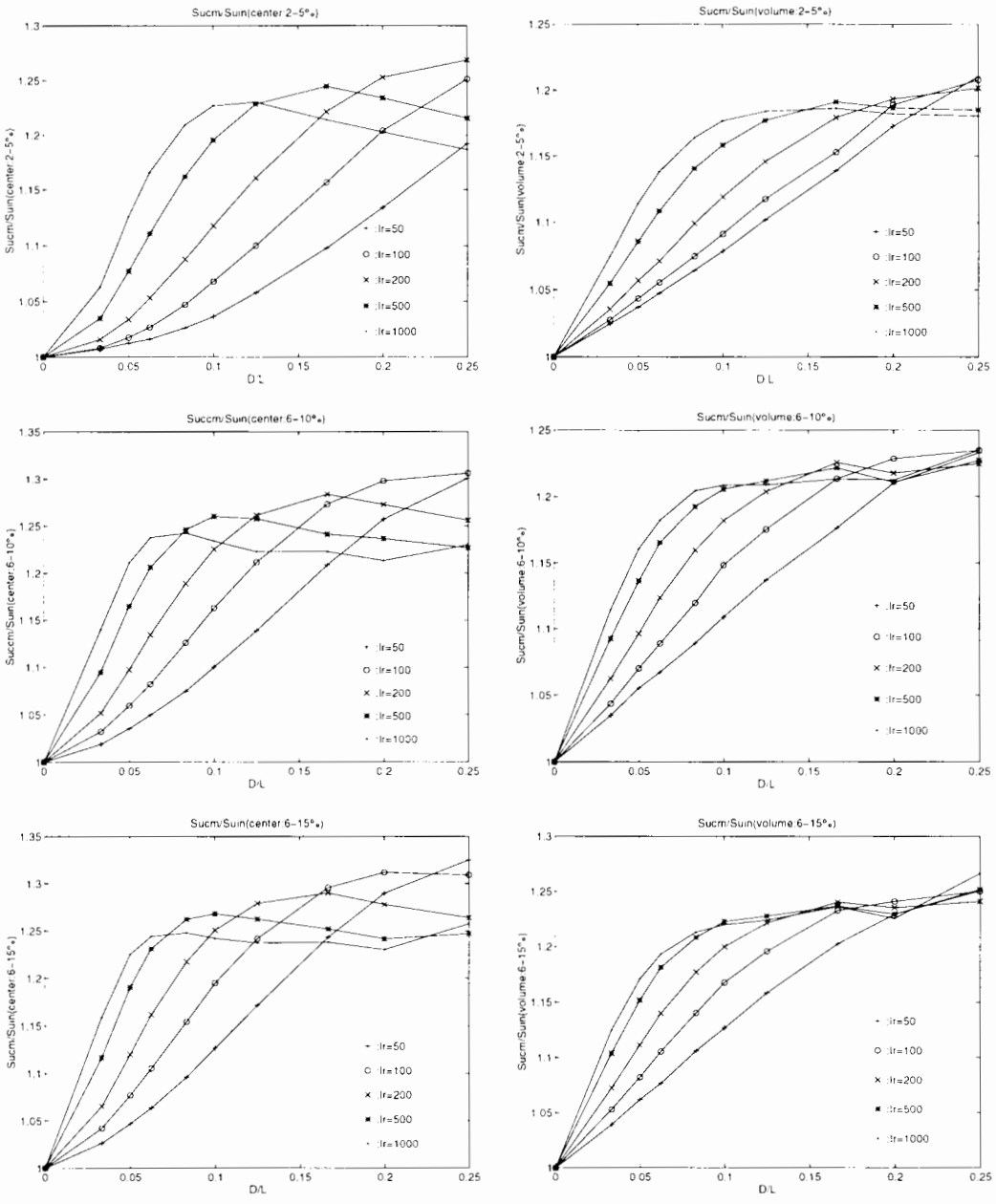


Figure 27: The effects of length to diameter ratio on shear modulus

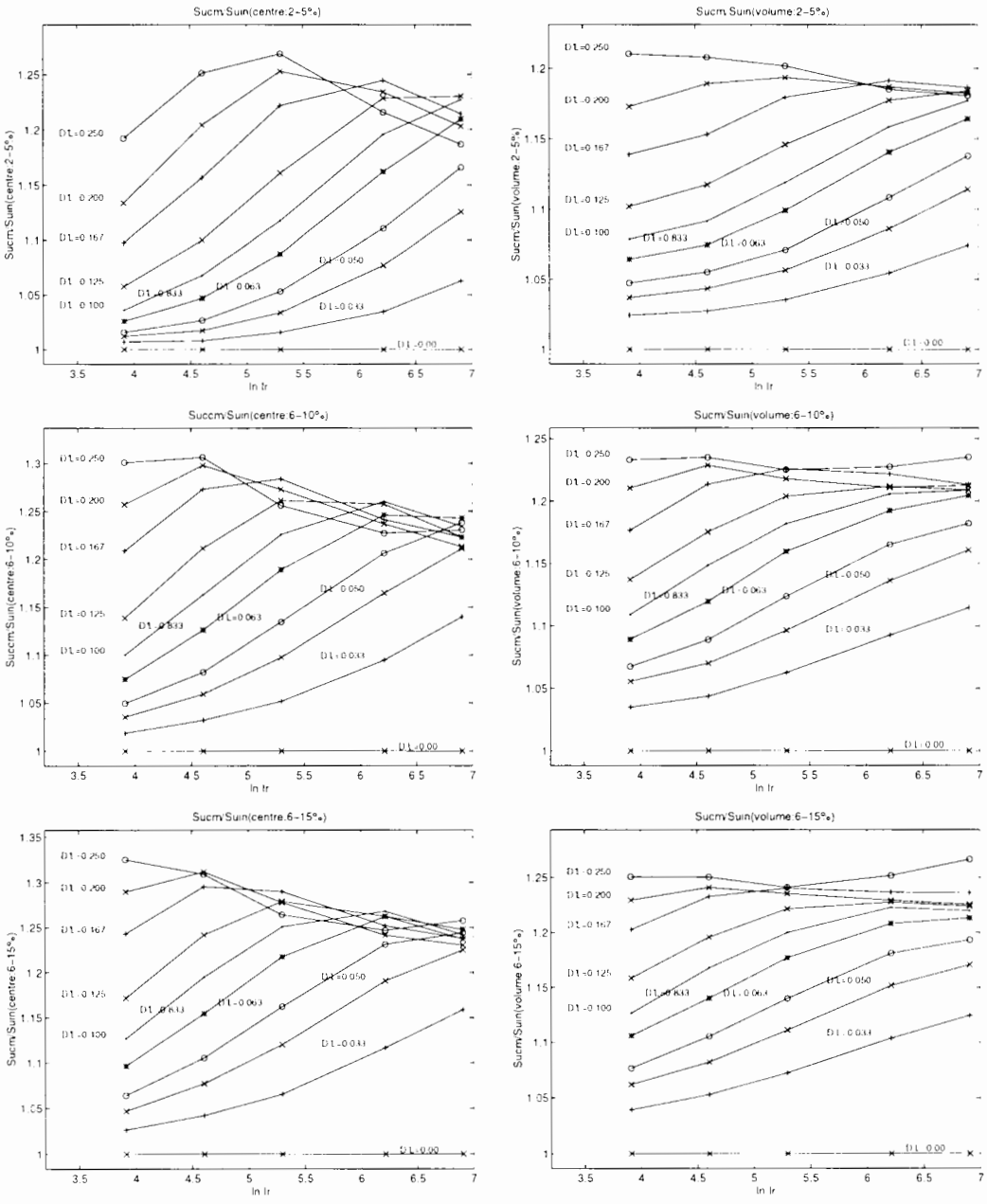


Figure 28: Effects of rigidity index on shear modulus

cases. In the averaged volumetric strain derived from volumetric hoop strain case, the rigidity index does not have a significant effect on the shear strength when the D/L ratio is more than 0.2, since the deviation due to the rigidity index is less than 5% in each case. Each line is flatter than the line found when the volumetric strain derived from central hoop strain is taken into account. This means that the effect of the rigidity index in the volumetric strain case is slightly less than in the volumetric strain derived from central hoop strain case.

The derived values from the strain range over 6% to 10% are examined next. In the volumetric strain derived from central hoop strain case, as found in Figure 27, the overestimation becomes constant when the D/L ratio is more than or equal to 0.125 and the rigidity index is relatively high. This means that when the length-to-diameter ratio is more than or equal to 8, the effect of the rigidity index on the shear strength has slightly less significance. When the D/L ratio is higher than 0.125, the effect of the rigidity index has significance. In the averaged volumetric strain derived from the volumetric hoop strain case, each line tends to be flatter comparing with the line in the volumetric strain derived from central hoop strain case as well.

The derived values from the strain over 6% to 15% are examined here. In the volumetric strain derived from central hoop strain case, it is found that the overestimation is almost constant with the maximum deviation of less than 9% when the length-to-diameter ratio is more than or equal to 6. The overestimation found in the shorter pressuremeter seems to decrease slightly when the rigidity index is higher. When the averaged volumetric strain derived from volumetric hoop strain is taken into account, the overestimation seems more constant when a short pressuremeter is used (D/L =4.5 or 6).

Finally, the derived values are examined according to which strain range is used. When the high strain range is taken into account, it can be seen that the lines tend to be on the same line both in the volumetric strain derived from the volumetric hoop strain case and the averaged volumetric strain derived from volumetric hoop strain case, as found in the Figure 27.

For the averaged volumetric strain derived from volumetric hoop strain case, it can be concluded that the effects of the length-to-diameter on the shear strength is

high when the rigidity index is small. On the other hand, the effect of the rigidity index on the shear strength is small when the length-to-diameter ratio is small. This means that it is necessary to take both effects into consideration in order to know the shear strength when the length-to-diameter ratio is high and and the rigidity index is small. However, the overestimation seems constant (15% to 25%) when the rigidity index is high and the length-to-diameter ratio is small. For the volumetric strain derived from central hoop strain case, the same conclusion can be derived, but the deviation is bigger than that found in the averaged volumetric strain derived from the volumetric strain.

2.2 Analysis in sand

2.2.1 Introduction

In this section, the analyses of the self boring pressuremeter in sand with the program, OXFEM 1.45, is given. A Matsuoka material with various shear moduli and friction angle is used. The mesh used in the analysis is the same as the medium mesh used in the previous section, since it is found that the medium mesh is sufficiently big to analyse this pressuremeter problem. In addition, equation 71 is used to specify the outer layer to model a horizontally infinite ground, although the Poisson's ratio is different for the sand from the clay. In each study, initial stress state is set to to be 1.0 horizontally (σ_{h0}) and vertically (σ_{v0}), which means that $K_0(=\frac{\sigma_{h0}}{\sigma_{v0}})$ is equal to 1.0, and all stresses were normalized with respect to σ_{h0}. For the numerical study, all analyses were carried out with $K_0 = 1.0$, since this allows direct comparison with available theoretical solutions e.g. Yu(1990). There is no implication that $K_0 = 1.0$ is in fact a typical value for sand. The pressure increment of $0.0001\sigma_{h0}$ was chosen to keep the analysis as stable as possible.

Various stiffness index values ($I_s = G/\sigma_{h0} = 50,100,200,500$ or 1000) are used and the Poisson's ratio is set to be 0.2 (which is a commonly used figure for sand) in all of the studies. The stiffness index is defined as ratio of the shear modulus to the initial horizontal stress, (G/σ_{h0}). The shear modulus of a correcting layer (G^*) was chosen according to the equation, $G^*/G = 0.6$. The critical state friction angle for plane strain (ϕ_{cr}) is assumed to 33^o in each case. In order to determine

the angle of dilation, Rowe's stress-dilatancy equation is applied:

$$\frac{1+\sin\phi_{ps}}{1-\sin\phi_{ps}} = \frac{1+\sin\phi_{cr}}{1-\sin\phi_{cr}}\frac{1+\sin\psi_{ps}}{1-\sin\psi_{ps}} \tag{73}$$

where ϕ_{ps} and ψ_{ps} are the angle of friction for plane strain and the angle of dilation for plane strain respectively.

Because the Matsuoka model is based on a triaxial friction angle (ϕ_{tc}) and dilation angle (ψ_{tc}), it is necessary to derive the relationship between ϕ_{tc}, ψ_{tc},ϕ_{ps} and ψ_{ps}.

Firstly, the Matsuoka yield function (f) may be written as a function of the principal stresses ($\sigma_1 \geq \sigma_2 \geq \sigma_3$):

$$f(\sigma) = I_1 I_2 - I_3\zeta (= 0) \tag{74}$$

where

$$I_1 = \sigma_1 + \sigma_2 + \sigma_3$$

$$I_2 = \sigma_1\sigma_2 + \sigma_2\sigma_3 + \sigma_3\sigma_1$$

$$I_3 = \sigma_1\sigma_2\sigma_3$$

$$\zeta = \tan^2\phi_{tc}$$

Secondly, the definition of the friction angle for plane strain may expressed as:

$$\sin\phi_{ps} = \frac{\sigma_1 - \sigma_3}{\sigma_1 + \sigma_3} \tag{75}$$

Thirdly, the plastic potential is defined by

$$g(\sigma) = I_1^* I_2^* - I_3^*\zeta^* (= 0) \tag{76}$$

where

$$I_1^* = \sigma_1^* + \sigma_2^* + \sigma_3^*$$

$$I_2^* = \sigma_1^*\sigma_2^* + \sigma_2^*\sigma_3^* + \sigma_3^*\sigma_1^*$$

$$I_3^* = \sigma_1^*\sigma_2^*\sigma_3^*$$

$$\zeta^* = \tan^2\psi_{tc}$$

$$\sigma_{ij}^* = \sigma_{ij} + k\delta_{ij}$$

The parameter k is calculated on the grounds that the plastic potential and the yield function must coincide at the current stress state.

Fourthly, the intermediate plastic strain rate is zero for plane strain. This is expressed by:

$$\frac{\partial g}{\partial \sigma_2} = 0 \tag{77}$$

Finally, the angle of dilation for plane strain is defined as below:

$$\sin \upsilon_{ps} = -\frac{\dot{\epsilon}_1 + \dot{\epsilon}_3}{\dot{\epsilon}_1 - \dot{\epsilon}_3} \tag{78}$$

and the major plastic strain (ϵ_1) and the minor plastic strain (ϵ_3) are derived from the flow rule:

$$\dot{\epsilon}_{ij} = \lambda \frac{\partial g}{\partial \sigma_{ij}} \tag{79}$$

where λ is an undetermined multiplier.

Using the equation (76) and (77) to eliminate υ_{tc}, the following equation is obtained:

$$(\sigma_2^{*2} - \sigma_1^* \sigma_3^*)(\sigma_1^* + \sigma_3^*) = 0 \tag{80}$$

When $\sigma_1^* + \sigma_3^*$ is equal to zero, fact that $\zeta^* = 1$ or $\sin \upsilon_{ps} = 0$, therefore equation (80) is in all practical cases equivalent to:

$$\sigma_2^{*2} - \sigma_1^* \sigma_3^* = 0 \tag{81}$$

Combining equations (76), (79) and (81) produces:

$$\frac{\dot{\epsilon}_1}{\dot{\epsilon}_3} = -\frac{\sigma_3^*}{\sigma_1^*} = -\frac{\sigma_3 + k}{\sigma_1 + k} \tag{82}$$

Using equations (75) and (82) may derive the values (σ_1/σ_3, σ_1^*/σ_3^*) (σ_1/σ_3, k/σ_3) from (φ_{ps}, υ_{ps}), except the case that υ_{ps} is equal to be zero. In addition to this, the value, σ_2/σ_3, is obtained from the equation (81). Since ζ and ζ^* can be obtained from the values, (σ_1/σ_3, σ_1^*/σ_3^*, σ_2/σ_3) by using the equations (74) and (76), φ_{tc} and υ_{tc} are determined from φ_{ps} and υ_{ps}

When υ_{ps} is equal to zero, σ_2 may be shown to be:

$$\sigma_2 = \frac{1}{2}(\sigma_1 + \sigma_3) \tag{83}$$

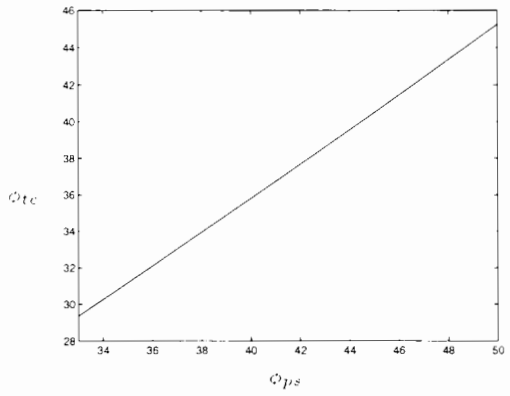


Figure 29: The relationship between ϕ_{ps} and ϕ_{tc}

ϕ_{psin}	ψ_{psin}	ϕ_{tsin}	ψ_{tsin}
33.00	0.00	29.35	0.00
38.00	6.13	33.94	5.31
43.00	12.62	38.60	10.95
48.00	19.48	43.34	16.95

Table 8: Input values for analysis of self-boring pressuremeter in sand

and using this equation and the equations (74) to (78), the relationship between the angle of friction for plane strain and for triaxial strain can be expressed by:

$$\tan^2 \phi_{tc} = \frac{3}{4} \tan^2 \phi_{ps}$$

and the angle of dilation for triaxial strain is zero.

The resulting relationship between ϕ_{ps} and ϕ_{tc} and between ϕ_{ps} and ψ_{tc} are presented in Figure 29, which is derived using the Rowe's equation (73).

In the analysis, four input plane strain frictional angle values ($\phi_{psin} = 48^o, 43^o, 38^o$ or 33^o) are chosen and other values (ϕ_{tsin}, ψ_{tsin}) are determined in the way described above. All of the input values can be seen in Table 8

2.2.2 Procedure of interpretation

Following the theory by Hughes et al. (1977), the friction angle of sand (ϕ) can be obtained from the slope of a straight line (s) from a plot of pressure against strain

on double logarithmic axes when the critical friction angle(ϕ_{cr}) is known:

$$\sin\phi = \frac{s}{1 + (s-1)\sin\phi_{cr}} \tag{84}$$

The apparent measured value of slope is obtained over the strain (ϵ), $1\% - 5\%$. Then, the measured value of friction(ϕ_m) is obtained by substituting measured slope value (s_m) and critical friction angle ($\phi_{cr} = 33^o$) into equation 84.

In engineering practice, the interpretation method by Hughes et al. is commonly used, although it is possible to obtain the exact small strain solution (Yu, 1990). In Hughes et al.'s method, it is assumed in the theory that the elastic deformation in plastic zone is small and negligible in comparison with the plastic strain component. The theoretical value of the slope for Hughes et al's method is defined as s_{ta} and that for Yu's method is defined as s_{ex}, which should be very close to the slope value obtained from the finite element analysis for an infinitely long case. ϕ_{ta} and ϕ_{ex} are obtained from equation 84 with the values, s_{ta} and s_{ex} respectively.

There are two ways to do correction of the measured values: one of them is against s_{ta} and the other is against s_{ex}. In this thesis, the later correction is chosen, because the corrected measured value should be a value which is thought to be found in in-situ condition. s_{ta} and ϕ_{ta} are used later to examine the effects of elastic deformation in plastic region.

Assuming that the possible numerical errors due to the non-linear algorithm in the measured slope for an infinitely long case will be of the same proportion in each analysis with the same input values , the measured slope (s_m) is calibrated by being divided by the ratio of the measured slope(s_m^∞) to the exact solution (s_{ex}). Defining this corrected value as s_{cm}, the correction procedure is expressed as following equations:

$$s_{cm} = s_m \frac{s_{ex}}{s_m^\infty} \tag{85}$$

From this corrected measured slope(s_{cm}), each corrected friction angle is calculated, following equation 84.

Indeed, it is possible to do this kind of correction by comparing measured friction angle in an infinitely long case (ϕ_m^∞) with input friction angle value (ϕ_{in}).

However, this calibration is slightly indirect, therefore, the calibration procedure described above is applied in this analysis.

The whole interpretation procedure is shown in Fig 30.

2.2.3 Numerical results

A total of 147 finite element analyses were completed, most of the all possible combinations of 8 values of L/D, 5 values of I_s and $\phi_{psin} = 33^o, 38^o, 43^o, 48^o$ were analysed.

All results are summarized in Table 9 to 16. Table 9 to 12 show the measured and corrected measured values of the loading slope. Table 13 to 16 show the ratio of the corrected measured value to the exact solution value.

As it is difficult to do the tests with higher value ϕ_{psin} and I_s, some of the tests ($\phi_{psin} = 38^o, I_s = 1000, L/D = 5, 6, 8, 10$, $\phi_{psin} = 43^o, I_s = 1000, L/D = 5, 6, 8, 10, 12$ and $\phi_{psin} = 48^o, I_s = 1000, L/D = 5, 6, 8, 10$) were not continued until the cavity strain reached 5 %. Therefore, all these results are eliminated in Table 9-16. Figure 31 shows the typical set of results of numerical simulations of the self-boring pressuremeter in sand for $I_s = 500$. A good agreement is found between the theoretical pressuremeter expansion curve using Yu's method and resulting pressuremeter expansion curve for an infinitely long case, with the maximum deviation of less than 1 % in the derived slope value.

Figure 32 shows the distribution of σ_r. It is found that only the area along the pressuremeter is compressed. Figure 33 shows distribution of $\tau_{r\theta}$. The relevant plots for the bottom left-hand corner of the large mesh (Figure 11) are shown in Figure 32 and 33 .

It is found that the area near the end of the pressuremeter is partly sheared, which cannot happen for an infinitely long case.

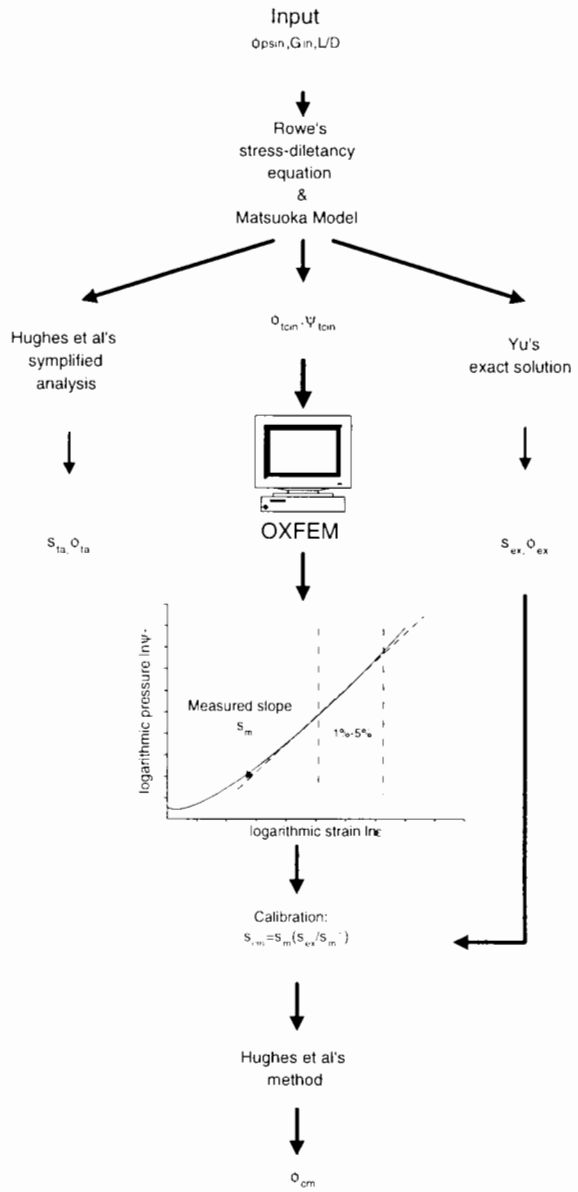


Figure 30: Procedure of interpretation for self-boring pressuremeter in sand

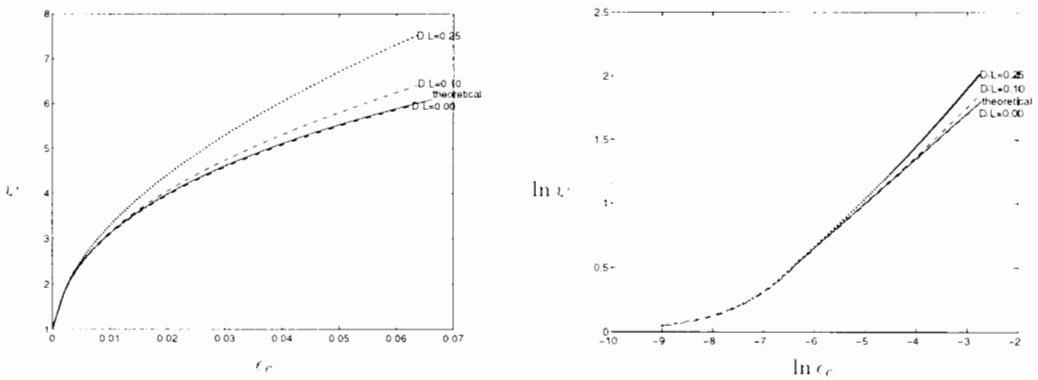


Figure 31: A comparison between theoretical and numerical pressuremeter curves ($I_s = 100$)

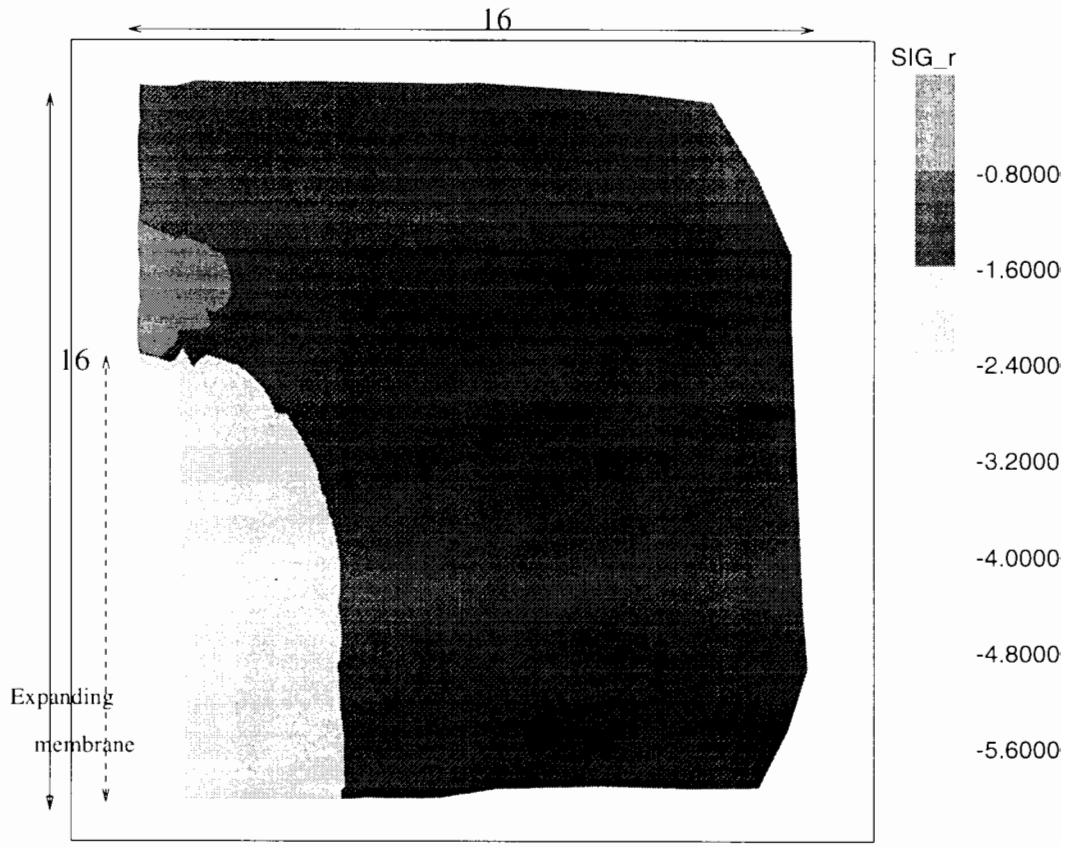


Figure 32: Distribution of σ_r for $\varphi_{psin} = 33^o, I_s = 500, L/D = 10.$ (contours at intervals of $0.8\sigma_{h0}$)

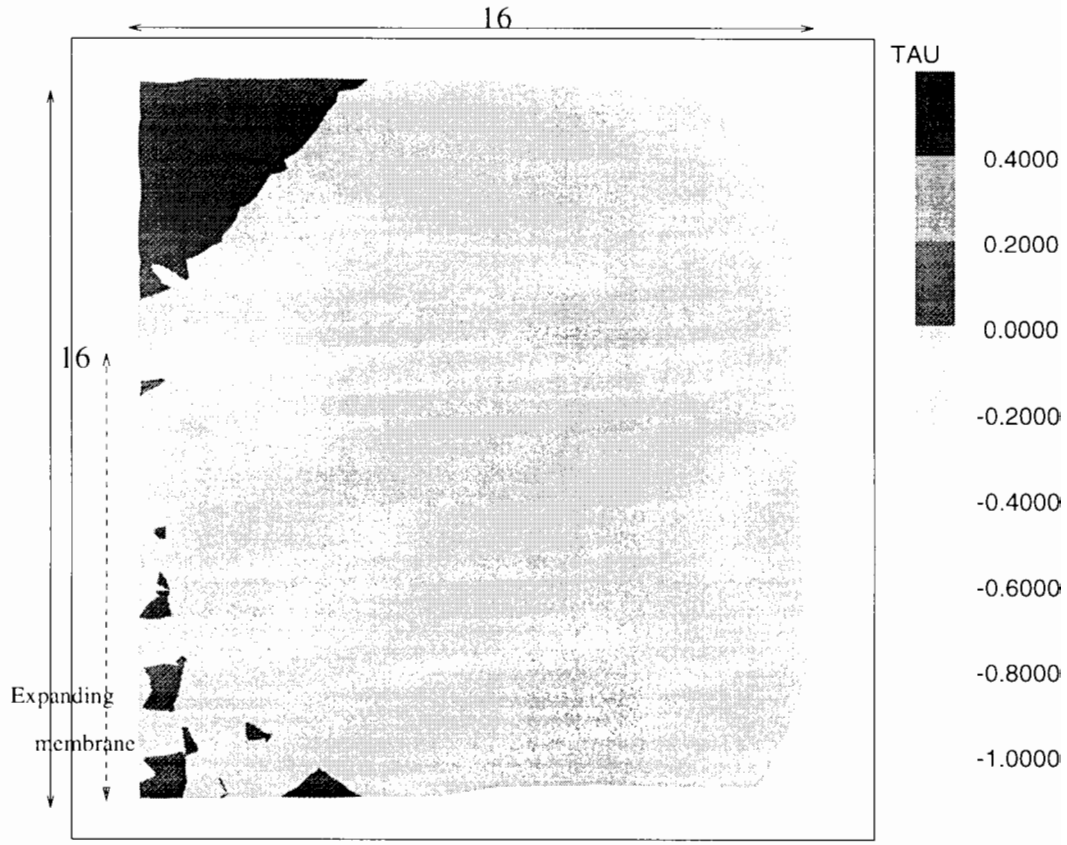


Figure 33: Distribution of $\tau_{r\theta}$ for $\phi_{psin} = 33^o, I_s = 500, L/D = 10.$ (contours at intervals of $0.2\sigma_{h0}$)

input values					central		volumetric	
φ_{psin}	I_s	L/D	s_{ta}	s_{ex}	s_m	s_{cm}	s_m	s_{cm}
33.0	50	5	0.329	0.296	0.320	0.322	0.329	0.332
33.0	50	6	0.329	0.296	0.312	0.314	0.322	0.325
33.0	50	8	0.329	0.296	0.305	0.307	0.314	0.317
33.0	50	10	0.329	0.296	0.302	0.304	0.310	0.313
33.0	50	12	0.329	0.296	0.300	0.302	0.307	0.310
33.0	50	16	0.329	0.296	0.298	0.300	0.303	0.306
33.0	50	20	0.329	0.296	0.297	0.299	0.301	0.305
33.0	50	∞	0.329	0.296	0.295	0.296	0.293	0.296
33.0	100	5	0.329	0.302	0.340	0.344	0.346	0.351
33.0	100	6	0.329	0.302	0.330	0.334	0.338	0.343
33.0	100	8	0.329	0.302	0.317	0.321	0.327	0.331
33.0	100	10	0.329	0.302	0.311	0.315	0.321	0.325
33.0	100	12	0.329	0.302	0.307	0.311	0.316	0.321
33.0	100	16	0.329	0.302	0.304	0.307	0.311	0.315
33.0	100	20	0.329	0.302	0.302	0.306	0.308	0.312
33.0	100	∞	0.329	0.302	0.298	0.302	0.298	0.302
33.0	200	5	0.329	0.310	0.368	0.373	0.369	0.374
33.0	200	6	0.329	0.310	0.355	0.361	0.360	0.365
33.0	200	8	0.329	0.310	0.339	0.344	0.347	0.352
33.0	200	10	0.329	0.310	0.329	0.334	0.338	0.343
33.0	200	12	0.329	0.310	0.322	0.327	0.332	0.337
33.0	200	16	0.329	0.310	0.315	0.320	0.325	0.330
33.0	200	20	0.329	0.310	0.312	0.316	0.321	0.325
33.0	200	∞	0.329	0.310	0.306	0.310	0.306	0.310
33.0	500	5	0.329	0.320	0.402	0.407	0.395	0.399
33.0	500	6	0.329	0.320	0.392	0.397	0.388	0.392
33.0	500	8	0.329	0.320	0.375	0.379	0.375	0.379
33.0	500	10	0.329	0.320	0.361	0.365	0.365	0.369
33.0	500	12	0.329	0.320	0.351	0.355	0.358	0.361
33.0	500	16	0.329	0.320	0.338	0.342	0.347	0.351
33.0	500	20	0.329	0.320	0.331	0.334	0.340	0.344
33.0	500	∞	0.329	0.320	0.317	0.320	0.317	0.320
33.0	1000	5	0.329	0.326	0.419	0.422	0.409	0.412
33.0	1000	6	0.329	0.326	0.413	0.417	0.405	0.408
33.0	1000	8	0.329	0.326	0.400	0.403	0.395	0.398
33.0	1000	10	0.329	0.326	0.387	0.390	0.385	0.388
33.0	1000	12	0.329	0.326	0.376	0.379	0.377	0.380
33.0	1000	16	0.329	0.326	0.360	0.363	0.365	0.367
33.0	1000	20	0.329	0.326	0.349	0.352	0.356	0.359
33.0	1000	∞	0.329	0.326	0.323	0.326	0.324	0.326

Table 9: Results of measured values of the slope from finite element analysis of self-boring pressuremeter in sand for $\varphi_{psin} = 33^o$ (see text for definitions of variables)

input values					central		volumetric	
ϕ_{psin}	I_s	L/D	s_{ta}	s_{cx}	s_m	s_{cm}	s_m	s_{cm}
38.0	50	5	0.391	0.340	0.364	0.365	0.377	0.379
38.0	50	6	0.391	0.340	0.357	0.358	0.370	0.371
38.0	50	8	0.391	0.340	0.349	0.351	0.361	0.363
38.0	50	10	0.391	0.340	0.346	0.347	0.356	0.358
38.0	50	12	0.391	0.340	0.344	0.345	0.353	0.354
38.0	50	16	0.391	0.340	0.342	0.343	0.349	0.350
38.0	50	20	0.391	0.340	0.341	0.342	0.347	0.348
38.0	50	∞	0.391	0.340	0.339	0.340	0.339	0.340
38.0	100	5	0.391	0.349	0.390	0.394	0.400	0.404
38.0	100	6	0.391	0.349	0.380	0.383	0.391	0.395
38.0	100	8	0.391	0.349	0.366	0.370	0.379	0.382
38.0	100	10	0.391	0.349	0.359	0.363	0.371	0.375
38.0	100	12	0.391	0.349	0.355	0.359	0.367	0.370
38.0	100	16	0.391	0.349	0.351	0.355	0.361	0.364
38.0	100	20	0.391	0.349	0.349	0.353	0.358	0.361
38.0	100	∞	0.391	0.349	0.346	0.349	0.346	0.349
38.0	200	5	0.391	0.361	0.427	0.432	0.430	0.435
38.0	200	6	0.391	0.361	0.414	0.419	0.420	0.424
38.0	200	8	0.391	0.361	0.394	0.399	0.405	0.409
38.0	200	10	0.391	0.361	0.383	0.387	0.395	0.399
38.0	200	12	0.391	0.361	0.375	0.380	0.388	0.392
38.0	200	16	0.391	0.361	0.367	0.372	0.380	0.383
38.0	200	20	0.391	0.361	0.363	0.368	0.375	0.378
38.0	200	∞	0.391	0.361	0.357	0.361	0.358	0.361
38.0	500	5	0.391	0.376	0.473	0.477	0.467	0.470
38.0	500	6	0.391	0.376	0.461	0.465	0.458	0.461
38.0	500	8	0.391	0.376	0.441	0.444	0.443	0.445
38.0	500	10	0.391	0.376	0.425	0.428	0.431	0.433
38.0	500	12	0.391	0.376	0.413	0.416	0.422	0.424
38.0	500	16	0.391	0.376	0.398	0.401	0.409	0.411
38.0	500	20	0.391	0.376	0.389	0.392	0.401	0.403
38.0	500	∞	0.391	0.376	0.373	0.376	0.374	0.376
38.0	1000	12	0.391	0.385	0.443	0.445	0.444	0.445
38.0	1000	16	0.391	0.385	0.427	0.428	0.433	0.434
38.0	1000	20	0.391	0.385	0.413	0.415	0.423	0.423
38.0	1000	∞	0.391	0.385	0.383	0.385	0.384	0.385

Table 10: Results of measured values of the slope from finite element analysis of self-boring pressuremeter in sand for $\phi_{psin} = 38^o$ (see text for definitions of variables)

input values					central		volumetric	
ϕ_{psin}	I_s	L/D	s_{ta}	s_{ex}	s_m	s_{cm}	s_m	s_{cm}
43.0	50	5	0.457	0.379	0.405	0.405	0.420	0.420
43.0	50	6	0.457	0.379	0.398	0.398	0.413	0.413
43.0	50	8	0.457	0.379	0.390	0.390	0.403	0.403
43.0	50	10	0.457	0.379	0.386	0.386	0.398	0.398
43.0	50	12	0.457	0.379	0.384	0.384	0.395	0.394
43.0	50	16	0.457	0.379	0.382	0.382	0.390	0.390
43.0	50	20	0.457	0.379	0.381	0.381	0.388	0.388
43.0	50	∞	0.457	0.379	0.380	0.379	0.380	0.379
43.0	100	5	0.457	0.393	0.438	0.441	0.450	0.452
43.0	100	6	0.457	0.393	0.426	0.428	0.440	0.442
43.0	100	8	0.457	0.393	0.412	0.414	0.427	0.429
43.0	100	10	0.457	0.393	0.404	0.407	0.419	0.421
43.0	100	12	0.457	0.393	0.400	0.403	0.414	0.415
43.0	100	16	0.457	0.393	0.396	0.398	0.407	0.409
43.0	100	20	0.457	0.393	0.394	0.397	0.404	0.406
43.0	100	∞	0.457	0.393	0.391	0.393	0.392	0.393
43.0	200	5	0.457	0.410	0.481	0.486	0.488	0.491
43.0	200	6	0.457	0.410	0.466	0.470	0.476	0.479
43.0	200	8	0.457	0.410	0.446	0.450	0.459	0.462
43.0	200	10	0.457	0.410	0.433	0.437	0.448	0.451
43.0	200	12	0.457	0.410	0.426	0.429	0.441	0.443
43.0	200	16	0.457	0.410	0.417	0.421	0.431	0.434
43.0	200	20	0.457	0.410	0.413	0.417	0.426	0.429
43.0	200	∞	0.457	0.410	0.406	0.410	0.407	0.410
43.0	500	5	0.457	0.430	0.540	0.543	0.535	0.537
43.0	500	6	0.457	0.430	0.526	0.529	0.525	0.526
43.0	500	8	0.457	0.430	0.503	0.506	0.507	0.508
43.0	500	10	0.457	0.430	0.485	0.488	0.493	0.494
43.0	500	12	0.457	0.430	0.472	0.475	0.483	0.484
43.0	500	16	0.457	0.430	0.455	0.458	0.469	0.470
43.0	500	20	0.457	0.430	0.445	0.448	0.460	0.461
43.0	500	∞	0.457	0.430	0.427	0.430	0.429	0.430
43.0	1000	16	0.457	0.442	0.491	0.492	0.500	0.499
43.0	1000	20	0.457	0.442	0.476	0.477	0.488	0.487
43.0	1000	∞	0.457	0.442	0.441	0.442	0.443	0.442

Table 11: Results of measured values of the slope from finite element analysis of self-boring pressuremeter in sand for $\phi_{psin} = 43^o$ (see text for definitions of variables)

input values					central		volumetric	
ϕ_{psin}	I_s	L/D	s_{ta}	s_{ex}	s_m	s_{cm}	s_m	s_{cm}
48.0	50	5	0.526	0.414	0.440	0.438	0.457	0.455
48.0	50	6	0.526	0.414	0.433	0.431	0.449	0.448
48.0	50	8	0.526	0.414	0.425	0.424	0.440	0.439
48.0	50	10	0.526	0.414	0.422	0.420	0.434	0.433
48.0	50	12	0.526	0.414	0.420	0.418	0.431	0.430
48.0	50	16	0.526	0.414	0.418	0.416	0.427	0.426
48.0	50	20	0.526	0.414	0.417	0.416	0.425	0.423
48.0	50	∞	0.526	0.414	0.416	0.414	0.416	0.414
48.0	100	5	0.526	0.433	0.479	0.480	0.495	0.495
48.0	100	6	0.526	0.433	0.467	0.468	0.484	0.484
48.0	100	8	0.526	0.433	0.453	0.454	0.470	0.470
48.0	100	10	0.526	0.433	0.446	0.447	0.461	0.462
48.0	100	12	0.526	0.433	0.441	0.442	0.456	0.456
48.0	100	16	0.526	0.433	0.437	0.438	0.450	0.450
48.0	100	20	0.526	0.433	0.435	0.436	0.446	0.446
48.0	100	∞	0.526	0.433	0.432	0.433	0.433	0.433
48.0	200	5	0.526	0.454	0.530	0.533	0.540	0.541
48.0	200	6	0.526	0.454	0.514	0.517	0.527	0.528
48.0	200	8	0.526	0.454	0.493	0.496	0.508	0.510
48.0	200	10	0.526	0.454	0.480	0.482	0.497	0.498
48.0	200	12	0.526	0.454	0.472	0.474	0.489	0.490
48.0	200	16	0.526	0.454	0.463	0.465	0.479	0.480
48.0	200	20	0.526	0.454	0.459	0.461	0.473	0.474
48.0	200	∞	0.526	0.454	0.452	0.454	0.453	0.454
48.0	500	5	0.526	0.480	0.599	0.602	0.597	0.597
48.0	500	6	0.526	0.480	0.584	0.587	0.584	0.585
48.0	500	8	0.526	0.480	0.559	0.561	0.565	0.565
48.0	500	10	0.526	0.480	0.540	0.543	0.550	0.550
48.0	500	12	0.526	0.480	0.526	0.528	0.539	0.540
48.0	500	16	0.526	0.480	0.508	0.511	0.524	0.524
48.0	500	20	0.526	0.480	0.498	0.500	0.514	0.514
48.0	500	∞	0.526	0.480	0.478	0.480	0.480	0.480
48.0	1000	12	0.526	0.496	0.571	0.572	0.573	0.572
48.0	1000	16	0.526	0.496	0.551	0.552	0.561	0.559
48.0	1000	20	0.526	0.496	0.535	0.536	0.548	0.547
48.0	1000	∞	0.526	0.496	0.496	0.496	0.498	0.496

Table 12: Results of measured values of the slope from finite element analysis of self-boring pressuremeter in sand for $\phi_{psin} = 48^o$ (see text for definitions of variables)

input values					central		volumetric	
ϕ_{psin}	I_s	L/D	$\frac{\varepsilon_{ta}}{\varepsilon_{ex}}$	$\frac{\phi_{ta}}{\phi_{ex}}$	$\frac{\varepsilon_{cm}}{\varepsilon_{ex}}$	$\frac{\phi_{cm}}{\phi_{ex}}$	$\frac{\varepsilon_{cm}}{\varepsilon_{ex}}$	$\frac{\phi_{cm}}{\phi_{ex}}$
33.0	50	5	1.110	1.087	1.086	1.069	1.121	1.096
33.0	50	6	1.110	1.087	1.061	1.049	1.098	1.078
33.0	50	8	1.110	1.087	1.036	1.029	1.071	1.057
33.0	50	10	1.110	1.087	1.024	1.019	1.056	1.045
33.0	50	12	1.110	1.087	1.018	1.014	1.046	1.037
33.0	50	16	1.110	1.087	1.011	1.009	1.034	1.027
33.0	50	20	1.110	1.087	1.008	1.006	1.027	1.022
33.0	50	∞	1.110	1.087	1.000	1.000	1.000	1.000
33.0	100	5	1.089	1.071	1.139	1.110	1.161	1.127
33.0	100	6	1.089	1.071	1.105	1.084	1.134	1.106
33.0	100	8	1.089	1.071	1.064	1.051	1.097	1.077
33.0	100	10	1.089	1.071	1.042	1.034	1.076	1.060
33.0	100	12	1.089	1.071	1.030	1.024	1.061	1.049
33.0	100	16	1.089	1.071	1.017	1.014	1.044	1.035
33.0	100	20	1.089	1.071	1.011	1.009	1.034	1.027
33.0	100	∞	1.089	1.071	1.000	1.000	1.000	1.000
33.0	200	5	1.060	1.048	1.203	1.158	1.205	1.160
33.0	200	6	1.060	1.048	1.162	1.127	1.176	1.138
33.0	200	8	1.060	1.048	1.109	1.086	1.134	1.106
33.0	200	10	1.060	1.048	1.076	1.060	1.105	1.083
33.0	200	12	1.060	1.048	1.054	1.043	1.086	1.068
33.0	200	16	1.060	1.048	1.031	1.025	1.063	1.050
33.0	200	20	1.060	1.048	1.020	1.016	1.048	1.038
33.0	200	∞	1.060	1.048	1.000	1.000	1.000	1.000
33.0	500	5	1.027	1.022	1.270	1.208	1.247	1.191
33.0	500	6	1.027	1.022	1.240	1.186	1.224	1.174
33.0	500	8	1.027	1.022	1.184	1.144	1.184	1.143
33.0	500	10	1.027	1.022	1.141	1.111	1.152	1.119
33.0	500	12	1.027	1.022	1.108	1.085	1.129	1.101
33.0	500	16	1.027	1.022	1.068	1.054	1.095	1.075
33.0	500	20	1.027	1.022	1.044	1.035	1.074	1.059
33.0	500	∞	1.027	1.022	1.000	1.000	1.000	1.000
33.0	1000	5	1.009	1.007	1.295	1.227	1.264	1.203
33.0	1000	6	1.009	1.007	1.278	1.214	1.251	1.194
33.0	1000	8	1.009	1.007	1.237	1.183	1.221	1.171
33.0	1000	10	1.009	1.007	1.197	1.153	1.190	1.148
33.0	1000	12	1.009	1.007	1.164	1.128	1.165	1.129
33.0	1000	16	1.009	1.007	1.112	1.088	1.127	1.099
33.0	1000	20	1.009	1.007	1.078	1.062	1.101	1.079
33.0	1000	∞	1.009	1.007	1.000	1.000	1.000	1.000

Table 13: A comparison of corrected measured values from finite element analysis of self-boring pressuremeter in sand for $\phi_{psin} = 33^o$ (see text for definitions of variables)

input values					central		volumetric	
ϕ_{psin}	I_s	L/D	$\frac{\varepsilon_{ta}}{\varepsilon_{cx}}$	$\frac{\varphi_{ta}}{\varphi_{cx}}$	$\frac{\varepsilon_{cm}}{\varepsilon_{cx}}$	$\frac{\varphi_{cm}}{\varphi_{cx}}$	$\frac{\varepsilon_{cm}}{\varepsilon_{cx}}$	$\frac{\varphi_{cm}}{\varphi_{cx}}$
38.0	50	5	1.152	1.118	1.075	1.059	1.114	1.089
38.0	50	6	1.152	1.118	1.054	1.043	1.093	1.073
38.0	50	8	1.152	1.118	1.031	1.025	1.066	1.052
38.0	50	10	1.152	1.118	1.020	1.016	1.052	1.041
38.0	50	12	1.152	1.118	1.014	1.011	1.042	1.033
38.0	50	16	1.152	1.118	1.009	1.007	1.031	1.025
38.0	50	20	1.152	1.118	1.006	1.005	1.025	1.020
38.0	50	∞	1.152	1.118	1.000	1.000	1.000	1.000
38.0	100	5	1.121	1.094	1.128	1.100	1.157	1.122
38.0	100	6	1.121	1.094	1.097	1.076	1.130	1.101
38.0	100	8	1.121	1.094	1.059	1.046	1.094	1.074
38.0	100	10	1.121	1.094	1.038	1.030	1.073	1.057
38.0	100	12	1.121	1.094	1.027	1.021	1.059	1.046
38.0	100	16	1.121	1.094	1.015	1.012	1.043	1.034
38.0	100	20	1.121	1.094	1.010	1.008	1.033	1.026
38.0	100	∞	1.121	1.094	1.000	1.000	1.000	1.000
38.0	200	5	1.084	1.065	1.195	1.150	1.203	1.156
38.0	200	6	1.084	1.065	1.158	1.123	1.174	1.134
38.0	200	8	1.084	1.065	1.104	1.081	1.131	1.102
38.0	200	10	1.084	1.065	1.072	1.057	1.103	1.080
38.0	200	12	1.084	1.065	1.052	1.041	1.085	1.067
38.0	200	16	1.084	1.065	1.029	1.023	1.061	1.048
38.0	200	20	1.084	1.065	1.018	1.014	1.047	1.037
38.0	200	∞	1.084	1.065	1.000	1.000	1.000	1.000
38.0	500	5	1.042	1.033	1.270	1.206	1.250	1.191
38.0	500	6	1.042	1.033	1.237	1.181	1.226	1.173
38.0	500	8	1.042	1.033	1.182	1.140	1.184	1.142
38.0	500	10	1.042	1.033	1.139	1.108	1.152	1.118
38.0	500	12	1.042	1.033	1.107	1.083	1.128	1.099
38.0	500	16	1.042	1.033	1.067	1.052	1.094	1.074
38.0	500	20	1.042	1.033	1.043	1.034	1.073	1.057
38.0	500	∞	1.042	1.033	1.000	1.000	1.000	1.000
38.0	1000	12	1.018	1.014	1.157	1.121	1.156	1.120
38.0	1000	16	1.018	1.014	1.114	1.088	1.128	1.099
38.0	1000	20	1.018	1.014	1.079	1.062	1.101	1.078
38.0	1000	∞	1.018	1.014	1.000	1.000	1.000	1.000

Table 14: A comparison of corrected measured values from finite element analysis of self-boring pressuremeter in sand for $\phi_{psin} = 38^o$ (see text for definitions of variables)

input values					central		volumetric	
ϕ_{psin}	I_s	L/D	$\frac{\varepsilon_{ta}}{\varepsilon_{ex}}$	$\frac{\phi_{ta}}{\phi_{ex}}$	$\frac{\varepsilon_{cm}}{\varepsilon_{ex}}$	$\frac{\phi_{cm}}{\phi_{ex}}$	$\frac{\varepsilon_{cm}}{\varepsilon_{ex}}$	$\frac{\phi_{cm}}{\phi_{ex}}$
43.0	50	5	1.205	1.157	1.067	1.052	1.107	1.083
43.0	50	6	1.205	1.157	1.048	1.038	1.087	1.068
43.0	50	8	1.205	1.157	1.027	1.021	1.062	1.048
43.0	50	10	1.205	1.157	1.017	1.013	1.048	1.038
43.0	50	12	1.205	1.157	1.012	1.010	1.040	1.031
43.0	50	16	1.205	1.157	1.007	1.005	1.029	1.023
43.0	50	20	1.205	1.157	1.005	1.004	1.023	1.018
43.0	50	∞	1.205	1.157	1.000	1.000	1.000	1.000
43.0	100	5	1.163	1.125	1.120	1.093	1.150	1.116
43.0	100	6	1.163	1.125	1.088	1.068	1.124	1.096
43.0	100	8	1.163	1.125	1.053	1.042	1.090	1.070
43.0	100	10	1.163	1.125	1.034	1.027	1.070	1.055
43.0	100	12	1.163	1.125	1.024	1.019	1.056	1.044
43.0	100	16	1.163	1.125	1.013	1.010	1.041	1.032
43.0	100	20	1.163	1.125	1.009	1.007	1.032	1.025
43.0	100	∞	1.163	1.125	1.000	1.000	1.000	1.000
43.0	200	5	1.116	1.089	1.185	1.142	1.199	1.152
43.0	200	6	1.116	1.089	1.148	1.114	1.169	1.130
43.0	200	8	1.116	1.089	1.098	1.076	1.127	1.098
43.0	200	10	1.116	1.089	1.067	1.052	1.100	1.077
43.0	200	12	1.116	1.089	1.048	1.037	1.082	1.064
43.0	200	16	1.116	1.089	1.027	1.021	1.059	1.046
43.0	200	20	1.116	1.089	1.017	1.013	1.046	1.036
43.0	200	∞	1.116	1.089	1.000	1.000	1.000	1.000
43.0	500	5	1.064	1.050	1.264	1.201	1.249	1.190
43.0	500	6	1.064	1.050	1.232	1.177	1.224	1.171
43.0	500	8	1.064	1.050	1.177	1.136	1.182	1.140
43.0	500	10	1.064	1.050	1.136	1.104	1.150	1.116
43.0	500	12	1.064	1.050	1.105	1.081	1.126	1.097
43.0	500	16	1.064	1.050	1.065	1.050	1.094	1.073
43.0	500	20	1.064	1.050	1.042	1.033	1.073	1.056
43.0	500	∞	1.064	1.050	1.000	1.000	1.000	1.000
43.0	1000	16	1.035	1.027	1.114	1.088	1.129	1.099
43.0	1000	20	1.035	1.027	1.080	1.062	1.102	1.079
43.0	1000	∞	1.035	1.027	1.000	1.000	1.000	1.000

Table 15: A comparison of corrected measured values from finite element analysis of self-boring pressuremeter in sand for $\phi_{psin} = 43^o$ (see text for definitions of variables)

input values					central		volumetric	
ϕ_{psin}	I_s	L/D	$\frac{\varepsilon_{ta}}{\varepsilon_{ex}}$	$\frac{\varphi_{ta}}{\varphi_{ex}}$	$\frac{\varepsilon_{cm}}{\varepsilon_{ex}}$	$\frac{\varphi_{cm}}{\varphi_{ex}}$	$\frac{\varepsilon_{cm}}{\varepsilon_{ex}}$	$\frac{\varphi_{cm}}{\varphi_{ex}}$
48.0	50	5	1.269	1.205	1.058	1.045	1.099	1.077
48.0	50	6	1.269	1.205	1.041	1.032	1.081	1.063
48.0	50	8	1.269	1.205	1.023	1.018	1.059	1.046
48.0	50	10	1.269	1.205	1.014	1.011	1.045	1.035
48.0	50	12	1.269	1.205	1.010	1.008	1.037	1.029
48.0	50	16	1.269	1.205	1.006	1.004	1.027	1.021
48.0	50	20	1.269	1.205	1.004	1.003	1.022	1.017
48.0	50	∞	1.269	1.205	1.000	1.000	1.000	1.000
48.0	100	5	1.214	1.163	1.109	1.084	1.143	1.110
48.0	100	6	1.214	1.163	1.082	1.063	1.118	1.091
48.0	100	8	1.214	1.163	1.049	1.038	1.086	1.066
48.0	100	10	1.214	1.163	1.031	1.024	1.066	1.051
48.0	100	12	1.214	1.163	1.021	1.016	1.054	1.042
48.0	100	16	1.214	1.163	1.011	1.009	1.039	1.031
48.0	100	20	1.214	1.163	1.007	1.006	1.030	1.024
48.0	100	∞	1.214	1.163	1.000	1.000	1.000	1.000
48.0	200	5	1.157	1.120	1.172	1.132	1.190	1.146
48.0	200	6	1.157	1.120	1.137	1.106	1.162	1.124
48.0	200	8	1.157	1.120	1.091	1.070	1.122	1.094
48.0	200	10	1.157	1.120	1.061	1.048	1.096	1.074
48.0	200	12	1.157	1.120	1.044	1.034	1.078	1.061
48.0	200	16	1.157	1.120	1.024	1.019	1.056	1.043
48.0	200	20	1.157	1.120	1.015	1.011	1.044	1.034
48.0	200	∞	1.157	1.120	1.000	1.000	1.000	1.000
48.0	500	5	1.094	1.073	1.253	1.194	1.244	1.187
48.0	500	6	1.094	1.073	1.221	1.170	1.218	1.167
48.0	500	8	1.094	1.073	1.169	1.130	1.177	1.136
48.0	500	10	1.094	1.073	1.130	1.100	1.146	1.113
48.0	500	12	1.094	1.073	1.100	1.078	1.124	1.095
48.0	500	16	1.094	1.073	1.063	1.049	1.092	1.071
48.0	500	20	1.094	1.073	1.041	1.032	1.071	1.055
48.0	500	∞	1.094	1.073	1.000	1.000	1.000	1.000
48.0	1000	12	1.059	1.046	1.152	1.117	1.153	1.118
48.0	1000	16	1.059	1.046	1.111	1.086	1.127	1.098
48.0	1000	20	1.059	1.046	1.079	1.061	1.101	1.078
48.0	1000	∞	1.059	1.046	1.000	1.000	1.000	1.000

Table 16: A comparison of corrected measured values from finite element analysis of self-boring pressuremeter in sand for $\phi_{psin} = 48^o$ (see text for definitions of variables)

The effect of elastic deformation in plastic region is first investigated. This effect is independent from the length-to-diameter ratio, because the exact small strain solution by Yu is used in the correction.

Figure 34 compares the slope values obtained from Hughes et al's method and from Yu's method. It is found from Figure 34 that the slope from Hughes et al's simplified analysis is larger than that from Yu's exact analysis, which indicates that the Hughes et al's analysis tends to underestimate the derived loading slopes and friction angle. The difference between the slopes become small when the stiffness index (I_s) is larger. For instance, the maximum value of the ratio, s_{ta}/s_{ex}, when I_s is equal to 1000 is less than 6 % ($I_s = 1000, \phi_{psin} = 48^o$) and the minimum value of that when I_s is equal to 50 is over 11 % ($I_s = 50, \phi_{psin} = 33^o$). The maximum value in the analyses is 27%, which is found when $I_s = 50$ and $\phi_{psin} = 48$ (Figure 34). This is reasonable because the elastic deformation in the plastic area may be small when the stiffness index value (I_s) is high.

As for the friction angle, the same trend can be found (Figure 35). The maximum value of the ratio, ϕ_{ta}/ϕ_{ex}, when I_s is equal to 1000 is less than 5 % ($I_s = 1000, \phi_{psin} = 48^o$) and the minimum value of that when I_s is equal to 50 is over 8.7 % ($I_s = 50, \phi_{psin} = 33^o$). The maximum value in the analyses is 20.5%, which is found when $I_s = 50$ and $\phi_{psin} = 48^o$ (Figure 35).

It is also found that the input friction angle (ϕ_{psin}) has influence on these values. In the case of the slope value (Figure 34), when the stiffness index is relatively large (I_s =500 or 1000), the deviation of the slope due to the friction angle (ϕ_{psin}) is 10 %. On the other hand, when the stiffness index is relatively small (I_s = 50 or 100), the deviation is more than 12 %. Considering the fact that the maximum deviation due to the stiffness index when the friction angle (ϕ_{psin}) is 33^o is 10 % and the maximum deviation is 21 % when the input friction angle (ϕ_{psin}) is 48^o, it can be said that the influence of the input friction angle (ϕ_{psin}) is significant. In addition, this deviation gets larger when the friction angle (ϕ_{psin}) is larger.

In the case of the friction angle values (Figure 35), the maximum deviation when the friction angle (ϕ_{psin}) is 33^o is 8 % and the maximum deviation when the input friction angle (ϕ_{psin}) is 48^o is 15 %. The same phenomena as found in the slope values can be seen, but, the influence of the input friction angle (ϕ_{psin})

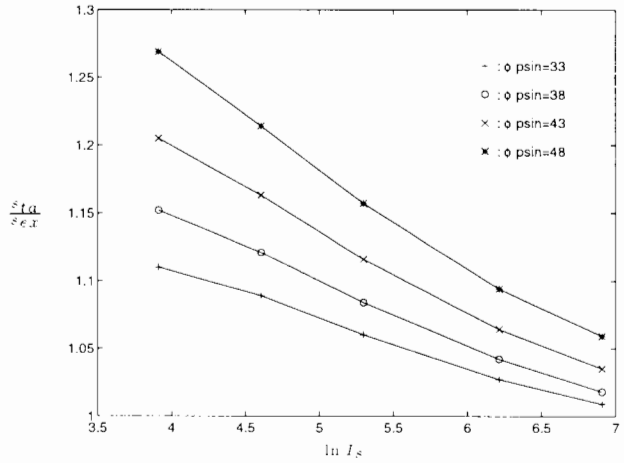


Figure 34: A comparison between s_{ta} and s_{ex}

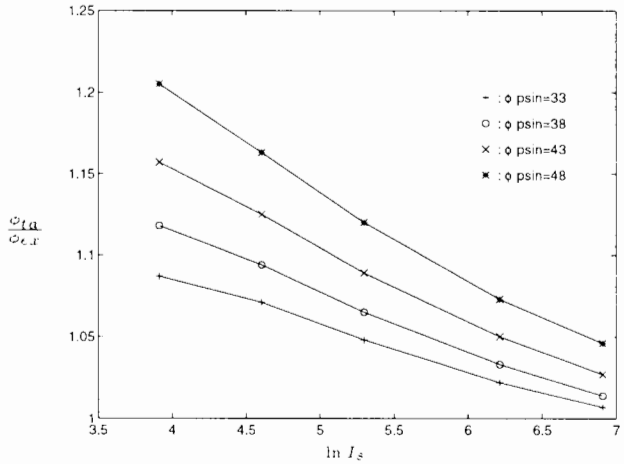


Figure 35: A comparison between o_{ta} and o_{ex}

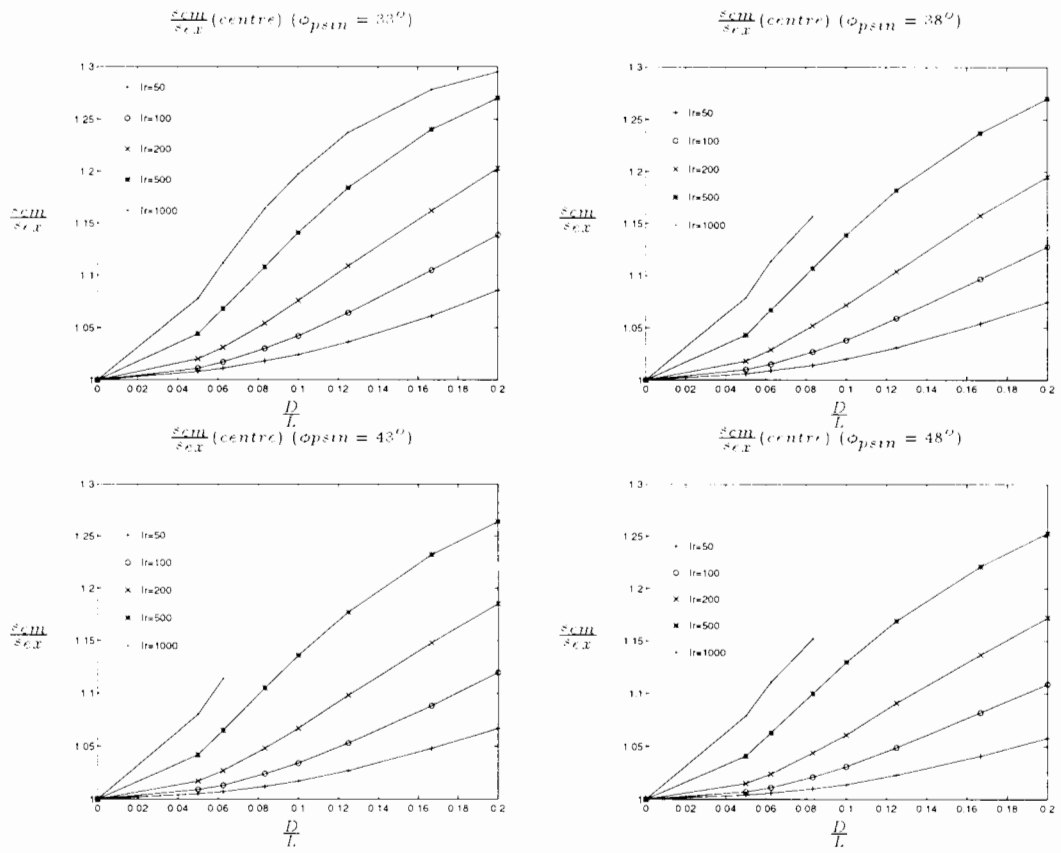


Figure 36: A comparison between s_m and s_{cx} using central hoop strain

seems to decrease in comparison with the slope value case. This is simply due to the mathematical method in Hughes et al.'s simplified analysis where the friction angle is calculated from the slope value.

In the following sections, the corrected values are examined, since the corrected values are thought to be those found under the realistic conditions.

The effects of length-to-diameter ratio

The effects of the length-to-diameter ratio on the loading slope and the friction angle can be seen in Figure 36 to 39. Figure 36 shows comparisons between corrected measured and exact slope using central hoop strain. In Figure 36, it is found that the overestimation found in the corrected measured slope (s_{cm}) depends highly on the length-to-diameter ratio and varies almost linearly with the

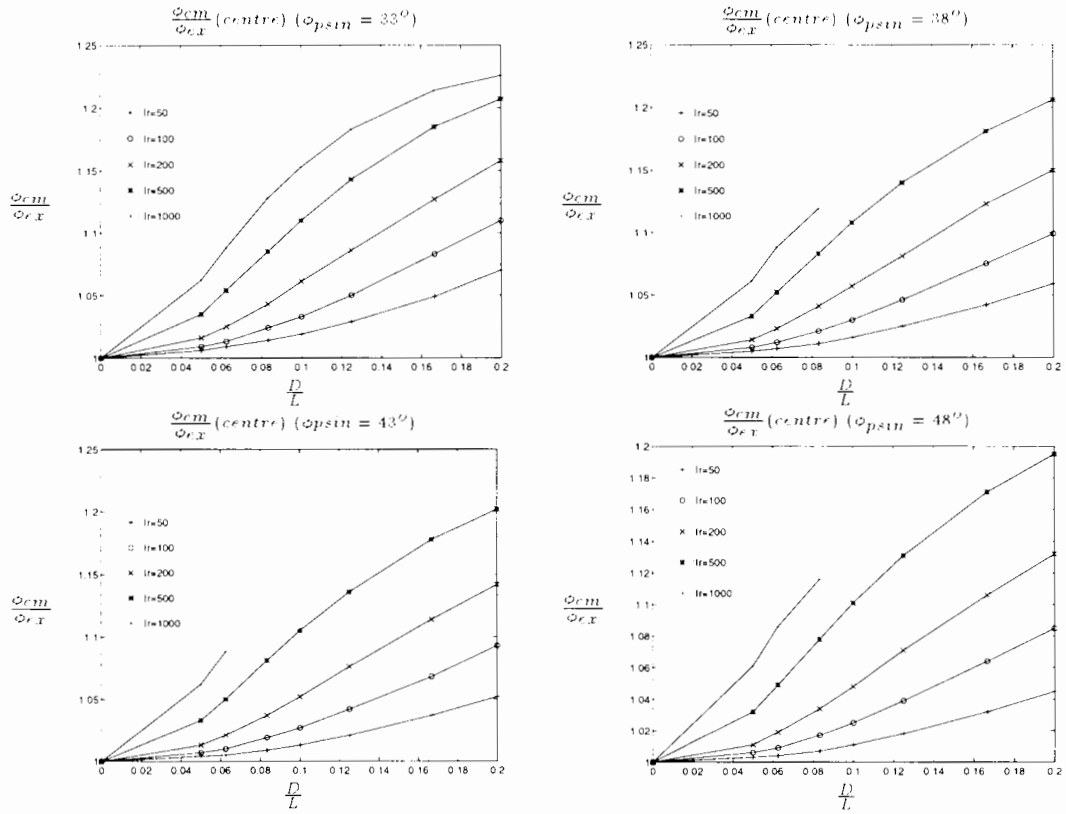


Figure 37: A comparison between σ_m and σ_{cx} using central hoop strain

length-to-diameter ratio. However, as found in high I_s values, such as $I_s = 1000$ or 500, the overestimation seems to become more constant. The overestimation due to the length-to-diameter ratio does not effect much the corrected measured slope for $I_s = 50$, since the deviation is less than 9 %. Particularly, for $I_s = 50$ and $\sigma_{psin} = 48°$, the deviation is 5.8 % at most. On the other hand, when I_s is equal to 500, the deviation is more than 25 %. This means that if the stiffness index is high, the effects of length-to-diameter ratio are significant.

Figure 37 shows comparisons between corrected measured and exact friction angle using central hoop strain. The overestimation found in the friction angle is, in general, less than the overestimation found in the slope. This is simply because of the mathematical relationship between the slope value and the friction angle value. The trend of the overestimation found in the friction angle itself is very similar to the trend of the overestimation found in the slope. Therefore, it can

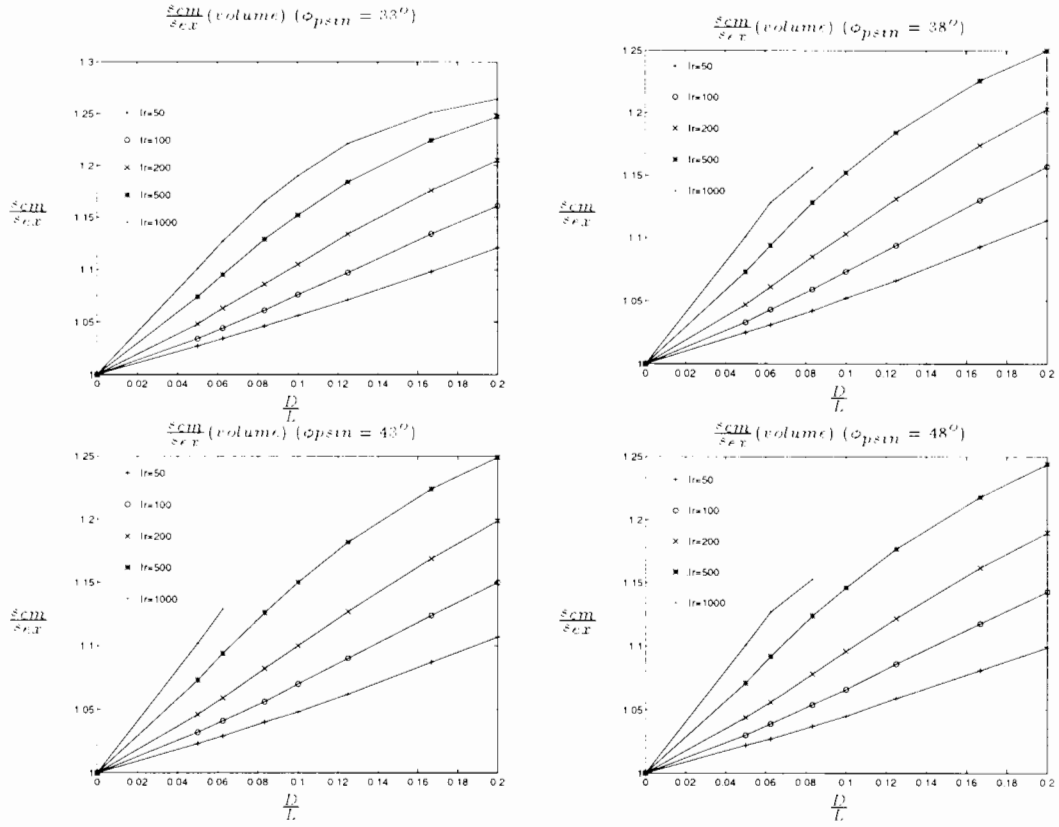


Figure 38: A comparison between s_{cm} and s_{cx} using volumetric hoop strain

be said that the overestimation due to the length-to-diameter ratio becomes less when the input friction angle (φ_{psin}) and the stiffness index are small and the overestimation is less than that found in the slope.

Figure 38 shows comparisons between corrected measured and exact slope using volumetric hoop strain. The derived value using volumetric hoop strain has more overestimation than that using central hoop strain. However, the difference is small and less than 3%. Therefore, it does not matter significantly whether volumetric hoop strain or central hoop strain is taken into account.

Figure 39 shows comparisons between corrected measured and exact friction angle using volumetric hoop strain. As mentioned before, the tendency found in the overestimation of the friction angle is similar to the tendency found in the slope. This results in the fact that the overestimation of the friction angle found

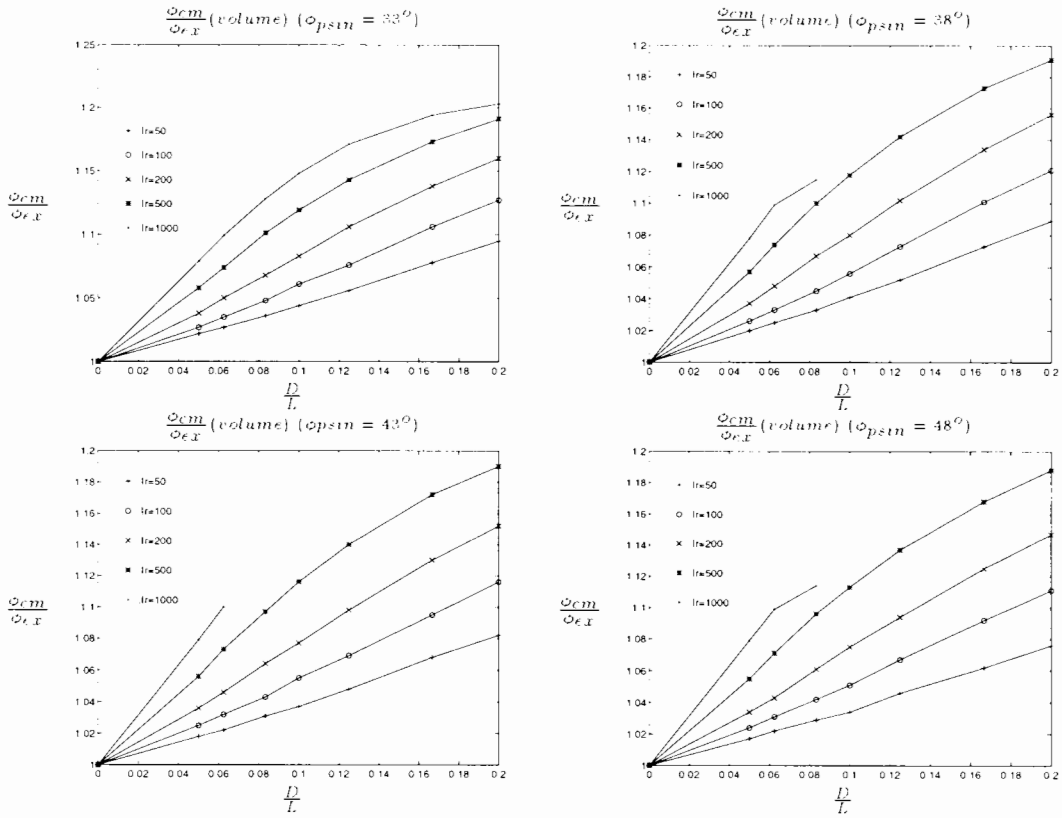


Figure 39: A comparison between Φ_{cm} and Φ_{ex} using volumetric hoop strain

in the volumetric hoop strain is found to be more than that in the central hoop strain.

On the whole, it can be derived that the overestimation of the slope due to the length-to-diameter is significant when the stiffness index is more than 50, since the overestimation become more than 10%. In contrast, when the stiffness index is equal to 50 and especially when the friction angle is high, the overestimation is less than 6% using the central hoop strain. The overestimation does not seem to be influenced much by whether the central hoop strain or volumetric hoop strain is used. The overestimation of the friction angle is less than that of the slope due to the mathematical procedure by Hughes *et al.*. The same tendency as found in the slope can be seen in the friction angle. The overestimation is almost linear with the D/L ratio, except when $\phi_{psin} = 33^{\circ}$, $I_s = 500$ or 1000. Examining the data derived from small ϕ_{psin} (=33° or 38°) values and large I_s (=500° or 100°) values , it is found that the overestimation slightly becomes approximately constant.

The effects of stiffness index

The effects of the stiffness index (I_s) is examined here. Figure 40 and 41 shows a comparison between the corrected measured slope value using the central strain and the exact solution based slope value. It is obvious that the effect of the rigidity index is large when the D/L ratio is small. As the I_s value increases, the overestimation increases. When the length-to-diameter ratio is less than 10, the overestimation is almost linear with the stiffness index. This means that when using a short pressuremeter and investigating rather stiff ground, the overestimation may turn out to be big. On the other hand, if the ground is not stiff, the pressuremeter will give a good estimation.

Figure 42 and 43 shows a comparison between the corrected measured friction angle using the central strain and the exact solution based friction angle value. The same tendency found in the slope value can be seen in the friction angle value. The overestimation in the friction angle is less than that in the slope.

As discussed before, the difference between the slope values using the central strain and the volumetric strain is small and these trends are same.

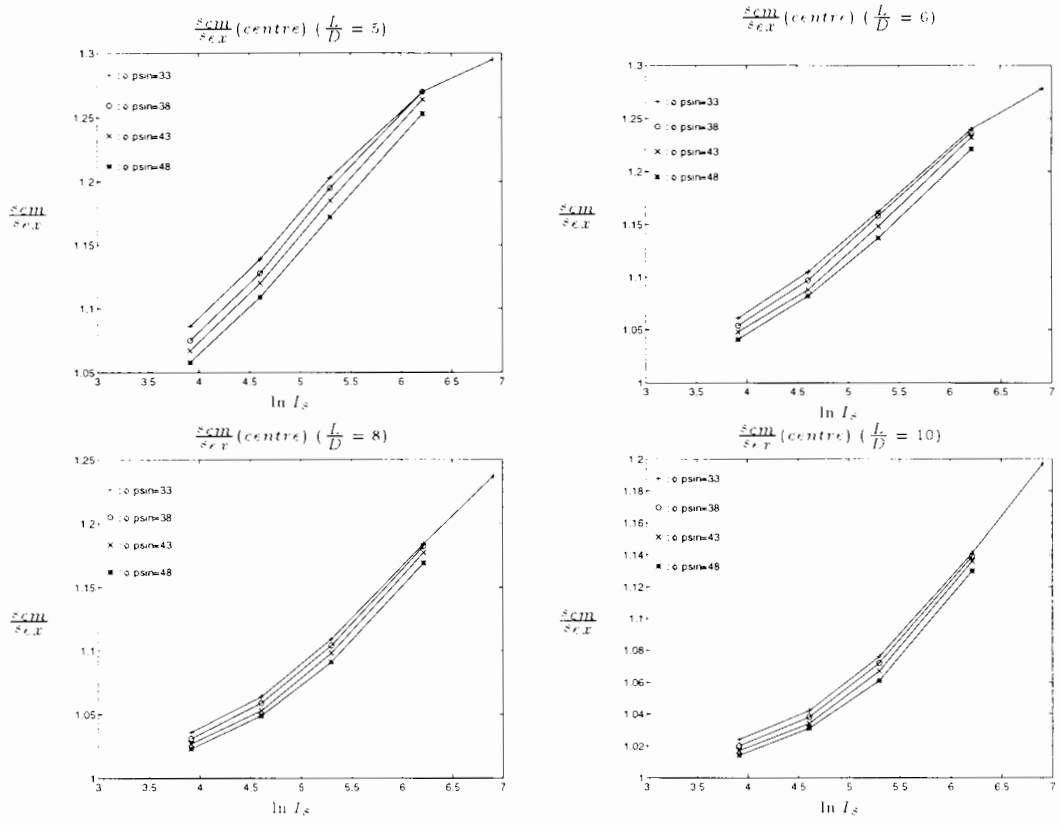


Figure 40: A comparison between s_{cm} and $s_{\epsilon x}$ using central strain (L/D = 5, 6, 8, 10)

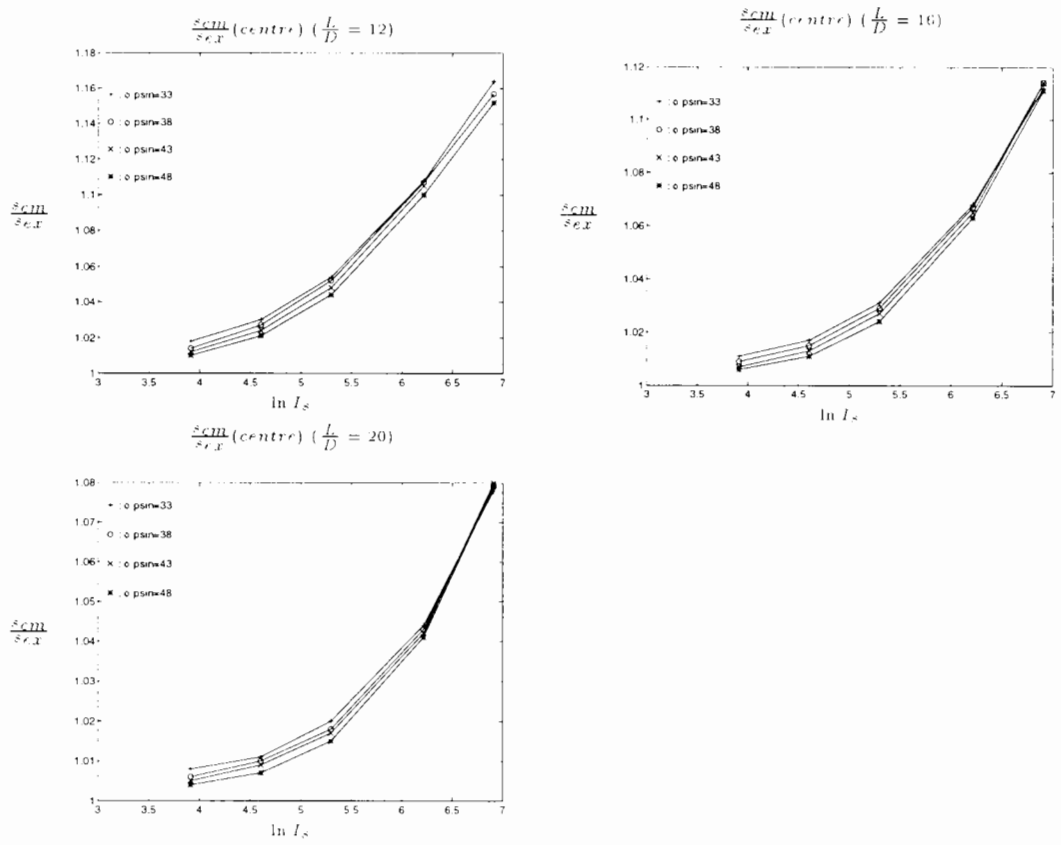


Figure 41: A comparison between s_{cm} and s_{ex} using central strain (L/D = 12, 16, 20)

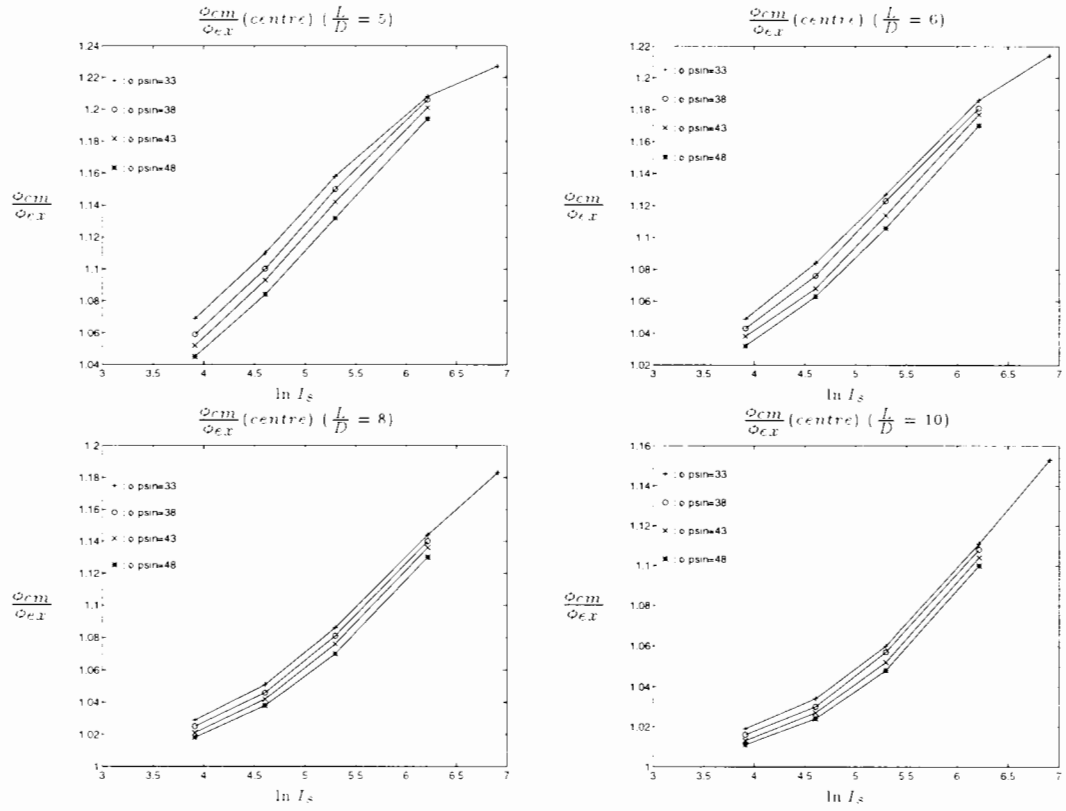


Figure 42: A comparison between σ_{cm} and σ_{ex} using central strain ($L/D = 5, 6, 8, 10$)

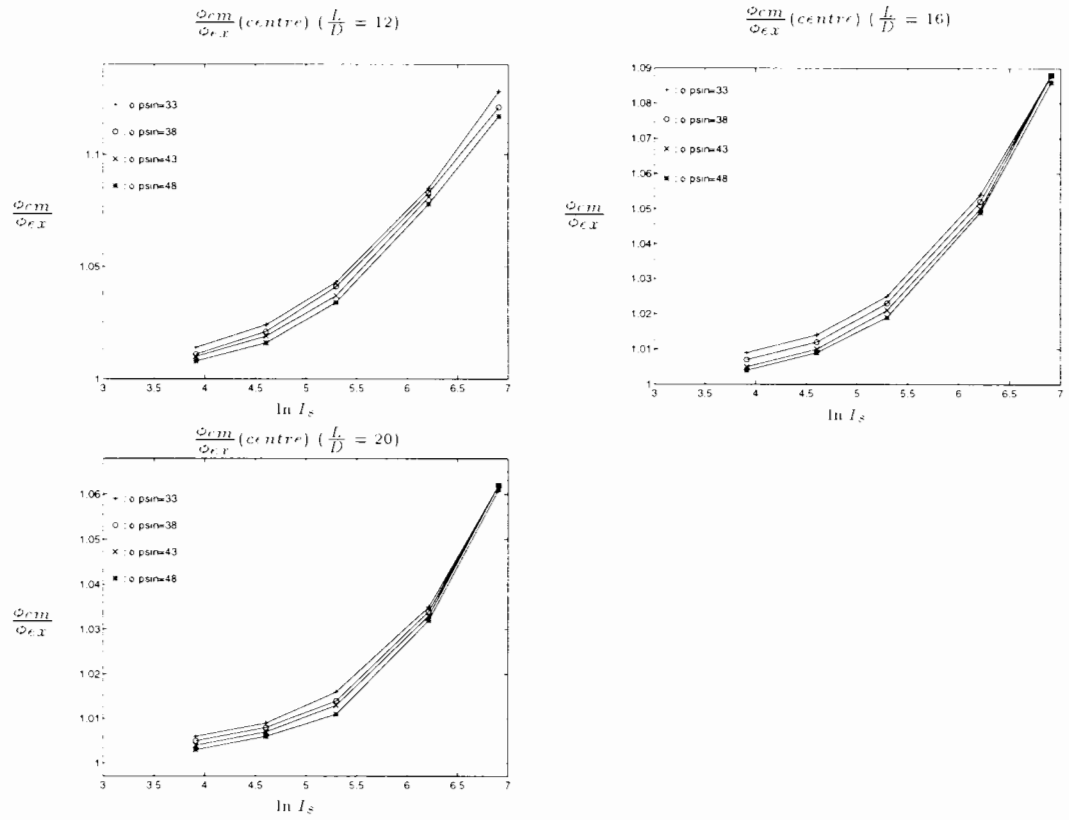


Figure 43: A comparison between σ_{cm} and σ_{ex} using central strain (L/D = 12, 16, 20)

The effects of friction angle

As is shown in Figure 40 to 43, the effects of friction angle is found to have little influence on the derived values in comparison with the effects of the length-to-diameter ratio and the stiffness index. The maximum deviation due to the input friction angle value (ϕ_{psin}) is less than 3% both in central strain and volumetric strain. Considering the fact that the friction angle depends highly on the density when the sand material is the same, this implies that the density does not have a significant influence on the pressuremeter test results when the rigidity index and the length-to-diameter ratio is constant. This is in agreement with Laier *et al.* (1975) who concluded from large chamber test results that the effects on the limit pressuremeter, derived from pressure-expansion curve, are largely independent of the soil density.

2.3 Recommended interpretation procedure

The self-boring pressuremeter which is widely used in practice has a length-to-diameter ratio, 6 (e.g. the Cambridge self-boring pressuremeter). Therefore, the self-boring pressuremeter analyses with the length-to-diameter equal to 6 are examined in detail here. Of course, the same argument may be used for self-boring pressuremeter tests with a different length-to-diameter ratio.

2.3.1 Self-boring pressuremeter tests in clay

For self-boring pressuremeter tests in clay, the effects of the length-to-diameter ratio on shear modulus is less than 0.8% when the central strain is taken into account. In addition, it seems that the effects of the rigidity has hardly any effect on the shear modulus. On the other hand, when the volumetric strain is taken into account, the overestimation is more than 7%. Therefore, it is recommended that the central strain should be used to measure shear modulus.

For undrained shear strength, when using the volumetric strain derived from the volumetric hoop strain and the shear strength is measured over the strain 2% to 5%, the overestimation is more than 14% and the effects of the rigidity index is

discernible although it is small. It does not matter much which strain range is used when the average volumetric strain from the volumetric hoop strain is taken into account. On the other hand, using the volumetric strain derived from the central hoop strain and the same strain range, the overestimation is more than about 10% and the overestimation is varied with the rigidity index more than the value from the volumetric strain derived from the central strain. The deviation is more than 10%. But, the deviation tends to decrease when using the strain range, 6% to 10% and 6% to 15%, and the deviation is less than 10%.

Considering that the strain range, 2% to 5% is widely used in practice, the volumetric strain from the volumetric hoop strain is recommended to measure the shear strength of clay, because the effects of the rigidity index is relatively small. When using the volumetric strain from the volumetric strain, the overestimation does not vary much due to the rigidity index and the overestimation is between 14% and 20% when the strain range, 2% to 5%, is used. This means that the finite length effects may be accounted for by multiplying the derived strength by a factor between 0.83 and 0.88.

2.3.2 Self-boring pressuremeter in sand

The results of the self-boring pressuremeter tests in sand show that the effects of the stiffness index and the length-to-diameter ratio on the slope, which is found when the pressure and the strain is plotted on double logarithmic scale and used to calculate the friction angle, is significant and the slope value is overestimated. However, they also showed that the effects of the input friction angle is not significant in comparison with the effects described above. This means that it does not matter much if the sand density is high or low. In addition, the trend which is found in the volumetric hoop strain case is the same as the trend found in the central hoop strain case, although the overestimation found in the central strain is a bit smaller.

Therefore, in the following discussion, the effects of the length-to-diameter ratio ($L/D = 6$) and the stiffness index are examined, assuming that the central hoop strain is taken into account. This is because the overestimation is relatively small. In addition, the most attention is paid to slope value here, since the friction angle

value can be derived from the slope value. This means that the correction of the overestimation in the friction angle is slightly indirect, by comparison with the slope value based correction.

The overestimation of the slope value increase between 4% and 28%, which leads to the overestimation of the friction angle between 3% and 21%, mainly due to the stiffness index as the stiffness index increase. The overestimation is almost linear with the logarithmic stiffness index value and the deviation due to the input friction angle value is less than 2% in any case. It is seen that the finite length effects may be accounted for by multiplying the derived slope by a factor of 0.78 to 0.96.

The other problem is that in Hughes *et al.*'s method the elastic deformation in the plastic area is ignored, with the result that the Hughes *et al.* method tends to underestimate the derived slope and also the friction angle. This underestimation depends on the stiffness index and the input friction angle. This means that the effect of the finite length of the pressuremeter depends both on the friction angle and the stiffness index, when taking the effects of ignoring elastic deformation in plastic area into account.

If the effects of ignoring elastic deformation in plastic area can be estimated simply by multiplying by a factor, s_{ex}/s_{in}, it is found that the slope value is overestimated when the stiffness index is large and the slope value is underestimated when the stiffness index value is small. This method is, to be strict, not sufficient to include the effects of the elastic deformation in plastic area, because the elastic deformation depends on the length-to-diameter ratio and, as a result, the effects of the elastic deformation in the plastic area cannot always be in the same proportion.

However, it is true that the value s_{cm}/s_{in} or o_{cm}/o_{tu} can account for the effects of the elastic deformation in the plastic area to some extent. Therefore, the following paragraph gives a discussion using the value s_{cm}/s_{in} or o_{cm}/o_{tu}

Figure 44 shows the combined effects on the slope due to finite length and elastic deformation. It is noticed that the slope value is underestimated with the small I_s value and high friction value when the elastic deformation in the plastic area is taken into account. It is interesting that when the I_s value is small the effect of the friction angle is slightly bigger. This means that the effects of density

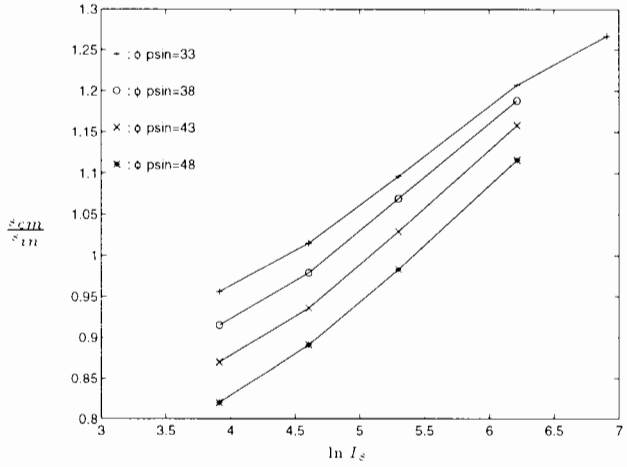


Figure 44: The combined effects on slope due to finite length and elastic deformation(centre)

is larger when the stiffness index is small.

Figure 45 shows the combined effect on the friction angle due to finite length and elastic deformation. The same trend as seen in Figure 44 can be found.

2.4 Final remark

The self-boring pressuremeter is used to obtain some fundamental soil parameters. In interpreting the data, it is assumed that the length of the pressuremeter is infinite. This chapter investigated the effects of the length-to-diameter ratio using the finite element method.

For self-boring pressuremeter tests in clay, it was found that the derived value of the soil stiffness and strength by use of the conventional Gibson and Anderson method is higher than the actual input value. This means that the conventional Gibson and Anderson method tends to overestimate the soil stiffness and strength. The overestimation in the shear modulus is negligible when the central hoop strain is taken into account. However, in the volumetric hoop strain case, the shear modulus is overestimated much. In addition, the overestimation does not seem to be influenced by the rigidity index.

On the other hand, the overestimation of the shear strength is significant. The

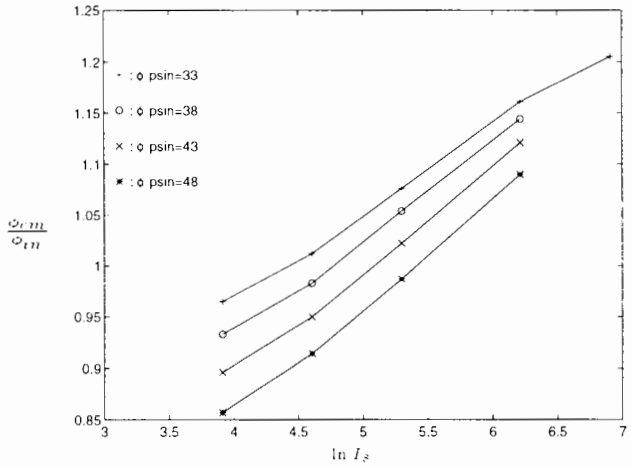


Figure 45: The combined effects on friction angle due to finite length and elastic deformation(centre)

overestimation depends on the length-to-diameter ratio, the rigidity index, and the strain range where the shear strength is measured.

For the self-boring pressuremeter tests in sand, serious overestimation of the strength parameter, friction angle, was found. The overestimation using the central volumetric strain is lower than that using the volumetric strain. However, the trend of the overestimation in the volumetric hoop strain is similar to that in the central hoop strain.

In addition, the effects of the elastic deformation in plastic area is studied comparing Yu's exact small strain solution and Hughes et al.'s simplified solution. It is found that Hughes et al.'s method tends to underestimate the friction angle.

Chapter 3

Study of the full-displacement pressuremeter

3.1 Introduction

This chapter explores the analyses of the full-displacement pressuremeter in clay by using the finite element program, OXFEM 1.45.

First of all, the pressuremeter expansion is modelled as a two-dimensional axisymmetric problem in a large strain elastic perfectly-plastic material. All of the tests are carried out with $\sigma_{h0} = 0.0$, since the horizontal stress appears simply as an additive term on all stresses. A value of $s_u = 1.0$ is used in all tests to normalize all stresses with respect to s_u.

Concerning a mesh used in this analysis, a mesh which is 50 in height and 80 in width is used to study of the effects of the length-to-diameter ratio (Figure 46). The mesh consists of 424 triangular elements of 6 nodes, with 913 nodes in total. The structure of the mesh is different from the meshes used in the analysis of a self-boring pressuremeter. The installation is modelled by expansion of a parallel cylinder from 0.25 radius, since it is not possible to expand from zero. Therefore, the initial displacement of the ground is set to 0.25 to keep the finite element calculation stable. Indeed, this differs from physical reality since there is no initial displacement in the ground. However, as mentioned, it is impossible to conduct analyses with zero initial radius because of numerical problems with the $\frac{1}{r}$ terms.

Figure 46: Mesh used in the full-displacement pressuremeter analysis

The analysis proceeds in six steps, a displacement control led phase, an initial expansion phase, a second expansion phase, an initial displacement control led section for unloading, an initial unloading phase and a second unloading phase. In the displacement control led section, the initial radial position of the inner boundary is set to 0.25 and then displaced to 1.0. In order to keep the calculation stable at the beginning of a plastic phase, the displacement control led phase consists of a small displacement increment stage and a large displacement increment. The first is a stage where the displacement is 0.25 with 50 steps. The latter is a stage where the displacement is 0.5 with 75 steps. These values are carefully chosen. In the second phase, the initial expansion phase, zero pressure is applied for a few steps to allow out of balance forces to be eliminated. Then, in the third phase, the main expansion phase, each pressure increment is set to $0.03s_u$. The pressuremeter is assumed as a rigid body the radius ($D/2$) of which is set to 1.0. As a result of the axisymmetry, the length of the pressuremeter seen in the mesh is equal to L/D. The value of the stress increment is carefully chosen since the area around pressuremeter is already plastic at the beginning of the expansion. When the radius of the central part of the pressuremeter reaches 1.3, then the third phase begins. In the third step, zero displacement is applied along the pressuremeter surface. In the initial unloading phase, a few small negative pressure increments are applied. Each

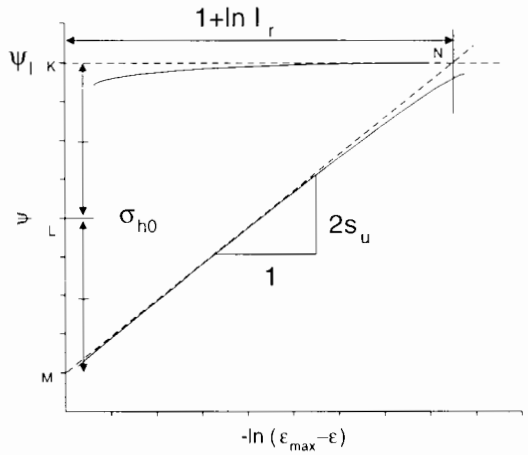


Figure 47: Houlsby and Withers(1988) analysis

negative pressure increment is set to $-0.025 s_u$. In the final phase, the unloading phase, each negative pressure is set to $-0.1 s_u$. Since it is very difficult to keep the analysis stable, the each loading or unloading pressure increment was carefully chosen. It was found that the analyses were sensitive to the choice of step size. The pressure increment was chosen by trial and error to keep analysis as stable as possible.

For an infinitely long pressuremeter, it is impossible to perform pressure expansion numerically by a pressure control as for a finite length pressuremeter. Therefore, a displacement controlled analysis was used for modelling pressuremeter tests with an infinitely long pressuremeter. In the first phase, the same displacement phase as in a finite long pressuremeter analysis is used. Then, in the second phase, the inner boundary is displaced from 1.0 to 1.3 with 200 steps again to allow out of balance forces to be eliminated. Then, in the final phase, the boundary is displaced to 1.0 again with 500 steps.

3.2 Procedure of Interpretation

In order to interpret the data correctly, a correction method is necessary to eliminate the inaccuracies due to the non-linear solution algorithm.

According to the theory for an infinitely long pressuremeter by Houlsby and Withers (1988), after the strain reached at its maximum value ϵ_{max}, plotting the pressuremeter pressure v against $-\ln(\epsilon_{max}-\epsilon)$ gives a straight line the gradient of which is equal to $2s_u$ (Figure 47). In their analyses, this slope is used to measure the shear strength. It is also known that the line passes through the point $(0, 2\sigma_{h0}-v_l)$, where σ_{h0} and v_l are initial horizontal stress and limit pressure respectively. Therefore, the mid point of K $(0, v_l)$ and M $(0, 2\sigma_{h0}-v_l)$, named L, is $(0, \sigma_{h0})$. Therefore, the mid point of K and M gives the initial horizontal stress. In addition, the abscissa of the intercept of the limit pressure and the plastic unloading line (point N) is used to determine the I_r value.

In practice, the same method is used to interpret the data, although the length of the pressuremeter is finite. Therefore, in the analyses, the same interpretation method as used for an infinitely long pressure is used. The pressure is plotted against $-\ln(\epsilon_{max}-\epsilon)$ and the shear strength is measured from the gradient of the approximately straight line obtained. Then, following the same procedure as for an infinitely long pressuremeter, the rigidity index value is determined. Then, multiplying the measured rigidity index and the shear strength gives the measured shear modulus. Finally, adding the y-intercept of the line and the limit pressure, which is the maximum pressure found in the test, and dividing the sum by 2.0 gives the measured horizontal stress value.

Then, an infinitely long pressuremeter analysis is used to perform a correction.The shear strength, rigidity index, shear modulus, and the initial horizontal stress are measured. As mentioned before, s_u means a triaxial compression undrained shear strength which corresponds to a plane strain undrained shear strength of $\frac{2}{\sqrt{3}}s_u$. Therefore, all the undrained shear strength values derived from the analysis are multiplied by $\frac{\sqrt{3}}{2}$ and all the rigidity index values derived from the analysis is multiplied by $\frac{2}{\sqrt{3}}$.

As a result, the measured shear strength turns out to be near 1.0 and the rigidity index is near input rigidity index value. The shear modulus is also appears to be near the input value. The measured initial horizontal stress is found to be near 0.0.

For the s_u value, the correction method is the same as the method in self-boring pressuremeter analysis. The measured shear strength (s_{um}) is multiplied by the ratio of the input shear strength (s_{uin}) to the measured shear strength for an infinitely long case (s_{um}^{∞}). When the shear strength is corrected, the line shifts horizontally in a linear fashion. This effects the rigidity index on logarithmic scale. Therefore, the correction method is to multiply the ratio of input rigidity index value (I_{rin}) to measured value for an infinitely long case (I_{rm}^{∞}). When the shear strength is corrected, initial horizontal stress moves linearly. Therefore, the correction method is to add the difference between the input initial horizontal stress (σ_{h0in}) and the measured initial horizontal for an infinitely long case (σ_{h0m}^{∞}). The measured shear modulus is corrected by multiplying the ratio of the input shear modulus (G_{in}) to the measured shear modulus for an infinitely long case (G_m^{∞}). This corrected shear modulus value is exactly the same as the one which is calculated on the basis of the corrected shear strength and rigidity index values.

Therefore, the corrected measured shear strength (s_{ucm}), rigidity index (I_{rcm}), shear modulus (G_{cm}), horizontal stress (σ_{h0cm}) and the limit pressure (v_{lcm}) are as follows:

$$\begin{aligned} s_{ucm} &= s_{um}\frac{s_{uin}}{s_{um}^{\infty}} \\ I_{rcm} &= I_{rm}\frac{I_{rin}}{I_{rm}^{\infty}} \\ G_{cm} &= G_m\frac{G_{in}}{G_m^{\infty}} \\ \sigma_{h0cm} &= \sigma_{h0m} + (\sigma_{h0in} - \sigma_{h0m}^{\infty}) \\ v_{lcm} &= v_{lm} + (v_{lin} - v_{lm}^{\infty}) \end{aligned} \tag{86}$$

where

$$v_{lin} = \frac{\sqrt{3}}{2}s_{uin}(1 + \ln\frac{2}{\sqrt{3}}I_{rin}) \tag{87}$$

The whole interpretation procedure is shown in Figure 48.

3.3 Numerical results

A total of 30 finite element analyses were completed, all possible combinations of 6 values of L/D and 5 values of I_r were analysed.

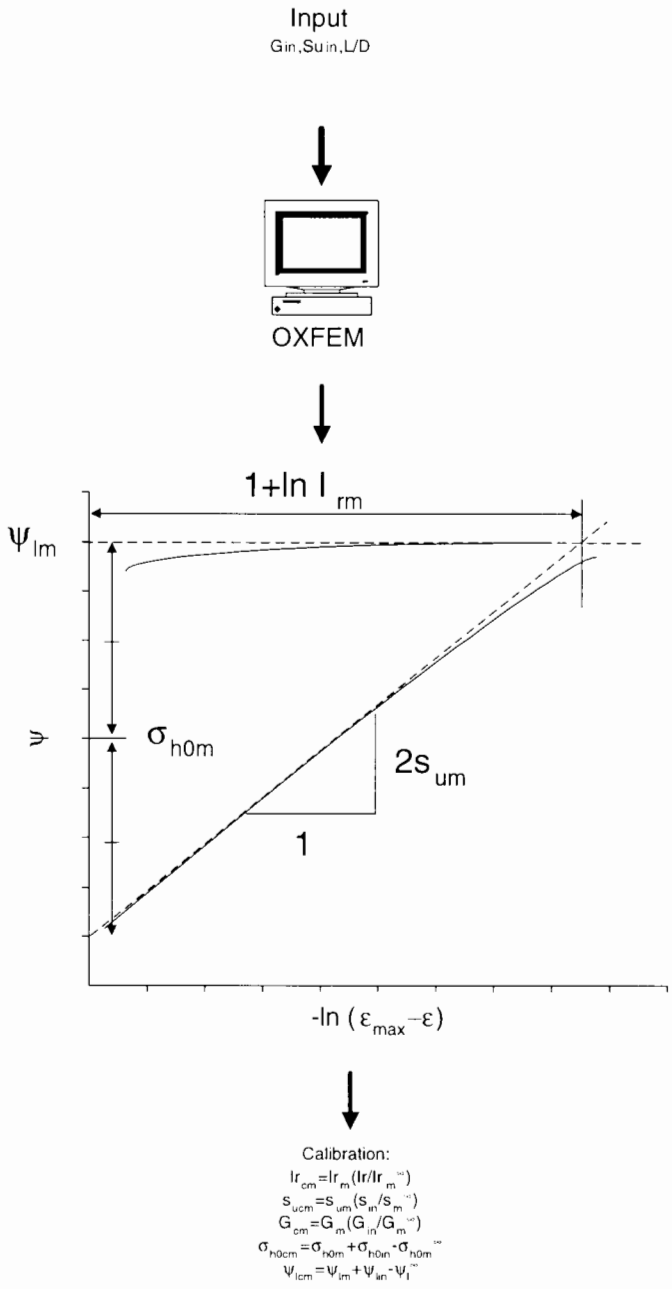


Figure 48: Procedure of interpretation

The results of all analyses are summarized in Table 17 and 18. Table 17 shows measured values and Table 18 shows corrected measured values divided by input values.

Figure 49 shows the distribution of σ_r in the loading stage. The length-to-diameter ratio is equal to 6. Figure 50 shows the distribution of $\tau_{r\theta}$ at the same stage. The stress distribution indicates that end-effects are found in this case. Figure 51 shows the plastic area around the pressuremeter. It is found that the shape of the plastic area is completely different from that found in self-boring pressuremeter analysis. In the full-displacement pressuremeter analyses, the area around the pressuremeter is initially compressed and yielded, with the result that the area around the full-displacement pressuremeter is easily yielded in comparison with the self-boring pressuremeter. All the plots (Figure 49 to 51) discussed above show a detail from the bottom left-hand corner of the large mesh (Figure 11).

Typical results are shown in Figure 52. As seen in Figure 52, the limit pressure is found to be higher as the length-to-diameter ratio decreases. This has effects on the measured initial horizontal stress.

The following sections investigate the effects of the length-to-diameter ratio and the rigidity index.

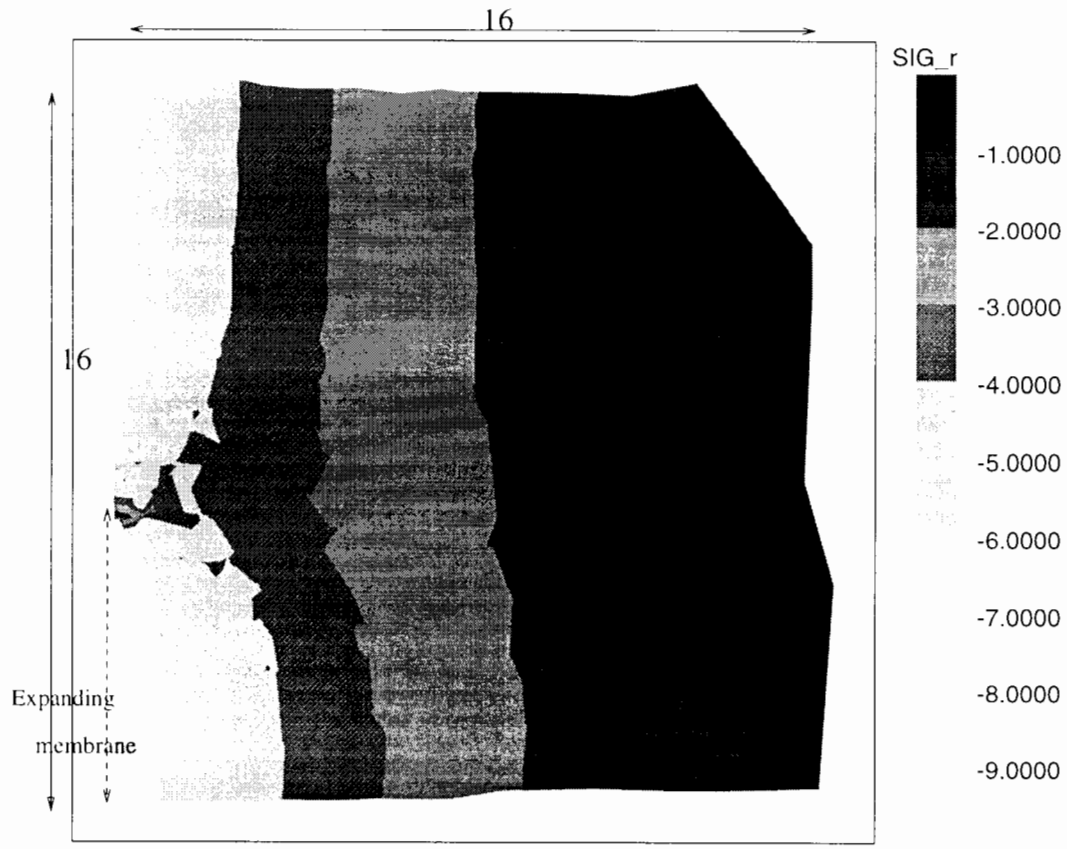


Figure 49: Distribution of σ_r for $I_r = 200$, $L/D = 6$. (contours at intervals of s_u)

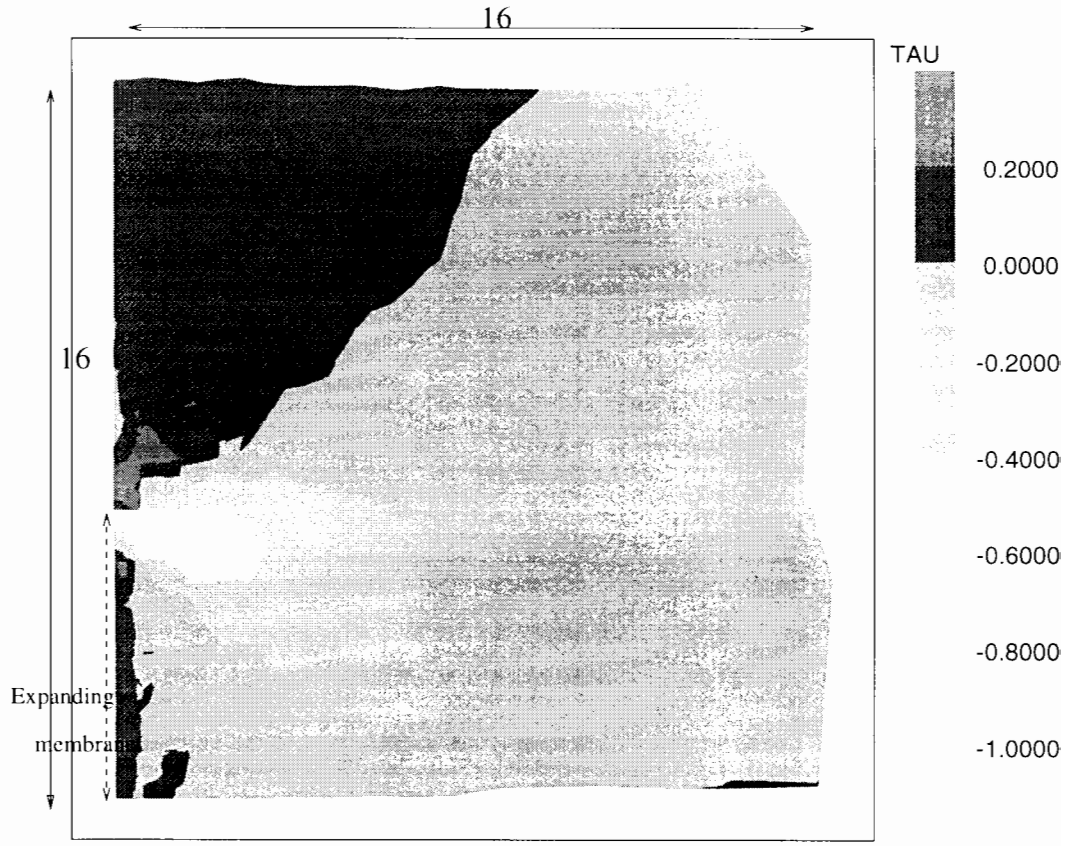


Figure 50: Distribution of $\tau_{r\theta}$ for $I_r = 200, L/D = 6$, (contours at intervals of $0.2s_u$)

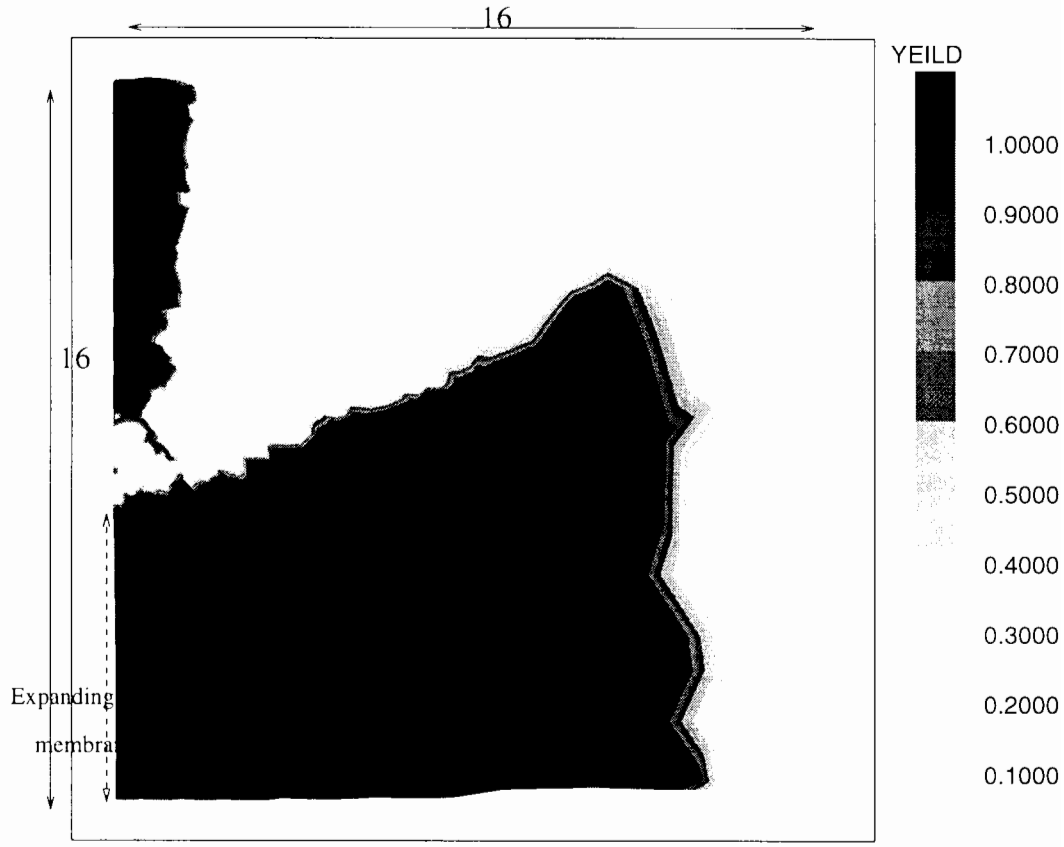


Figure 51: Plastic area for $I_r = 200$. $L/D = 6$. (dark shaded area is the plastically deforming zone)

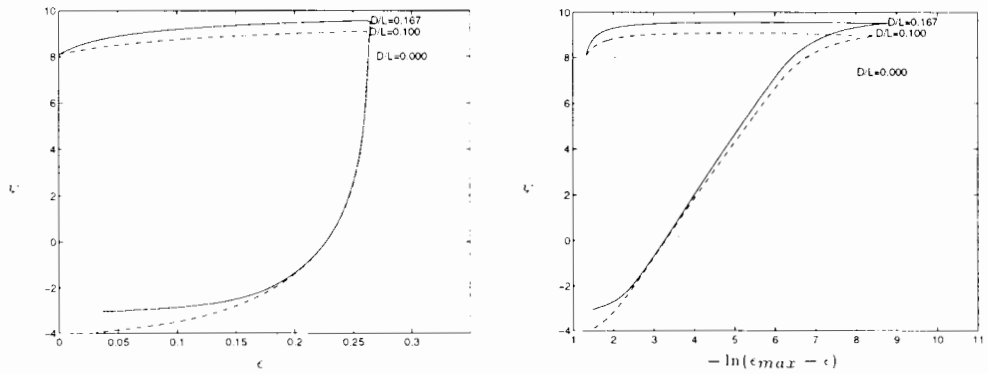


Figure 52: Typical pressuremeter curves from finite element analysis of full-displacement pressuremeter ($I_r = 200$)

I_{rin}	L/D	I_{rm}	s_{um}	G_m	σ_{h0m}	ψ_{lm}
50	6	45.90	1.095	50.25	0.10	6.02
50	8	46.81	1.059	49.57	0.14	5.89
50	10	47.69	1.036	49.42	0.15	5.80
50	12	48.12	1.025	49.31	0.14	5.74
50	16	49.89	1.014	50.58	0.13	5.71
50	∞	50.32	0.977	49.15	0.01	5.39
100	6	88.45	1.118	98.88	0.16	7.05
100	8	91.34	1.074	98.11	0.21	6.87
100	10	93.57	1.049	98.17	0.22	6.75
100	12	95.18	1.033	98.34	0.22	6.67
100	16	96.85	1.017	98.50	0.19	6.56
100	∞	100.67	0.982	98.84	-0.02	6.18
200	6	174.28	1.126	196.31	0.31	8.14
200	8	182.86	1.078	197.21	0.35	7.90
200	10	185.32	1.054	195.38	0.35	7.75
200	12	190.88	1.034	197.30	0.36	7.64
200	16	194.26	1.018	197.72	0.30	7.50
200	∞	203.86	0.980	199.74	-0.01	6.97
500	6	409.80	1.154	473.09	0.49	9.65
500	8	422.50	1.109	468.74	0.51	9.35
500	10	437.79	1.078	471.92	0.51	9.14
500	12	453.65	1.055	478.44	0.51	9.00
500	16	471.50	1.030	485.67	0.45	8.79
500	∞	510.01	0.981	500.14	-0.01	8.02
1000	6	771.73	1.178	908.83	0.60	10.80
1000	8	787.71	1.137	895.34	0.59	10.47
1000	10	819.66	1.103	903.84	0.60	10.23
1000	12	855.89	1.076	920.98	0.62	10.07
1000	16	906.73	1.044	946.22	0.57	9.81
1000	∞	1046.24	0.975	1020.36	0.02	8.82

Table 17: Results of measured values from finite element analysis of full displacement pressuremter

I_{rin}	L/D	$\frac{I_{rcm}}{I_{rin}}$	$\frac{s_{ucm}}{s_{uin}}$	$\frac{G_m}{G_{in}}$	σ_{h0cm}	$\frac{\psi_{lcm}}{\psi_{lin}}$
50	6	0.912	1.121	1.022	0.09	1.11
50	8	0.930	1.084	1.009	0.13	1.09
50	10	0.948	1.061	1.005	0.14	1.07
50	12	0.956	1.049	1.003	0.14	1.06
50	16	0.991	1.038	1.029	0.12	1.06
50	∞	1.000	1.000	1.000	0.00	1.00
100	6	0.879	1.139	1.000	0.18	1.14
100	8	0.907	1.094	0.993	0.22	1.11
100	10	0.929	1.069	0.993	0.23	1.09
100	12	0.945	1.052	0.995	0.23	1.08
100	16	0.962	1.036	0.997	0.20	1.06
100	∞	1.000	1.000	1.000	0.00	1.00
200	6	0.855	1.150	0.983	0.32	1.16
200	8	0.897	1.101	0.987	0.36	1.13
200	10	0.909	1.076	0.978	0.36	1.11
200	12	0.936	1.055	0.988	0.37	1.09
200	16	0.953	1.039	0.990	0.31	1.07
200	∞	1.000	1.000	1.000	0.00	1.00
500	6	0.804	1.177	0.946	0.49	1.20
500	8	0.828	1.131	0.937	0.51	1.16
500	10	0.858	1.099	0.944	0.51	1.14
500	12	0.889	1.075	0.957	0.51	1.12
500	16	0.924	1.050	0.971	0.46	1.09
500	∞	1.000	1.000	1.000	0.00	1.00
1000	6	0.738	1.208	0.891	0.57	1.22
1000	8	0.753	1.165	0.877	0.57	1.18
1000	10	0.783	1.131	0.886	0.58	1.16
1000	12	0.818	1.103	0.903	0.59	1.14
1000	16	0.867	1.070	0.927	0.55	1.11
1000	∞	1.000	1.000	1.000	0.00	1.00

Table 18: A comparison between corrected measured and input values from finite element analysis of full displacement pressuremter

3.4 Effects of length-to-diameter ratio

First, the effects of the length-to-diameter ratio on the results are discussed.

3.4.1 Rigidity index

The effects of the length-to-diameter ratio on the corrected measured rigidity index are seen in Figure 53. As seen in Figure 53, the corrected measured rigidity index decreases when the length-to-diameter ratio decrease. This means that the rigidity index is underestimated. The underestimation is more as the input rigidity index increase. Focusing on the slope of each line, it is said that the effects of the length-to-diameter ratio depends highly on the input rigidity index. For instance, the variation of the underestimation for $I_r = 1000$ is more than 25%, however, that for $I_r = 100$ is less than 7%.

3.4.2 Shear strength

The effects of the length-to-diameter ratio on the corrected measured undrained shear strength are seen in Figure 54. It is found that the shear strength is overestimated more as the length-to-diameter ratio decreases. When the rigidity index is more than or equal to 200, the overestimation increase as the rigidity index increase. However, when the rigidity index is less than or equal to 100, the overestimation decrease as the rigidity index increase. This is interesting since the opposite trend is found in the rigidity index. Considering that the rigidity index is a value of the shear modulus divided by the shear strength, this indicates that the shear modulus is almost constant. Assuming that the lines found in the Houlsby and Withers analysis passe the same point near the origin, this phenomena is reasonable. Because increase of the shear strain value leads to increase of the slope, then, as a result, this leads to decrease of $\ln I_r$ value. Therefore, from a certain angle, it is possible to estimate the overestimation of the rigidity index value from the shear strength value.

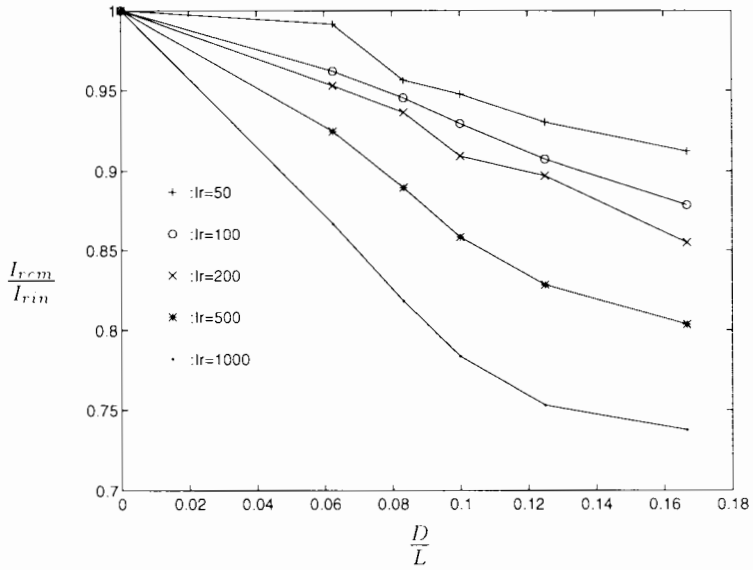


Figure 53: The effects of the length-to-diameter ratio on the calculated rigidity index

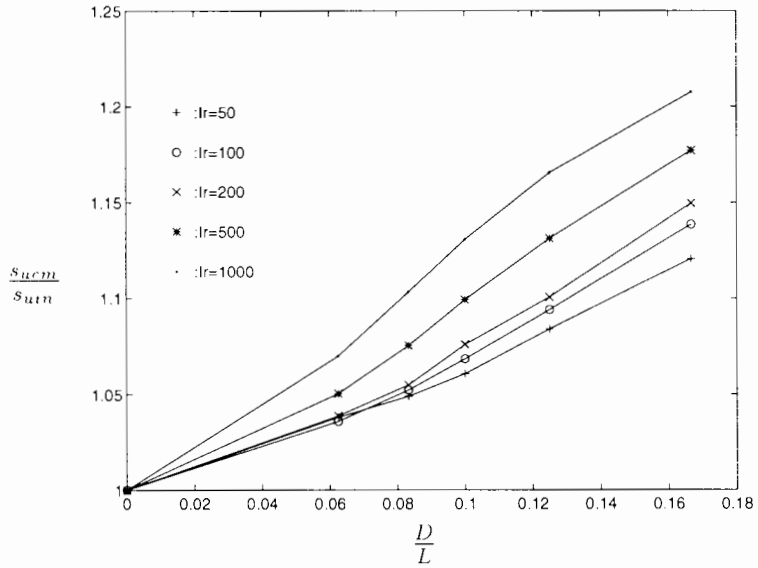


Figure 54: The effects of the length-to-diameter ratio on the calculated shear strength

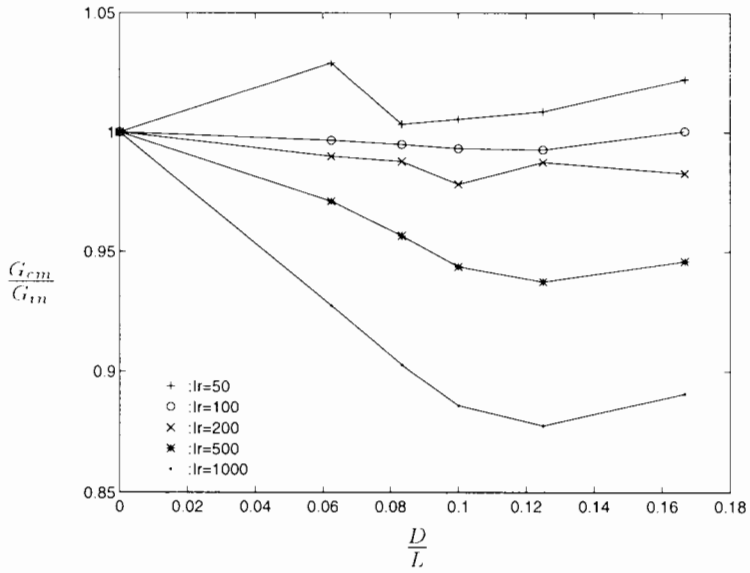


Figure 55: The effects of the length-to-diameter ratio on the calculated shear modulus

3.4.3 Shear modulus

As seen in Figure 55, the shear modulus is overestimated when the rigidity index is less than or equal to 100. On the the hand, when the rigidity index is more than or equal to 200, the shear modulus is underestimated. Thinking that multiplying the rigidity index and shear strength gives the shear modulus, the result of the shear modulus means that the underestimation of the rigidity index has a stronger effect than the overestimation of the shear strength when the rigidity index is less than or equal to 100 and the opposite phenomena happens when the rigidity index is more than or equal to 200. The underestimation or overestimation of the shear modulus is not important when the rigidity index is less than 5, since the overestimation or underestimation valued is within 6%. However, when the rigidity index is 1000, the underestimation is important because the underestimation value is more than 10% when the length-to-diameter ratio is less than 12. This also means that the rigidity index is underestimated much when the rigidity index is 1000.

3.4.4 Initial horizontal stress

Figure 56 shows the effects of the length-to-diameter ratio on the corrected measured initial horizontal stress. In the figure, the value of $\frac{\sigma_{h0cm}-\sigma_{h0}}{s_{uin}}$ is used since all of the values should be normalized by the shear strength value. However, because the input value of the shear strength and the horizontal stress is 1.0 and 0.0 respectively, the value of $\frac{\sigma_{h0cm}-\sigma_{h0}}{s_{uin}}$ is the same as the corrected measured initial horizontal stress value. The initial horizontal stress is always overestimated. As seen in Figure 56, the effects of the length-to-diameter ratio on the initial horizontal stress are not large in comparison with the effects of the rigidity index especially when the length-to-diameter ratio is more than or equal to 12. This means that when the rigidity index is the same, the overestimation of the initial horizontal stress is not much influenced by the length-to-diameter ratio. It is found that the overestimation is high when the rigidity index is high. Considering the fact that every value is normalized by the shear strength value, this indicates that the overestimation of the initial horizontal stress can be highly overestimated when both of the shear modulus and the shear strength are high.

3.4.5 Limit pressure

Figure 57 shows the effects of the length-to-diameter ratio on the limit pressure. As is found in Figure 57, the limit pressure increases as the length-to-diameter ratio decreases. The increase of the limit pressure seems nearly linear with the D/L ratio. The slope of the line becomes slightly larger when the rigidity index value increases. This means that the effects of the rigidity index is also significant.

3.5 Effects of rigidity index

The effects of the rigidity index on the results are examined here.

3.5.1 Rigidity index

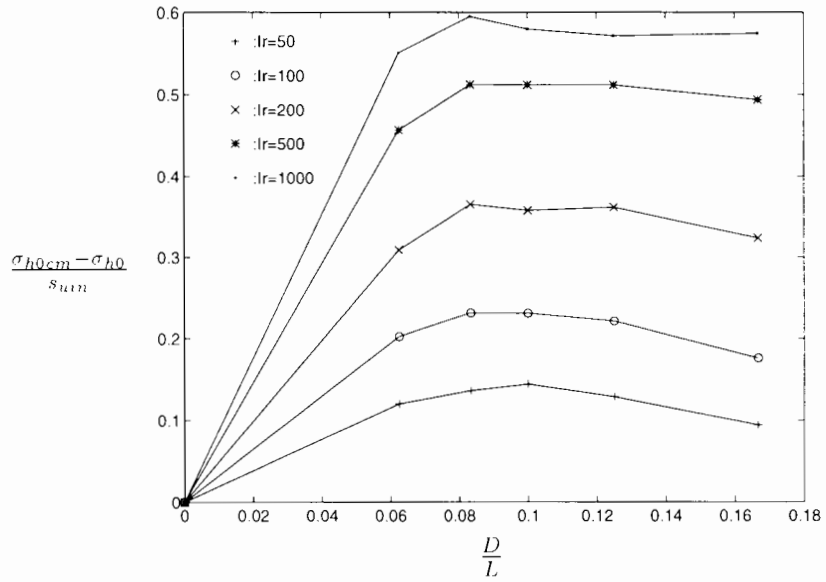


Figure 56: The effects of the length-to-diameter ratio on the calculated initial horizontal stress

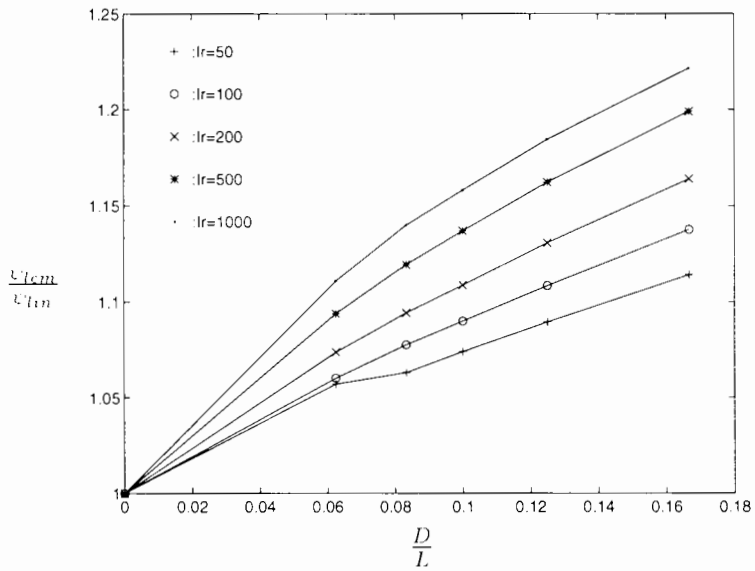


Figure 57: The effects of the length-to-diameter ratio on the calculated limit pressure

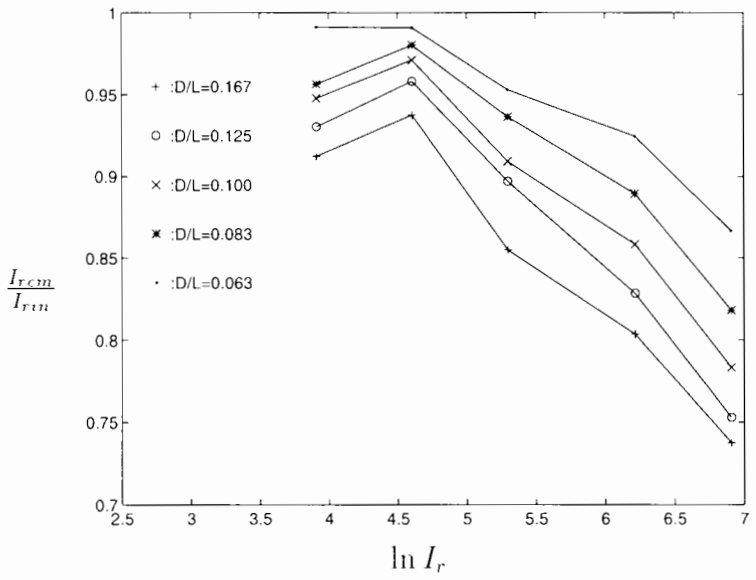


Figure 58: The effects of the input rigidity index on the calculated rigidity index

The effects of the rigidity index on the corrected measured rigidity index is seen Figure 58. It is interesting that there is a peak value near $I_r = 100$ in each line. The corrected measured rigidity index is highly underestimated when the input rigidity index is equal to 1000 (14% to 26%). The slope of each line seems almost the same and they are parallel with each other. This means that the underestimation consists of two categories: one is the effects of the length-to-diameter ratio effects, which has the same effects even with different rigidity index values. Second is the effects of the input rigidity index, which varies with input rigidity index and almost linear with the logarithmic input rigidity index value.

3.5.2 Shear strength

Figure 59 shows the effects of the rigidity index on the corrected measured shear strength. It is noticed that there is a minimum value near $I_r = 100$. As discussed in the previous section, this is reasonable if considering the line in the Houlsby and Withers analysis. However, focusing on the slope line which appears when the rigidity index is more than or equal to 100, the gradient of the slope is slightly steeper as the length-to-diameter ratio decreases. For instance, the slope

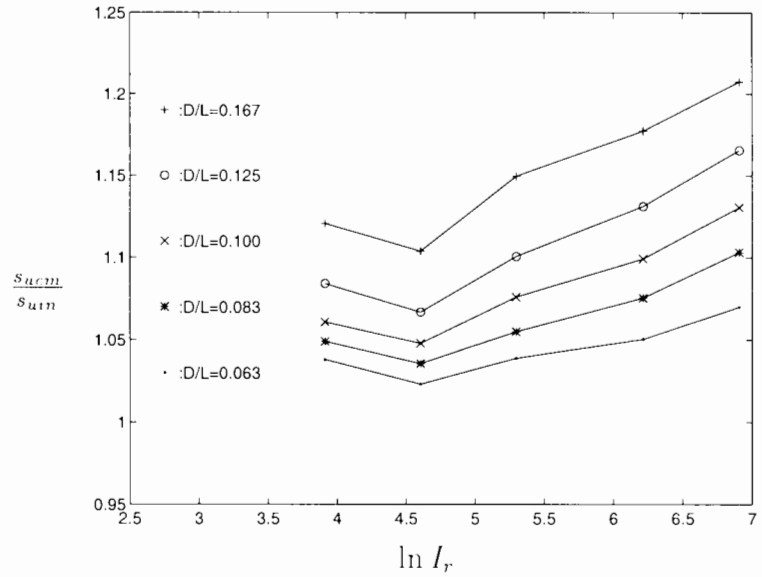


Figure 59: The effects of the input rigidity index on the calculated shear strength

for $L/D = 16$ is twice as large as the slope for $L/D = 6$.

3.5.3 Shear modulus

Figure 60 shows the effects of the rigidity index on the corrected measured shear modulus. All data seem to be on the same line with maximum deviation of the G_{cm}/G_{in} value less than 5% when rigidity index is equal to 1000. Therefore, it can be said that the effects of the length-to-diameter ratio has hardly any significance on the shear modulus. This also leads to the fact that multiplying the corrected measured shear strength and corrected rigidity index eliminates the effects of the length-to-diameter ratio. It is also found that the overestimation or the underestimation of the shear modulus is rather small in comparison with the shear strength and rigidity index.

3.5.4 Initial horizontal stress

The overestimation of the initial horizontal stress found to be nearly linear to the logarithmic rigidity index. Although it seems that all data is on the same line

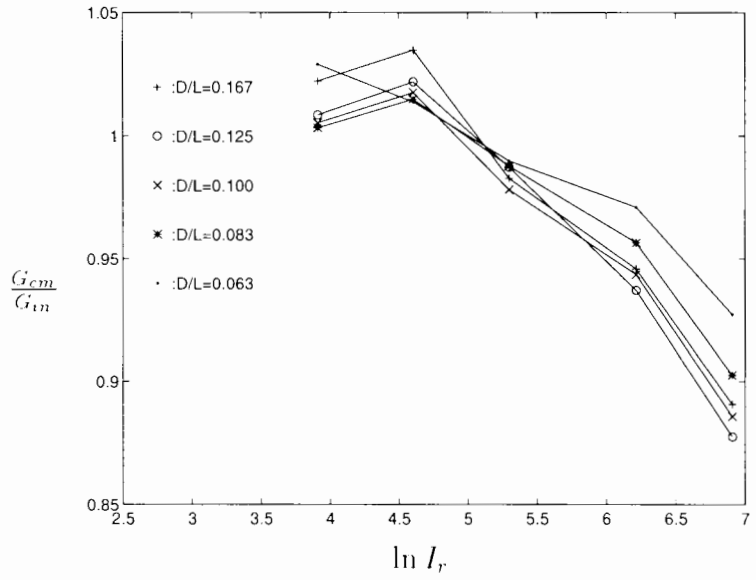


Figure 60: The effects of the input rigidity index on the calculated shear modulus

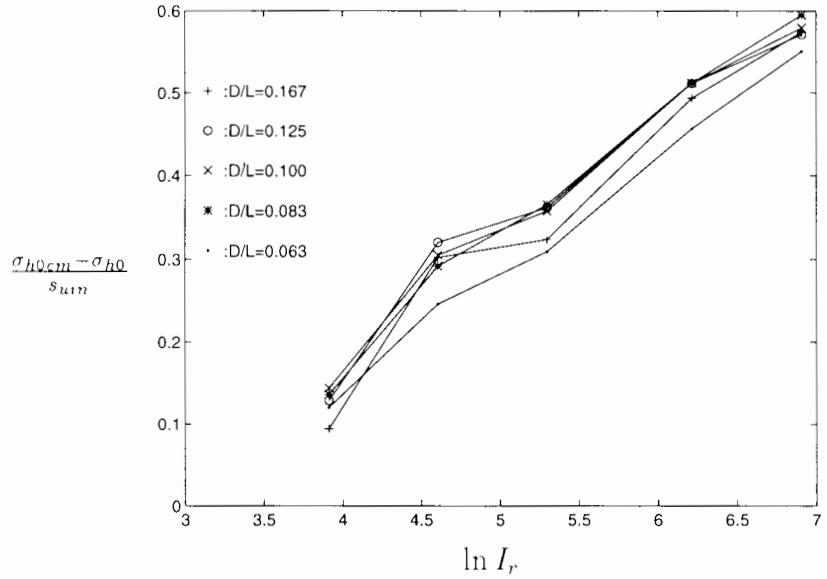


Figure 61: The effects of the input rigidity index on the calculated initial horizontal stress

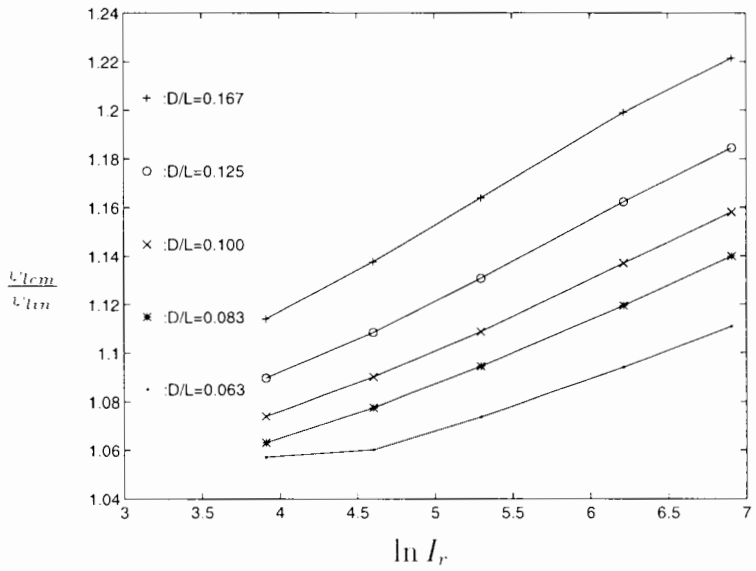


Figure 62: The effects of the input rigidity index on the calculated limit pressure

with a small deviation about 0.05, it cannot be said that the effect of the length-to-diameter ratio on the initial horizontal stress is small, since the value 0.05 should be compared with the overestimation value. However, it is said that the effects of the length-to-diameter ratio is small in comparison with the effects of the rigidity index.

3.5.5 Limit pressure

Figure 62 shows the effects of the rigidity index on the limit pressure. As seen in the figure, it can be said that there is a significant effect of the rigidity index on the limit pressure. The limit pressure increases proportionally with the logarithmic of the rigidity index. It is interesting that the lines seems parallel. This means that the effects of the length-to-diameter ratio are constant when the D/L is the same value and the effects of the rigidity index are varied.

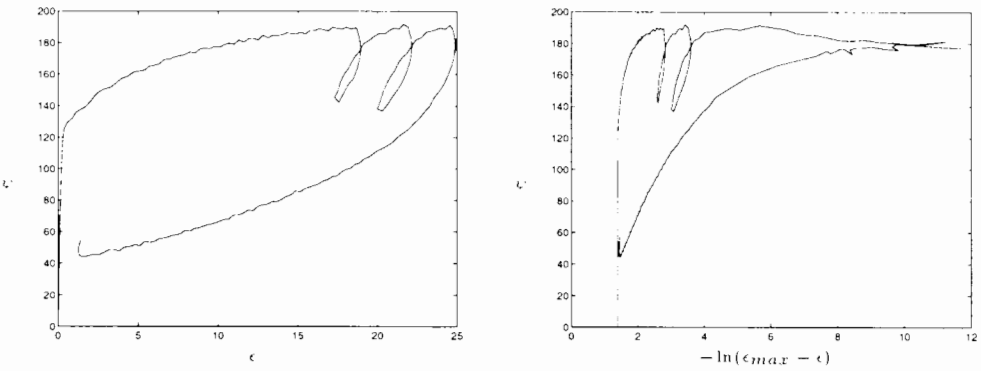


Figure 63: A typical pressuremeter curve from a field test b1, see Table 65

3.6 Application

This chapter explores an application of the finite element test results to in-situ tests. It is well-known that the initial horizontal stress measured by the cone-pressuremeter test are higher in comparison with other test results. Therefore, this chapter concentrate on the initial horizontal stress correction.

The in-situ test data performed by Powell and Shields, and Houlsby and Withers are analysed. 15 tests are from Madingley and 4 tests are from Bothkennar. The full-displacement pressuremeter used in the tests has a length-to-diameter ratio of 10.

The result of the calibration of the pressuremeter in air used to eliminate the influence of the pressure caused by the membrane on the pressuremeter tests as much as possible. It was found by Schnaid (1990) that a three parameter hyperbola of the form

$$\upsilon = K_1\epsilon\left(\frac{\upsilon_f + K_2\epsilon}{\upsilon_f + K_1\epsilon}\right) \tag{88}$$

provided a good fit to the air calibration data. The three parameters are obtained from the loading part and then the best offset is obtained for unloading part. Then, the pressuremeter results are obtained by subtracting the calibration curve from the original data.

A typical pressuremeter test result is seen Figure 63, which shows data from Bothkennar(test b1). There are several parameters measured from the result,

test name	depth(m)	s_u	υ_l	I_r	σ_{h0}
m1	4	97.9	791.0	269.0	190.6
m2	9	128.5	1000.8	199.8	230.1
m3	14	171.9	1461.5	283.4	365.1
m4	6.5	121.0	936.4	222.1	205.8
m5	9	125.3	921.5	191.5	235.5
m6	11.5	166.6	1271.4	220.0	315.5
m7	14	159.6	1277.6	211.6	385.5
m8	16.5	208.6	1510.2	166.0	345.2

Table 19: Test results at Madingley by Powell and Shields

test name	depth(m)	s_u	I_r	σ_{h0}
m9	4	80	410	369
m10	9	150	223	465
m11	14	184	374	461
m12	18	179	255	739
m13	4	111	133	239
m14	14	192	255	641
m15	4	89	136	164

Table 20: Test results at Madingley by Houlsby and Withers

using Houlsby and Withers method. There are the undrained shear strength(s_u), limit pressure(υ_l), rigidity index(I_r), and the y-intercept(y_{int}) of the line found in the Houlsby and Withers analyses. Then, in practice, horizontal stress (σ_{h0}) is calculated by adding the limit pressure and the y-intercept and dividing the sum by 2. The limit pressure is defined as the maximum pressure found in the test. Therefore, it is not necessary that the maximum pressure occurred at the maximum strain. All the in-situ test results are summarized in Table 19, 20 and 21. Table 19 shows the data from in-situ tests performed by Powell and Shields in Madingley. Table 20 shows the data from in-situ tests performed by Houlsby and Withers in Madingley. In Table 20, limit pressure is not included, because there is no data for it. (However, it is possible to predict limit pressure using $\upsilon_l = \sigma_{h0} + s_u(1 + \ln I_r)$) Table 21 shows the data from in-situ tests performed by Powell and Shields in Madingley.

The correction procedure begins with the measured I_r value. So, the first corrected value is the apparent measured I_r value and measured value is the measured

test name	depth(m)	s_u	v_l	I_r	σ_{h0}
b1	4	19.2	191.8	59.9	94.0
b2	6	24.5	246.8	46.8	128.3
b3	12	37.3	424.5	59.7	234.6
b4	15	42.8	522.7	56.8	306.9

Table 21: Test results at Bothkennar by Powell and Shields

I_r value. Much attention should be paid to use this value, because the finite element analysis is normalized by the triaxial compression undrained shear strength. Since the I_r value is based on the undrained shear strength for plane strain, it is necessary to multiply the I_r value by $\frac{2}{\sqrt{3}}$. Then, the I_r value based on the triaxial compression undrained strain is obtained. Using the first corrected I_r value, get a factor from Table 18. Then, divide the measured I_r value by the factor and then get the second corrected I_r value. From this second corrected value, obtain a factor again. Calculate second corrected I_r value using this factor. Repeat the whole procedure for several times and if the difference between the n-th and n+1 th corrected value is sufficiently small, define it as a final corrected value.

Taking the data of test m1 as an example, The measured I_r value is 269.0. As it should be changed to the value based on the triaxial compression shear strength, multiply $\frac{2}{\sqrt{3}}$. Then, the I_r value is 311.3. Therefore, the first corrected value is 311.3. Seek a factor using the first corrected I_r value. It is found that the measured I_r value is underestimated by about 11%, therefore, the first measured I_r value is divide by 0.89. As a result, the second corrected value, 349.8 is obtained. From this second corrected I_r value, seek a factor. A value of 12% underestimation is taken. Therefore, the second corrected I_r value is a value of the measured I_r divided by 0.88. As a result, the second corrected value 353 is obtained. The seek a factor again and the factor is 0.88. Then, the final corrected value is 353. (The I_r value based on the shear strength for plane strain is 290.3.)

Then, from this value, the shear strength is overestimated by 7.5%. Hence, the true shear strength value, 91.0, is obtained. One is to use the measured σ_{h0} value. The measured σ_{h0} value is 190.3 and this is thought to be overestimated by $0.46 s_{uin}$. Therefore, the true value σ_{h0c} may be 148 (kPa).

The corrected value is seen in Table 22 and 23.

test name	s_u	I_r	σ_{h0c}
m1	91.0	290.3	148.4
m2	128.4	241.9	189.2
m3	158.5	340.0	304.3
m4	110.1	258.2	165.3
m5	115.8	227.8	195.5
m6	153.0	249.5	268.4
m7	148.5	254.4	365.8
m8	193.2	189.3	275.8
m9	76.5	480.1	337.2
m10	170.4	268.4	412.4
m11	171.2	442.1	387.2
m12	165.7	302.3	674.3
m13	105.5	158.3	210.7
m14	177.7	320.3	576.3
m15	147.2	96.7	124.1

Table 22: Corrected values of test results at Madingley

Figure 64 and 65 shows the comparison between corrected values, measured values and the best estimate value of initial horizontal stress for both cases.

In Figure 64, when paying attention on the data by Powell and Shields, the measured value itself is slightly lower than the best estimate value quoted by Powell and Shields, and the corrected value is lower than the measured value. The correction seems small. When paying attention on the data by Houlsby and Withers, the measured value itself is higher than the best estimate value and the corrected measured value is nearer to the best estimate value than the measured value. However, still, the difference between them is large. In Figure 65, it is found that the correction itself is small with the result that the corrected value is almost same as the measured value. It is found that the correction does not fully explain the observed initial horizontal stress values, although the direction of the correction is correct.

As mentioned in Chapter 1, there is a consensus that the measured initial horizontal stress is overestimated in comparison with other test results. If taking the Powell and Shields data as an exception, it can be said that the direction of the correction is right, but the correction is still not enough to explain the difference. This means that the length-to-diameter ratio effect on the initial horizontal stress is not large enough to explain the overestimation of the initial horizontal stress.

test name	s_u	I_r	σ_{h0c}
b1	17.4	68.3	90.2
b2	21.3	56.6	123.7
b3	33.8	67.4	227.6
b4	38.6	66.0	299.1

Table 23: Corrected values of test results at Bothkennar

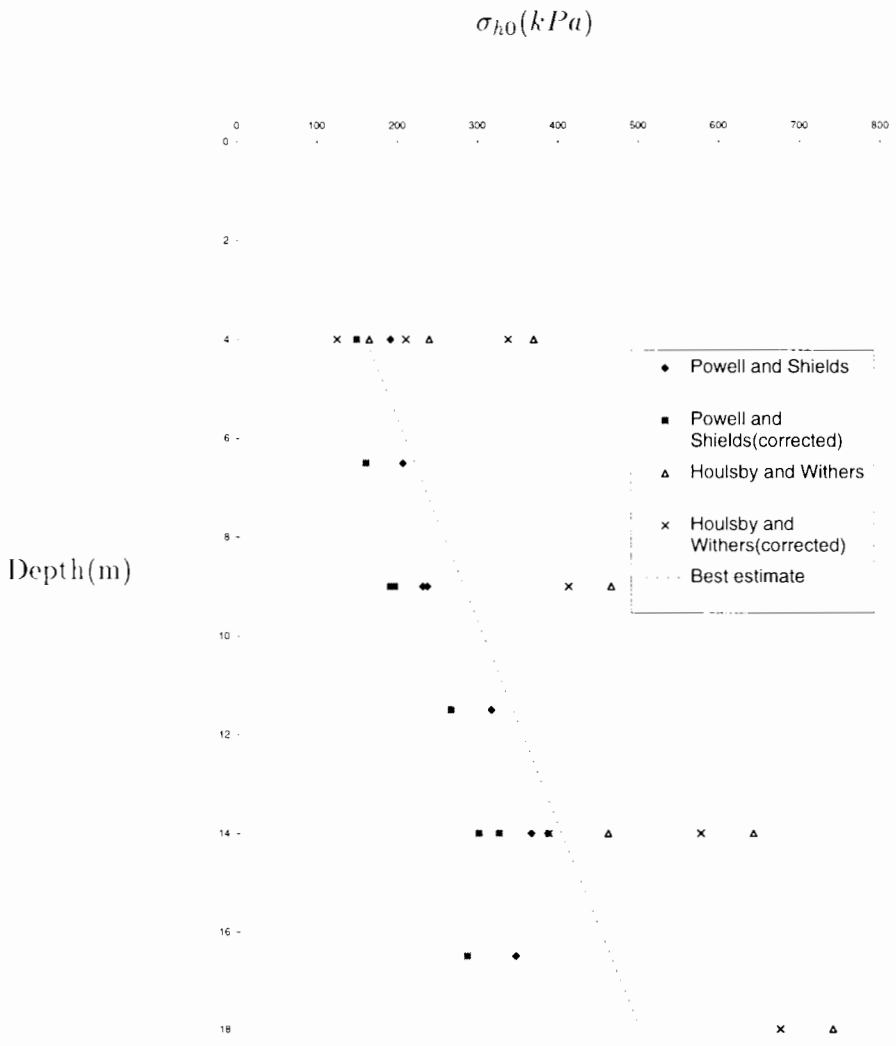


Figure 64: Results of the correction of Madingley results (best estimate as made by Powell and Shields)

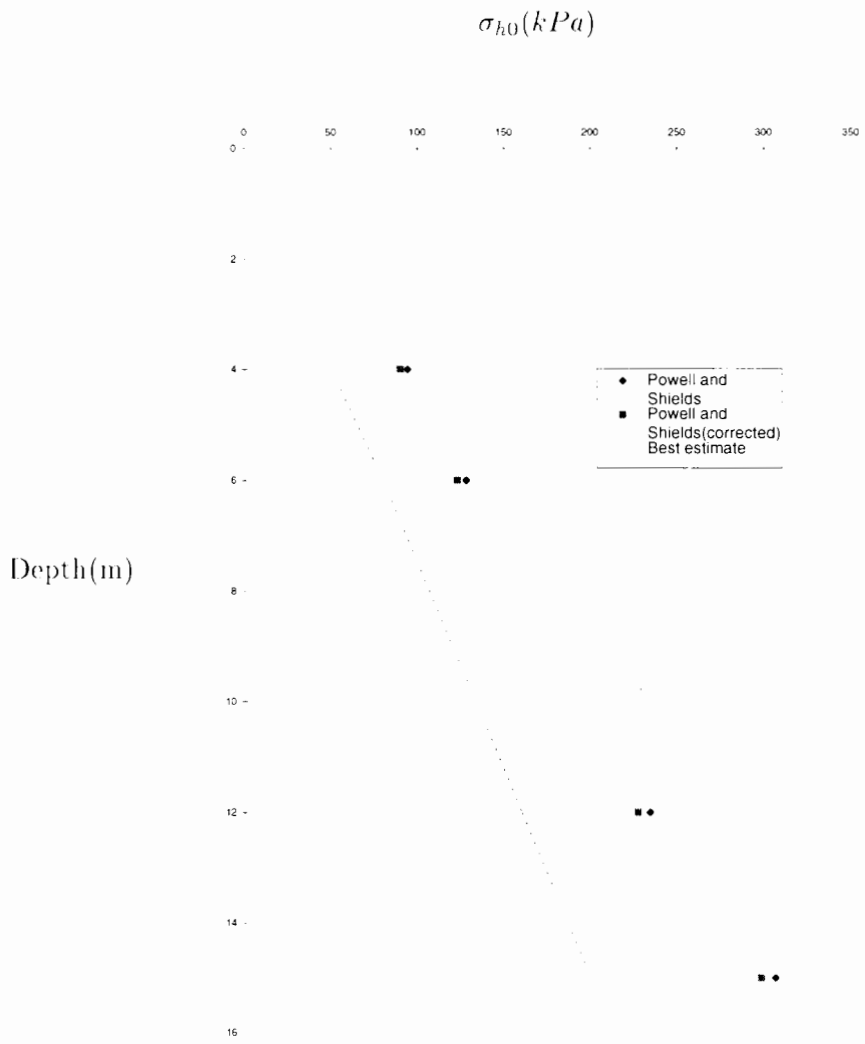


Figure 65: Results of the correction of Bothkennar results (best estimate as made by Powell and Shields)

3.7 Final remark

This chapter investigates the full-displacement analyses using finite element method. In in-situ tests, measuring the initial horizontal stress correctly is one of the most difficult task. Therefore, this chapter especially pays much attention to the effects of the length-to-diameter ratio on the initial horizontal stress using the Houlsby and Withers analysis.

It is found that the shear strength is overestimated and the rigidity index is underestimated because of finite length of a pressuremeter. Both of them depends highly on the rigidity index. As a result, there seems less significant effects of finite length of a pressuremeter on the shear modulus. The initial horizontal stress is overestimated as well, however, it dose not seem to be influenced by rigidity index.

The correction method is applied to the in-situ tests performed by Powell and Shields. The results show that the correction does not work. However, if taking into the fact that the initial horizontal stress is normally overestimated, the direction of the correction is right.

Chapter 4

Experimental apparatus and sample preparation

4.1 Introduction

Some calibration chamber tests were carried out to investigate the length-to-diameter ratio on the cone-pressuremeter tests in sand. Since the pressuremeter used in the tests is a 5 cm^2 device, it is not sufficiently strong to be pushed into a dense or highly stressed sample. In preliminary testing the pressuremeter buckled when being pushed into a dense stressed sample. It was therefore decided that the sample pressurization would follow after the installation of the pressuremeter. This differs from realistic installation in-situ. However, the effects of this procedure may be thought to be small, since the soil around pressuremeter should be deforming plastically just after the installation. The cone tip resistance was not measured. However, it is still possible to study the length-to-diameter effects on the deduced strength and stiffness of soil.

4.2 Experimental apparatus

4.2.1 The cone-pressuremeter

All the tests carried out in the sand calibration chamber reported in this thesis used a 5 cm^2 cone pressuremeter. This device was designed and constructed by Cambridge In-situ to specifications prepared by Oxford University and Fugro-McClelland. The cone-pressuremeter consists of two measuring instruments: a standard 60 degree cone-penetrometer, which is used to measure tip cone resistance, and the pressuremeter module. The latter is provided with various adapters enabling it to be assembled with length to diameter ratios of, approximately, 5, 10 and 20. It is inflated by silicone oil and the resulting pressure expansion curve used to measure the soil stiffness and strength. Due to limitations in diameter, the instrument has no strain gauged arms (as are usually used in larger pressuremeters), with the result that membrane expansion is only measured by the change of volume of the pressuremeter probe. The detail of the design of the pressuremeter is shown in Figure 66.

The membrane is fixed to the pressuremeter with two threaded clamping rings. Much attention is be paid to fixing the membrane, because it is easily damaged by the clamping ring when it is being tightened. It was discovered during the tests that at high pressures and at large strains, the membrane can inflate in between the ring and the Chinese lantern, so that the membrane can be damaged causing it to burst. In order to avoid these problem, some tape is wrapped around the end of the membrane to prevent the membrane from being damaged by the clamping ring. The junction between the clamping ring and membrane are further wrapped to prevent the membrane from inflating in the way described above.

The pressuremeter membrane is covered with stainless steel strips (the Chinese lantern), which prevent the membrane from being damaged by the sand, and also help the membrane to inflate even. In Schnaid's tests (1990), a Chinese lantern for a long pressuremeter ($L/D = 20$) is used even for a medium ($L/D = 10$) and small ($L/D = 5$) pressuremeter. This may alter the end effects, therefore, Chinese lanterns for a medium pressuremeter and a small pressuremeter were prepared to investigate the length to diameter ratio. In addition, this cone pressuremeter has

so small across sectional area that it is just impossible to push it into a dense sand sample or highly stressed sample without damage.

4.2.2 The Oxford sand calibration chamber

In order to investigate the behaviour of the cone-pressuremeter in sand, a calibration chamber is used in which sand density and in-situ stresses can be controlled directly. The size of the chamber used in the tests is 1.0m in diameter and 1.5 m in height, corresponding to a volume around 1.2m^3. Pressure can be applied both horizontally and vertically. Details of the chamber are presented in Figure 67.

This triaxial calibration chamber was designed as a new version of that used at Cambridge University (Fahey,1980) and later re-assembled at Oxford University (Houlsby and Hitchman,1988). The sample can be pressurized laterally by a flexible rubber membrane filled with water. The top of the sample is confined by a rigid plate, so that the sample can be pressurized vertically by applying water pressure at the bottom bag.

A problem during tests is leakage of water at the end of the membrane. A simple method is used to avoid these leaks. Each membrane was fixed between two metal faces, by means of circular clamping rings as seen in Figure 67, and small amount of silicon rubber was daubed between the rubber and the metal before clamping, with the results that there were hardly any leaks during tests.

The horizontal pressure and vertical pressure are controlled by identical pressurization systems.The change in pressure is produced by regulating air pressure using a self-relieving valve and air-water interface system. The interface allows water to be used to apply stresses to the sand sample and stabilizes pressure fluctuation due to variations in volume experienced by the sample during test.

4.2.3 The driving rig

A driving rig capable of providing sufficient thrust (up to 100kN) for insertion of a range of in-situ devices, is attached to the rigid top plate of the calibration chamber. The whole mechanism of the driving rig is seen in Figure 68. This rig provides a linear speed of 20mm/s, with a tolerance of $\pm$ 5mm/s. A load

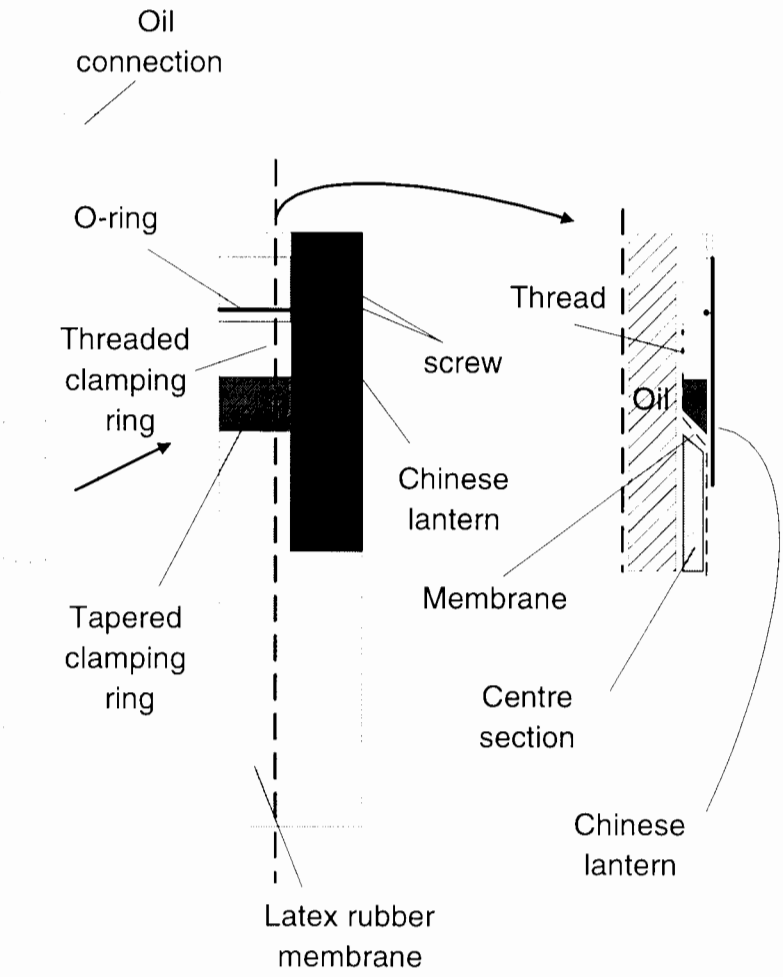


Figure 66: The mechanism for the pressuremeter pressurization

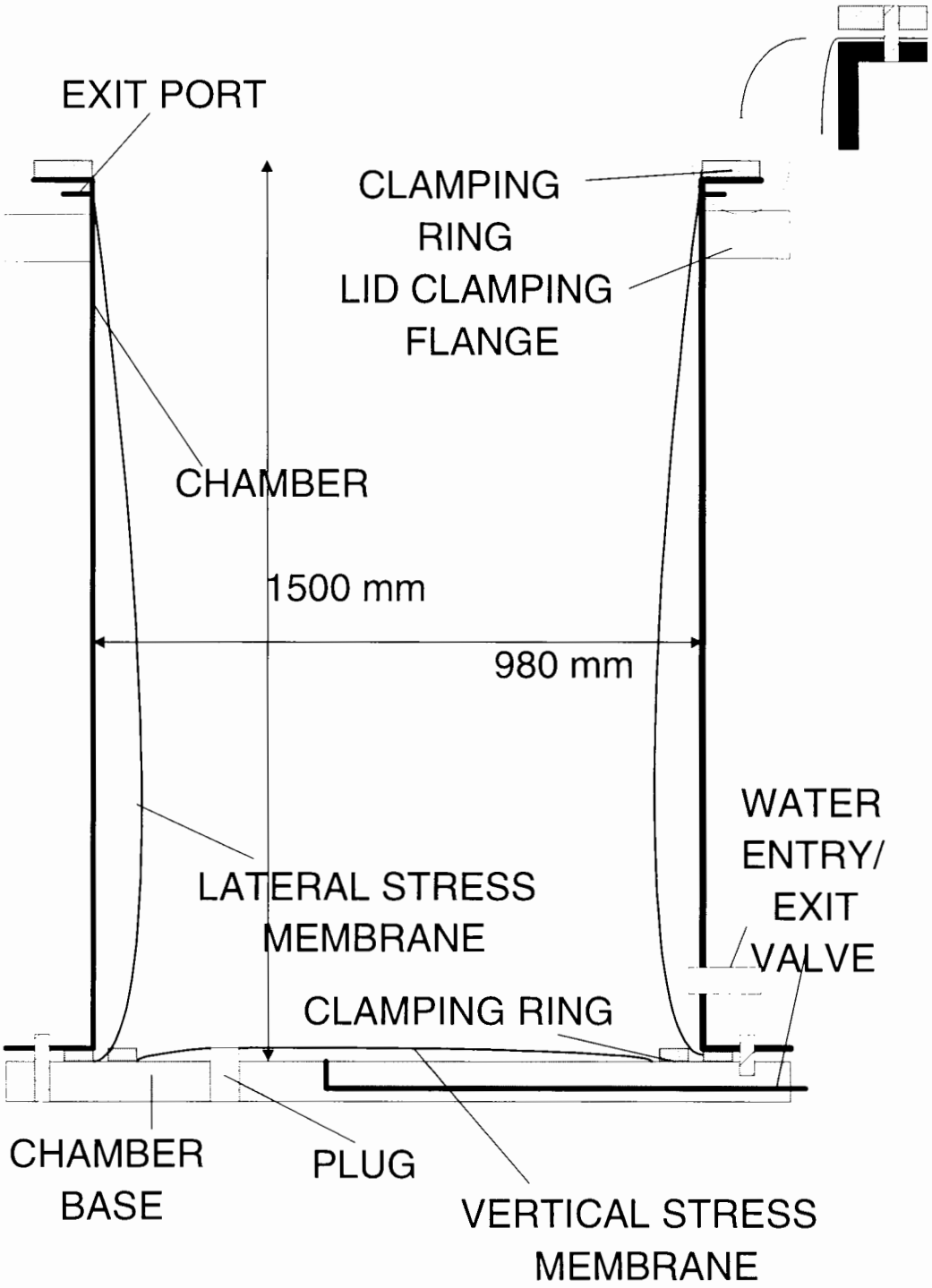


Figure 67: The Oxford calibration chamber

transmission plate is driven by a ball screw mechanically connected to a geared 3 kW DC motor.

4.2.4 The hopper and sieve

In order to rain the sand uniformly, a large hopper, capable of holding the complete amount of sand necessary for sample preparation was used. The hopper consists of two cylinder which are connected to each other. One of them is 1580mm in diameter and 300mm in height. The other is 1000mm in diameter and 1100mm in height. The structure of the hopper can be seen in Figure 69. The hopper has holes located on a 80mm triangular grid at the bottom, the size of which is 20mm in diameter. These holes can be closed and opened by shifting a steel plate described below. There are two kinds of steel plates, one for making a dense sample and the other for making a medium or loose sample. Both of them have holes. One of them with holes of 6mm diameter on a 80mm triangular grid, is for dense sand sample. The other with holes of 20mm diameter on a 80mm triangular grid, is for loose and medium dense sand sample.

Each of this plates can be attached to the bottom of the hopper. Therefore, the sand in the hopper can come through the hole when the holes in steel plate and the holes in the hopper are overlapped. In the tests, only medium sands are used because of the pressuremeter strength.

In making a medium or dense sample, it is necessary to use a sieve, which is attached to the bottom of the hopper, since the density of the sample highly depends on the speed of the sand raining. Therefore, a sieve was made to prepare a medium or dense sand sample. The sieve consists of two wire meshes, the mesh of which is 5mm. The structure of the sieve can be seen in Figure 70. This sieve is set to the bottom of the hopper.

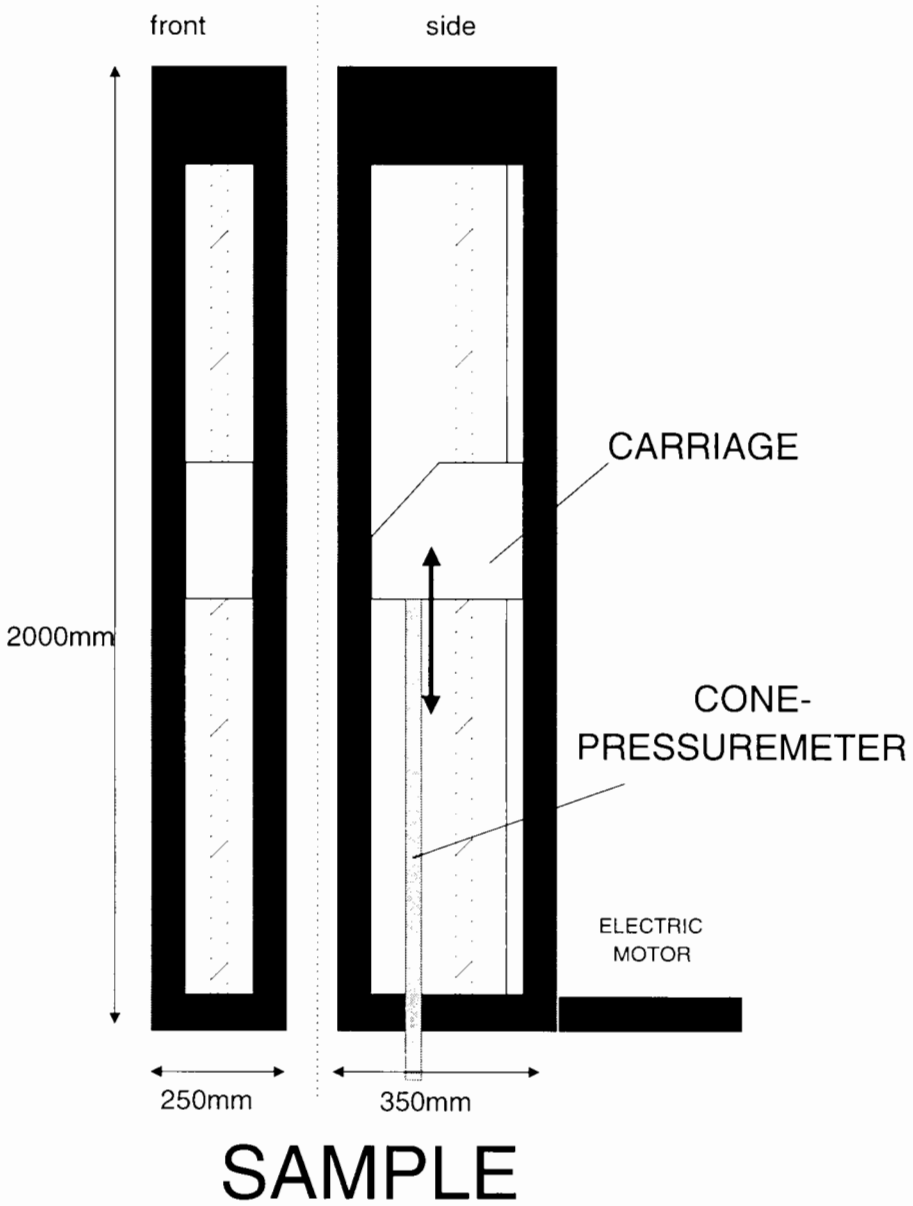


Figure 68: The mechanism of the driving rig

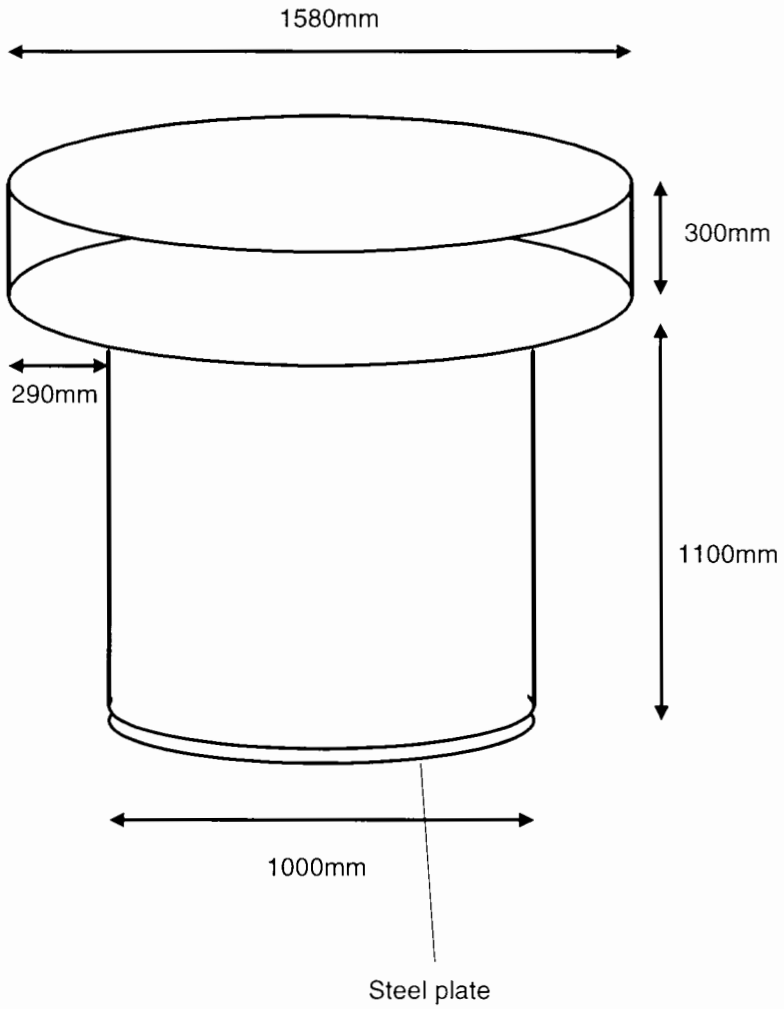


Figure 69: The hopper

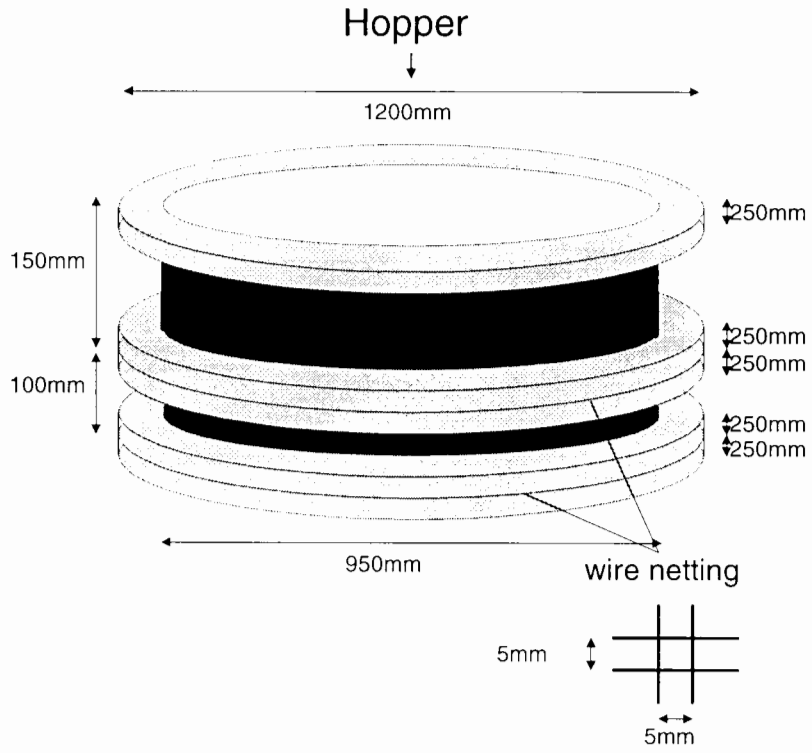


Figure 70: The sieve

4.3 The pressurization system for the pressuremeter

A pressurization system for the pressuremeter was designed and constructed at Oxford University to control tests in the laboratory. The $5cm^2$ cone-pressuremeter is inflated by means of silicon oil in order to monitor the volume change of the expanding membrane. The mechanism is illustrated in Figure 71. A piston is driven inside an oil cylinder to inject oil into the pressuremeter. It is mechanically connected to a geared DC motor. The maximum speed of this piston is 2 mm/s and the displacement is measured by a Calvin position transducer, type PT101-30 with a tensioned cable, powered by a 5V DC supply. The displacement of the piston is used to calculate the volume change of the pressuremeter and hence the pressuremeter strain.

In the setting up of the pressuremeter, some vacuum is applied at the top of the oil tank to remove all the air inside the pressuremeter and the tank, because air can be compressed and it would effect the volumetric strain calculation. Then, a large pressure is applied to the pressuremeter in order to let air come out. This process is repeated several times, especially at the end of the calibration test to check whether or not there is air inside the pressuremeter system. In fact, during the tests no air was found in the system, which indicates the high accuracy of the pressuremeter monitoring system.

A pressure transducer, type P102 is used to monitor the pressure. The capacity of it is 10MPa. This is connected to the oil cylinder, to which a pressuremeter is also connected. In each test, the pressure and volume change of the pressuremeter are logged through a data-logging system attached to an IBM PC.

4.4 Procedure of the test

The testing procedure is as follows:

1. Seal the steel plug in the base of chamber. (This can be removed after testing to allow the sand to be poured back into the hopper.)

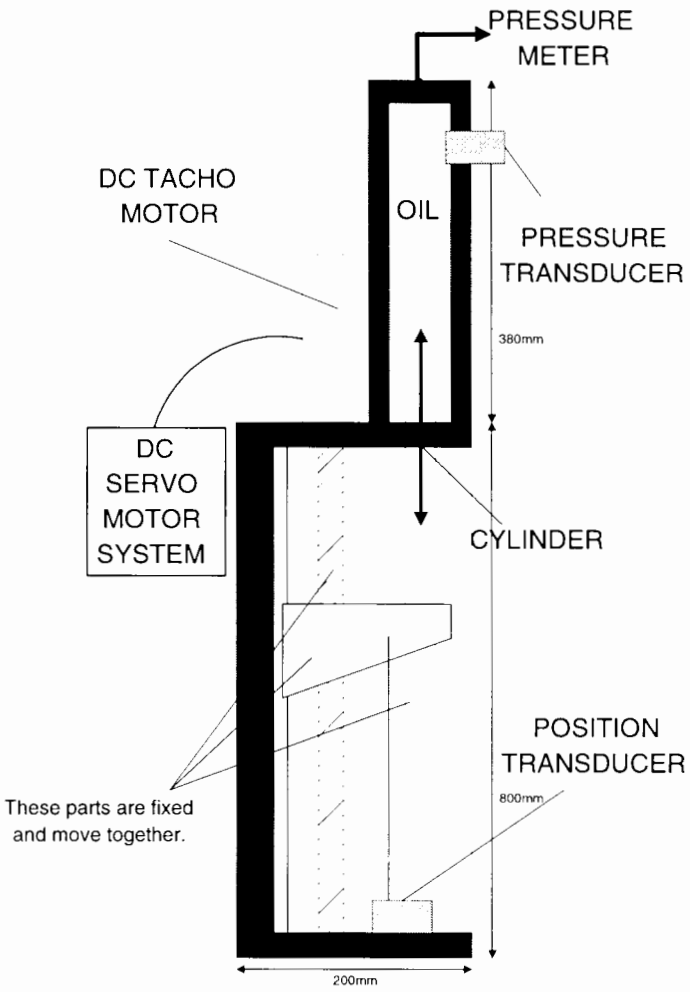


Figure 71: The mechanism for the pressuremeter pressurization

2. Apply a vacuum of about 10kPa to the lateral membrane to suck it firmly against the side wall of the chamber.

3. Place cylindrical steel former in chamber, taking care not to damage the lateral membrane, especially near the bottom of the edge, and put some water in base membrane of chamber up to the height of the plug in order to make the bottom of the sample as horizontal as possible.

4. Place the inner membrane inside the former, sealing the hole in the membrane, which is later to be connected to the plug in the base of the chamber, and wrapping the top over the steel former.

5. Hang the hopper (together with the steel plates and sieves) above the chamber and enclose the gap between the hopper and chamber by a rubber membrane to reduce dust.

6. Open the shutter plates to allow sand to flow into the chamber.

7. Level the surface of the sample to measure the height of the sample. (The surface of the sample should be near the top of the chamber, within 15mm below.) Seal sample, apply vacuum

8. Remove the steel former upward with a vacuum pressure of 4kPa to 5kPa applied to the sample. When the steel former is removed, the sample should stand by itself, to the extent that whole of the sample can be moved by pushing it gently. If this condition is not satisfied, it indicates that the bottom of the sample is collapsed, therefore, the sample should not be used for testing.

9. Fill the annular space behind the lateral membrane with water so that the sample can stand by itself without a vacuum pressure. The vacuum is released and the boundary of the cylindrical sample becomes water supported. It is important to observe the height of the sample to check the sample is still good enough or not.

10. Lower the top plate and fix it to the chamber body. Install pressuremeter. Because the 5 cm^2 is not sufficiently strong to be pushed into a highly stressed

sample or dense sample, the pressuremeter is installed before pressurizing the sample. (The cone tip resistance is not therefore measured.)

11. Open the chamber valves and control the self relieving valves on the pressurization panel to stress the sample following any pre-selected $K_0 = \sigma_{h0}/\sigma_{v0}$ path both horizontally and vertically. A strain controlled pressuremeter test is then carried out at constant vertical and horizontal stresses.

12. Drain the side and bottom membrane as much as possible, and then measure the weight of the chamber with sand and the sand bag. The plug of the bottom and side membrane should be closed after draining.

13. Empty the chamber by opening the plug on base of chamber and then measure the weight of the chamber with a sand bag. Finally, the weight of the sand is obtained.

As is mentioned above, the pressuremeter is installed before pressurizing the sample. This is not ideal, however, the difference between installation before pressurizing the sample and after is thought to be small, since the volume of soil disturbed by the pressuremeter should be the same in both cases.

4.5 Data acquisition and calibration

In in-situ tests, a cone pressuremeter is used to measure both the cone tip resistance and the pressure-strain relationship. However, as is mentioned before, the 5 cm^2 pressuremeter itself is easily damaged on installation by a dense or highly pressurized sample with the result that the installation is performed before pressurizing and the cone tip recording is not performed at all in the tests.

Therefore, the data acquisition system for a pressuremeter test is just explained in this section. The pressure of the pressuremeter is recorded by a pressure transducer and this can be monitored by a logging system attached to IBM PC. The results of the calibration of the transducer against a DPI is shown in Figure 73 and Table 24.

The strain is calculated from the change of the volume of the pressuremeter assuming that the strain is a half value of the ratio of the volume change to initial

Instrument	Calibration (/Volt)	R^2	Calibrated against
Position transducer	208.35(mm)	0.9999	Steel ruler
Pressure transducer	19889.8(kPa)	0.9999	a DPI

Table 24: Results of calibration

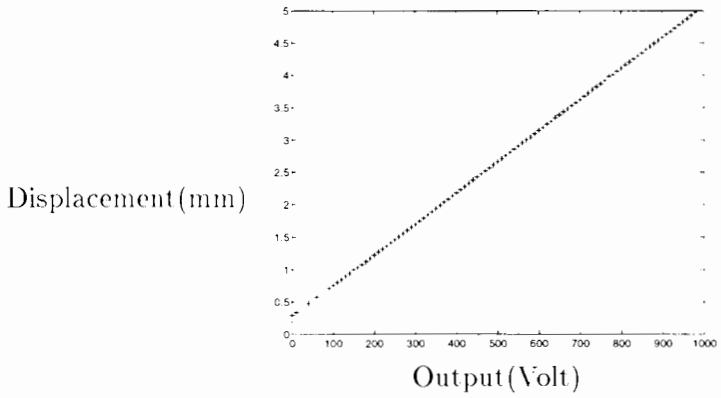


Figure 72: Calibration result of displacement transducer

volume. and this volume change is calculated from the displacement of the piston. which is monitored by a position transducer. The calibration of this transducer against steel ruler is shown in Figure 72 and Table 24.

As seen in Figure 72 and Table 24. the data derived from these transducers are very accurate as the calibration are highly linear.

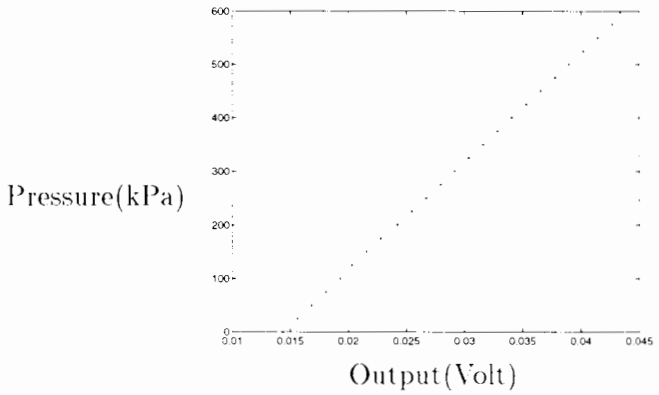


Figure 73: Calibration result of pressuremeter transducer

Chapter 5

Experimental results

5.1 Introduction

The cone-pressuremeter is a device which can measure the cone tip resistance and obtain a pressure expansion curve. However, the length-to-diameter ratio has a significant effect on the pressuremeter expansion curve both for sand and clay. This chapter explores the use of calibration chamber tests in sand to examine the L/D effects.

A total of seven calibration chamber tests using the cone-pressuremeter are analysed here. The material used in the tests is yellow Leighton Buzzard sand. The sand has a maximum voids ratio value of 0.79 and a minimum voids ratio value of 0.49, according to Pedley (1990).

In practice, the limit pressure found in the test is a key factor used to interpret the strength of sand. However, it was shown by Schnaid (1990) that the limit pressure obtained from the pressuremeter curve in sand is influenced by the length-to-diameter ratio. Therefore, this chapter focuses only on the effects of the length-to-diameter ratio on the limit pressure.

5.2 Calibration results

Since the pressuremeter test results are influenced by the stiffness of membrane itself, calibration needs to be done. A calibration in air is performed.

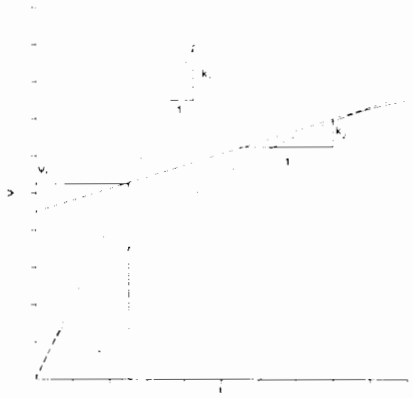


Figure 74: Three-parameter hyperbola

The result of the calibration of the pressuremeter in air used to eliminate the influence of the pressure caused by the membrane on the pressuremeter tests as much as possible. It was found by Schnaid (1990) that a three parameter hyperbola of the form

$$v = K_1\epsilon(\frac{v_f + K_2\epsilon}{v_f + K_1\epsilon}) \tag{89}$$

provided a good fit to the air calibration data, where the parameters K_1, K_2 and v_f are as shown in Figure 74. From the loading stage, the three parameters are obtained. An offset from this curve is used to obtain a which best fit the air calibration unloading curve. This assumes that the unloading curve is obtained by shifting the loading curve. A typical result of the pressuremeter calibration in air is shown in Figure 75.

5.3 Interpretation method

5.3.1 Data reduction and correction

1. Raw data in voltages is converted to engineering units using the input of relevant calibration factors. In the tests the hoop strain is calculated based on the volume change of the oil in the pressuremeter and the logarithmic strain is used:

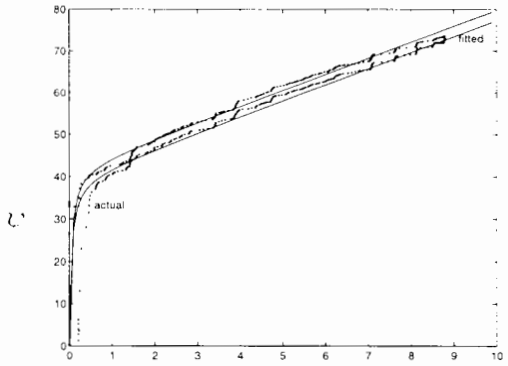


Figure 75: A typical result of membrane calibration

$$\epsilon = \ln(\frac{R}{R_0}) = \frac{1}{2}\ln(\frac{R^2}{R_0^2}) = \frac{1}{2}\frac{V}{V_0} \tag{90}$$

where V and V_0 are the current volume of the pressuremeter and the initial volume of the pressuremeter, and R and R_0 are the current radius and initial radius of the pressuremeter.

2. Subtract the best-fit air calibration curve from the pressuremeter test curve.

3. Measure the limit pressure, which is the maximum pressure in a test. In addition, since a value of limit pressure was not clearly observed when the length-to-diameter ratio of the pressuremeter is 5, the cavity pressure at a strain of 10% is used to compare the pressure expansion curves.

5.4 Experimental results

A total of seven tests were carried out. The test results are presented in Table 25. L/D means the length-to-diameter ratio of the pressuremeter. σ_h and σ_v are the horizontal stress and the vertical stress at the centre of the pressuremeter. K_0 is the coefficient of earth pressure. Since the short pressuremeter cannot reach a high strain range, 10% is chosen to compare the cavity pressure. $\sigma^{10\%}$ is pressure found

test name	L/D	$R_d(\%)$	$\sigma_v(kPa)$	$\sigma_h(kPa)$	K_0	$v^{10\%}$	v_l	$v_c^{10\%}$	v_{lc}
p1	5	32.8	98.8	100.4	1.0	1710	1835	1830	1963
p2	5	33.8	119.9	59.8	0.5	1382	1514	1448	1586
p3	5	29.9	71.6	152.4	2.1	1840	2005	2096	2283
p4	10	42.4	98.3	100.8	1.0	1510	1623	1339	1439
p5	10	36.7	147.6	76.7	0.5	750	875	740	863
p6	10	47.5	74.5	151.2	2.0	1694	1872	1387	1532
p7	20	32.8	98.8	100.4	1.0	953	1090	1016	1162

Table 25: Results of the experimental work

at the 10% of the strain. The limit pressure, v_l means the maximum pressure found in a test.

Although test p4 and p6 are denser than others, all tests are at almost same density. A possible reason for this is that the steel plate could not be fully opened because the friction between the steel plate and the hopper was large. Other reason is that the steel plate itself has been bent with the result that it was difficult to shift the steel plate. The pressure is well-controlled.

Figure 76, 77 and 78 shows the results for $K_0 = 0.5$, $K_0 = 1.0$ and $K_0 = 2.0$ respectively. In general, the results appear to be self-consistent in that comparisons between different tests give consistent trends. Note that the two tests at $K_0 = 0.5$ show a much stronger effect of L/D than the tests at $K_0 = 2.0$. The reason for this is not clear.

According to Nutt (1993), the relationship between the limit pressure v_l and the relative density R_d can be written:

$$\frac{v_l - \sigma_h}{\sigma'_h} = 1.98 + 19.1 R_d \tag{91}$$

where σ_h and σ'_h are horizontal stress and effective horizontal stress. (In this case, the tests are performed with dry sand, with the result that $\sigma'_h = \sigma_h$.) This equation is valid for Dogs Bay, Hokksund, and Leighton Buzzard sand (white), although the tests were performed with 10 cm^2 device.

Schnaid (1990) showed that the relationship between $\frac{v_l - \sigma_h}{\sigma'_h}$ and the ratio of the chamber to probe diameter is almost linear when the density is the same.

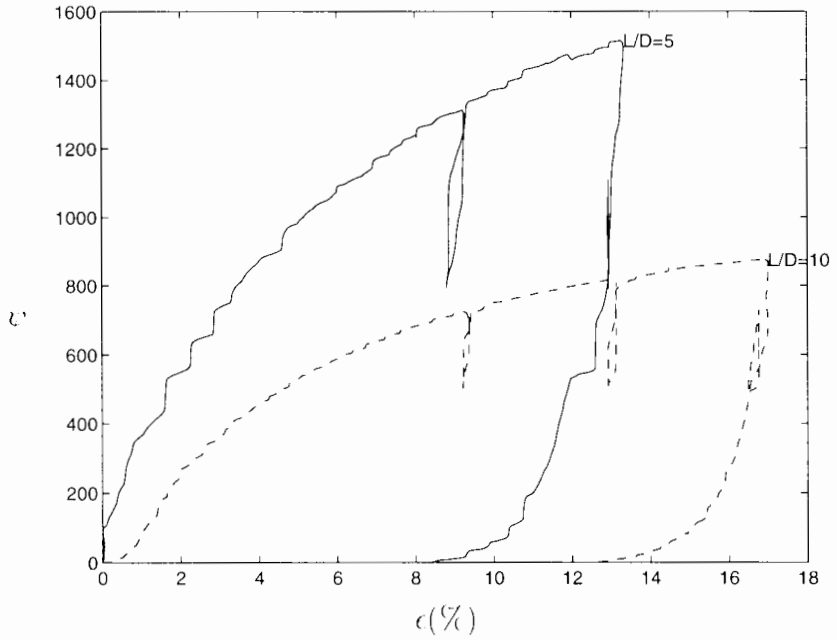


Figure 76: Experimental results for $K_0 = 0.5$

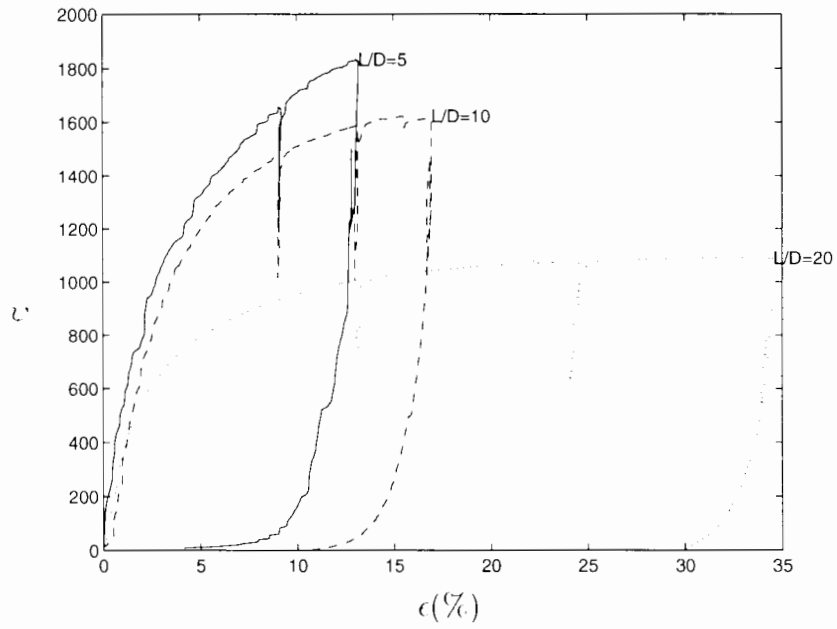


Figure 77: Experimental results for $K_0 = 1.0$

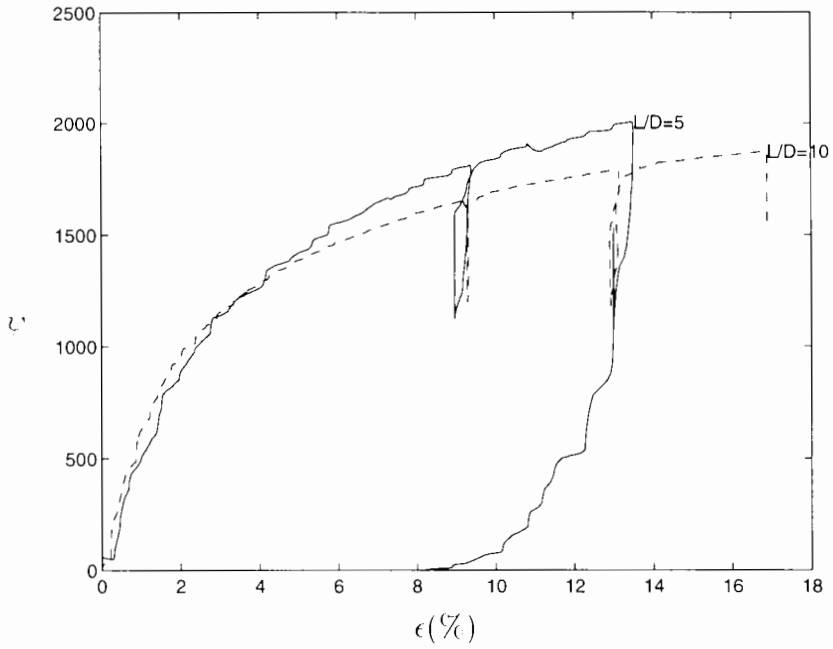


Figure 78: Experimental results for $K_0 = 2.0$

Therefore, equation 91 can be used to analyse 5cm^2 pressuremeter test results. In Schnaid's thesis (1990), corrections for variations of the density has not been done. Therefore, the results obtained by Schnaid (1993) are investigated again here. In the experiments performed by Schnaid, white Leighton Buzzard was used and the results of the medium density tests were chosen. It is known that there is no significant difference between white and yellow Leighton Buzzard sand at comparable densities except that the angle of friction is higher.

However, the density of Schnaid's tests are medium and there is no way to produce a linear equation like equation 91, which hold true for all of the test results. Hence, a factor, k, is used to obtain the relationship between $\frac{\upsilon_l - \sigma_h}{\sigma'_h}$ and R_d That is, $\frac{\upsilon_l - \sigma_h}{\sigma'_h}$ value for 5 cm^2 is obtained by multiplying $\frac{\upsilon_l - \sigma_h}{\sigma'_h}$ value for 5 cm^2 by k. This factor, k, is chosen according to Schnaid's thesis. (k varies just with the density.)

Therefore,

$$\frac{\upsilon_l - \sigma_h}{\sigma'_h} = k(1.98 + 19.1Rd) \tag{92}$$

test name	L/D	$Rd(\%)$	$\sigma_v(kPa)$	$\sigma_h(kPa)$	K_0	$\upsilon^{10\%}$	υ_l	$\upsilon_c^{10\%}$	υ_{lc}
s1	5	67	138.1	71.6	0.5	1819	1940	1752	1868
s2	5	63	88.8	96.6	1.1	2046	2200	2072	2227
s3	10	64	138.7	71.6	0.5	1320	1460	1320	1460
s4	10	65	88.8	96.6	1.1	1727	2050	1706	2025
s5	20	61	138.1	71.6	0.5	1077	1140	1119	1184
s6	20	62	88.8	96.6	1.1	1431	1490	1468	1528

Table 26: Results of the experimental work by Schnaid(1990)

is used to correct the density effects on the test results.

The tests done by Schnaid are corrected as $R_d = 64\%$ and the tests done by Yao are corrected as $R_d = 36.6\%$. Both density value are the average values for each group of test results. When the aiming density value is R_{da}, the corrected value, υ_c, is obtained as follows:

$$\frac{\upsilon_c - \sigma_h}{\upsilon_l - \sigma_h} = \frac{1.98 + 19.1R_{da}}{1.98 + 19.1R_d} \tag{93}$$

The υ_l and $\upsilon^{10\%}$ values are corrected on the assumption that equation 91 is valid for υ_l and $\upsilon^{10\%}$ and for yellow Leighton Buzzard sand. Defining these corrected values as υ_{lc} and $\upsilon_c^{10\%}$, all results are summarized in Table 25 and 26.

First of all, $\frac{\upsilon_l - \sigma_h}{\sigma'_h}$ is plotted against the relative density. As seen in Figure 79, there is a trend that when the length-to-diameter ratio decreases, the value of $\frac{\upsilon_l - \sigma_h}{\sigma'_h}$ increases.

Second, $\frac{\upsilon^{10\%} - \sigma_h}{\sigma'_h}$ is plotted against the relative density. As seen in Figure 80, the value of $\frac{\upsilon^{10\%} - \sigma_h}{\sigma'_h}$ is high when the length-to-diameter is equal to 5. However, when the length-to-diameter ratio is equal to 10 or 20, the length-to-diameter ratio does not seem to have a significant effect.

Third, $\frac{\upsilon_{lc} - \sigma_h}{\sigma'_h}$ is plotted against D/L ratio (Figure 81). The data of loose sand sample is from Yao and that of medium is from Schnaid. There is a trend that the value of $\frac{\upsilon_{lc} - \sigma_h}{\sigma'_h}$ decreases when the length-to-diameter ratio increases.

Figure 82 shows the graph where $\frac{\upsilon_c^{10\%} - \sigma_h}{\sigma'_h}$ is plotted against D/L ratio. It can be said that the value of $\frac{\upsilon_c^{10\%} - \sigma_h}{\sigma'_h}$ decrease when the length-to-diameter ratio increase.

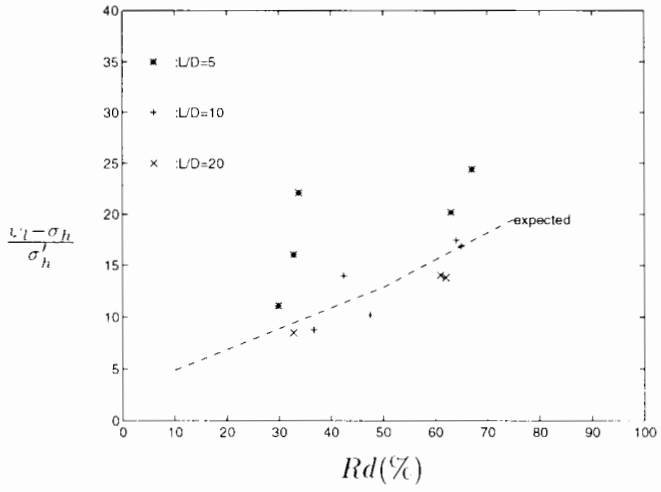


Figure 79: Density effects on the limit pressure

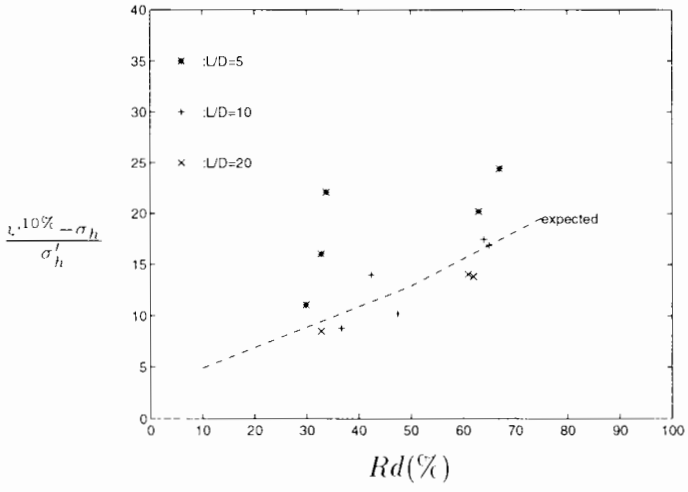


Figure 80: Density effects on the limit pressure(10%)

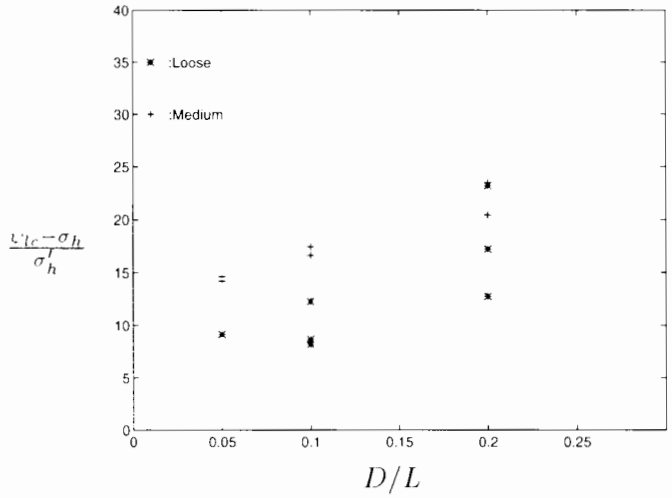


Figure 81: Length-to-diameter effects on the limit pressure

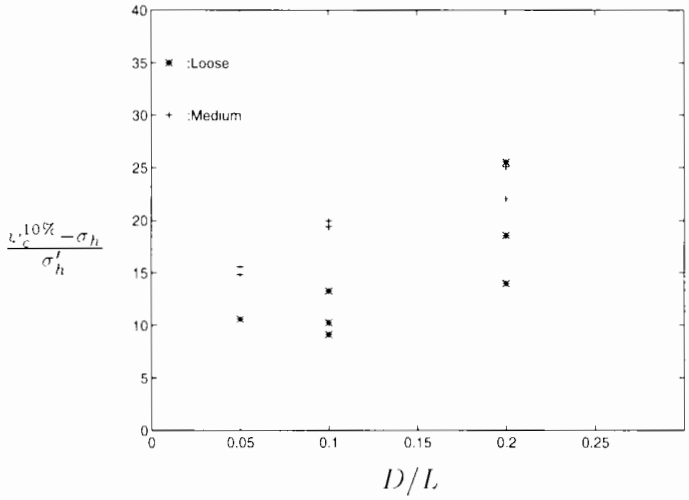
In addition, the value of $\frac{q_c^{10\%} - \sigma_h}{\sigma'_h}$ increase almost linearly with the D/L ratio and it seems that the slope of the medium sample data is less than the slope of the loose sample data. This means that the effects of the length-to-diameter is slightly effected by density, or to be more accurate, friction angle.

It is difficult to see the length-to-diameter ratio effects directly from Figure 81 and 82. Hence, the average of the same length-to-pressuremeter ratio pressuremeter data is is taken and then divided by the data for $L/D = 10$. From Figure 81 and 82, the value described above is derived and plotted in Figure 83 and 84 respectively. As seen in Figure 83 and 84, the effects of the length-to-diameter is slightly larger when the sand sample is loose than when the sand sample is dense. In addition, when the length-to-diameter ratio is 5, the normalized value is highly overestimated.

5.5 Final remark

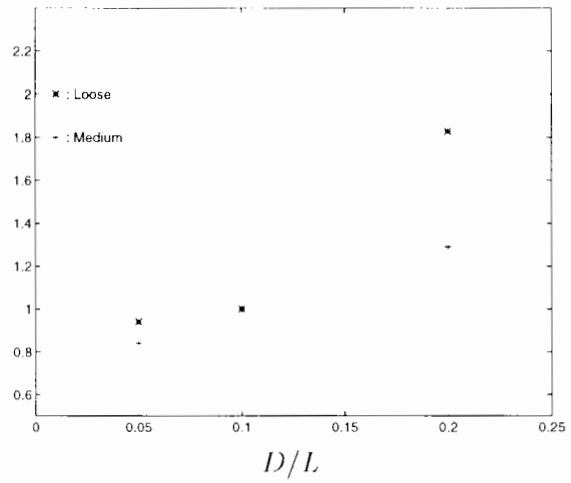
Although relatively few tests have been carried out, the effects of the length-to-diameter ratio on the limit pressure using the cone-pressuremeter for sand have been examined.

There is a consensus (e.g. Laier *et al.* (1975)) that the length-to-diameter ratio



$\frac{\sigma_c^{10\%} - \sigma_h}{\sigma_h'}$

Figure 82: Length-to-diameter effects on the limit pressure(10%)



$$\frac{\frac{\sigma_{lc} - \sigma_h}{\sigma_h'}}{\left(\frac{\sigma_{lc} - \sigma_h}{\sigma_h'}\right)_{L/D=10}}$$

Figure 83: Length-to-diameter effects on the limit pressure

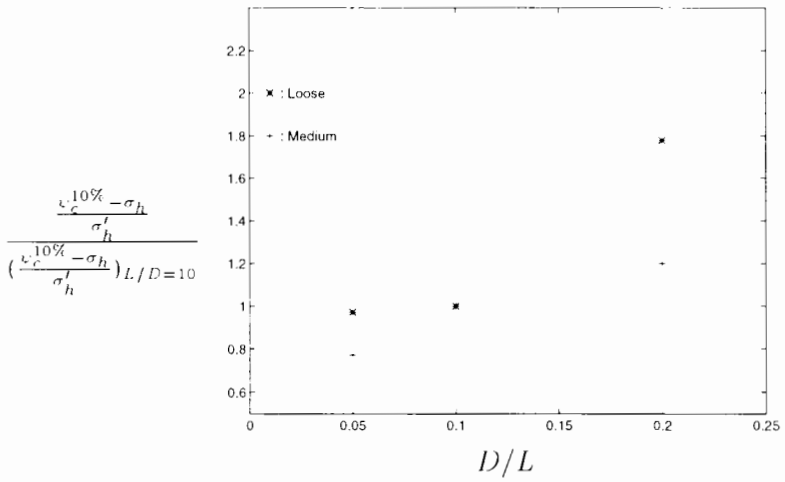


Figure 84: Length-to-diameter effects on the limit pressure(10%)

on the limit pressure does not influenced much by the density of the sand although it is found from experimental results that the effects of the length-to-diameter ratio is slightly more significant in loose sand than in dense sand.

However, the density of the sand sample varies and the effect of it is discernible. Moreover, tip cone resistance was not measured because of the capacity of the pressuremeter itself. Therefore, it is not possible to quantify the influence of the length-to-diameter ratio accurately, because there is a way to normalize the difference between the limit pressure and the horizontal stress by the difference between the horizontal stress and the cone tip resistance.

As far as the limit pressure is concerned, the influence of the length-to-diameter is significant. But the strain range for a short pressuremeter is limited with the result that the exact limit pressuremeter could not be examined.

Chapter 6

Conclusion

6.1 Introduction

Since cavity expansion theory, which is used to interpret the pressuremeter test, is based on simple boundary conditions which allow solution for stresses from simple differential equation, the pressuremeter is one of the most common *in-situ* testing devices to derive accurate soil parameters. However, in the cavity expansion theory, the length of the pressuremeter is assumed to be infinite, although the length of a real pressuremeter is of course finite. Therefore, this thesis concentrates on the effects of the length-to-diameter effects on pressuremeter tests.

The work has been divided into three topics. First, a numerical study of the self-boring pressuremeter both in sand and in clay is presented. Second, a numerical study of the full-displacement pressuremeter in clay is given. Third, an experimental study using the cone-pressuremeter in sand is given. The conclusions from each section are given below.

6.2 Self-boring pressuremeter

The advantage of the self-boring pressuremeter in comparison with the full-displacement pressuremeter is that the disturbance during the installation of the pressuremeter is rather small. In order to investigate the effects of the length-to-diameter ratio on pressuremeter test results, the analysis of a finite length self-boring pressuremeter is modelled as a two-dimensional axisymmetric problem, and large strain elastic perfectly-plastic analysis is used.

For the self-boring pressuremeter tests in clay, it was found that use of the conventional Gibson and Anderson method for investigating *in-situ* pressuremeter tests tends to overestimate the shear modulus and the undrained shear strength of clay because of the finite length of the pressuremeter. The numerical results suggest that the overestimation of the shear modulus does not depend on the rigidity index. In addition, the overestimation depends highly on which strain is used, central hoop strain or volumetric hoop strain. The overestimation found when using the central strain has no significance; on the other hand, the overestimation found when using the volumetric strain is discernible. The overestimation of the shear strength is remarkable both when the volumetric strain derived from the central strain is taken into account and when the averaged volumetric strain is used. The numerical results show that the overestimation depends highly on the rigidity index, but does not depend so much on the strain range over which the shear strength is measured.

As far as the self-boring pressuremeter tests in sand are concerned, the friction angle is overestimated because of the finite length of the pressuremeter. The overestimation does not depend much on which strain is used, central hoop strain or volumetric hoop strain. The overestimation depends highly on the stiffness index, but is less affected by the friction angle. This means that the density of the sand does not affect the overestimation. It is also found that Hughes *et al.*'s method tend to underestimate the friction angle because it ignores the elastic deformation in plastic area.

6.3 Full-displacement pressuremeter

The advantage of the full-displacement pressuremeter in comparison with the self-boring pressuremeter is that it is rather easy to perform a test, and is therefore economical. However, the problem is that disturbance during the installation of the pressuremeter is negligible. In order to investigate the effects of the length-to-diameter ratio on the pressuremeter test results, a finite length full-displacement pressuremeter test is modelled as a two-dimensional axisymmetric problem, and large strain elastic perfectly-plastic analysis is used.

It was found that use of Houlsby and Withers analysis tends to underestimate the rigidity index and overestimate the shear strength because the length of the pressuremeter is finite. The underestimation of the rigidity index and the overestimation of the shear strength depends highly on the rigidity index. The initial horizontal stress is found to be overestimated because of the finite length of the pressuremeter, however, the overestimation is not influenced by the rigidity index. The interpretation method developed in this thesis is applied to the *in-situ* tests performed by Powell and Shields, and Houlsby and Withers. The results suggests that the correction does not fully explain the observed initial horizontal stress, but the direction of the correction is right.

6.4 Experimental Work

Several tests of the cone-pressuremeter in sand were carried out using the Oxford calibration chamber. A 5 cm^2 device with length-to-diameter ratio, 5,10 and 20 was used. The result show that the limit pressure increase as the length-to-diameter ratio decreases. The effects of the length-to-diameter ratio seem to be more significant when the density is low.

6.5 Recommendations for future work

As far as theoretical work is concerned, the interpretation method for the pressuremeter test in clay is well-established. On the other hand, the interpretation of the pressuremeter test in sand is not so well-established, although Yu (1990)

developed an exact solution. Since the simplified Hughes *et al.*'s method ignores the elastic deformation in the plastic area, which effects significantly on the measured friction angle, an alternative interpretation method should be developed to interpret the pressuremeter test simply.

For numerical work, it is proposed that finite element analysis of the full-displacement pressuremeter in sand should be performed, to analyse the effects of the length-to-diameter ratio.

Lastly, it is proposed that the calibration chamber should continue to be used to calibrate the cone-pressuremeter. It is also proposed that a 10 cm^2 device in which the length-to-diameter ratio can be changed should be developed, since the 5 cm^2 is not sufficiently strong to perform a test with dense sand, and it has no strain arm measurement.

Finally, the results of the numerical work and the results of the calibration chamber tests should be corrected.

References

[1] F. J. Baguelin, R. A. Frank, and Nahra R. A theoretical study of pore pressure generation and dissipation around the pressuremeter. *Proc. 2nd Int. Symp. on the Pressuremeter and Its Marine Applications, ASTM*, pages 169–186, 1986.

[2] M. Borsetto, L. Imperato, R. Nova, and A. Peano. The interpretation of *in-situ* soil tests. *Symposium International (Paris)*, 2:211–215, 1983.

[3] H.J. Burd. A large displacement finite element analysis of a reinforced unpaved road. *D.Phil thesis, Oxford University*, 1986.

[4] L. Dormieux. Bounding solutions for the pressuremeter modulus using variational principles in elasticity. *International journal for numerical and analytical methods in geomechanics*, 16(5):311–321, 1992.

[5] M. Fahey and M.F. Randolph. Effect of disturbance on parameters derived from self-boring pressuremeter tests in sand. *Géotechnique*, 34(1):81–97, 1984.

[6] R. E. Gibson and W.F. Anderson. *In-situ* measurement of soil properties with the pressuremeter. *Civil Engineering Public Works Review*, 56(658):615–618, 1961.

[7] G. T. Houlsby and J. P. Carter. The effects of pressuremeter geometry on the results of tests in clay. *Géotechnique*, 43(4):567–576, 1993.

[8] G. T. Houlsby and N. J. Withers. Analysis of the cone pressuremeter test in clay. *Géotechnique*, 38(4):573–587, 1988.

[9] J. M. Hughes, C. P. Wroth, and D. Windle. Pressuremeter tests in sand. *Géotechnique*, 27(4):455–477, 1977.

[10] M. Jamiolkowski, C.C. Ladd, J.T. Germaine, and R Lancellotta. New developments in field and laboratory testing of soils. *Proc. 11th Int. Conf. on Soil Mech. and Found. Eng., San Francisco*, 1:57–154, 1985.

[11] B. Ladanyi. Evaluation of pressuremeter tests in granular soils. *Proc. Second Pan American Conf. Soil Mech. Found. Eng.*, 1, 1963.

[12] J. E. Laier and J.H. Schmertmann. Effect of finite pressuremeter length in dry sand. *Proceeding Conference In Situ Measurement of Soil Properties, American Society of Civil Engineers*, pages 241–259, 1975.

[13] M. Livneh, M. Gellert, and J. Uzan. Determination of the elastic modulus of soil by the pressuremeter test- theoretical background. *Journal of Materials*, 6(2):348–355, 1971.

[14] R. J. Mair and D.M. Wood. Pressuremeter testing- methods and interpretation. *CIRIA Ground Eng. Report, In-situ testing, Butterworths, London*, 1987.

[15] N.R.F. Nutt. Development of the cone-pressuremeter. *D.Phil thesis, Oxford University*, 1993.

[16] M. J. Pedley. The performance of soil reinforcement in bending and shear. *D.Phil thesis, Oxford University*, 1990.

[17] J.J.M. Powell and C.H. Shields. Field studies of the full displacement pressuremeter in clays. *Proc. 4th Int. Symp. on Pressuremeters, The pressuremeter and its new avenues (edited by Gérard Ballivy), Balkema*, pages 239–246, 1995.

[18] P. W. Rowe. The relation between the shear strength of sands in triaxial compression, plane strain and direct shear. *Géotechnique*, 19(1):75–86, 1962.

[19] F. Schnaid. A study of the cone pressuremeter test in sand. *D.Phil thesis, Oxford University*, 1990.

[20] D. A. Shuttle and M. G. Jefferies. A practical geometry correction for interpreting pressuremeter tests in clay. *Géotechnique*, 45(3):549–555, 1995.